

Nanoscale

Accepted Manuscript



This is an *Accepted Manuscript*, which has been through the Royal Society of Chemistry peer review process and has been accepted for publication.

Accepted Manuscripts are published online shortly after acceptance, before technical editing, formatting and proof reading. Using this free service, authors can make their results available to the community, in citable form, before we publish the edited article. We will replace this *Accepted Manuscript* with the edited and formatted *Advance Article* as soon as it is available.

You can find more information about *Accepted Manuscripts* in the [Information for Authors](#).

Please note that technical editing may introduce minor changes to the text and/or graphics, which may alter content. The journal's standard [Terms & Conditions](#) and the [Ethical guidelines](#) still apply. In no event shall the Royal Society of Chemistry be held responsible for any errors or omissions in this *Accepted Manuscript* or any consequences arising from the use of any information it contains.

3D graphene nanomaterials for binder-free supercapacitors: scientific design for enhanced performance

Shuijian He ^{a,b}, Wei Chen^{a*}

^aState Key Laboratory of Electroanalytical Chemistry, Changchun Institute of Applied

Chemistry, Chinese Academy of Sciences, Changchun, Jilin 130022, China

^bUniversity of Chinese Academy of Sciences, Beijing 100039, China

*Corresponding author, Email: weichen@ciac.ac.cn; Tel. +86 431 85262061

Abstract

Attributed to the excellent intrinsic properties, especially the strong mechanical strength, extraordinarily high surface area and extremely high conductivity, graphene is deemed as versatile building block in fabricating functional materials for energy production and storage applications. In this article, the recent progress in the assembly of binder-free and self-standing graphene-based materials and their application in supercapacitors are reviewed, including electrical double layer capacitors, pseudocapacitors, and asymmetric supercapacitors. Various fabrication strategies and the influence of structures on the capacitance performance of 3D graphene-based materials are discussed. We finally give concluding remarks and an outlook on the scientific design of binder-free and self-standing graphene materials for achieving better capacitance performance.

Key words: Graphene; binder-free; supercapacitor, three-dimension; carbon; energy storage

1. Introduction

1.1 Mechanism and application of supercapacitors

Supercapacitor, also named ultracapacitor or electrochemical capacitor, is a type of energy storage device with many promising properties, including long cycle life ($>10^6$ times), high power density, easy maintenance and relatively low cost.¹ Supercapacitors bridge the power/energy gap between traditional dielectric capacitors (which have high power density and low energy density (E)) and batteries/fuel cells (which have high energy density and low power density).² The applications of supercapacitors are mainly grouped into three categories: power capture and supply; power quality applications; backup, safety and low maintenance applications.³

According to the energy storage mechanism, supercapacitors can be divided into electrical double layer capacitors (EDLCs) and pseudocapacitors (PCs). EDLCs store energy by the accumulation of electrostatic charges at the interface of electrode and electrolyte.⁴ The mechanism of an EDLC could be described by using a traditional dielectric capacitor as model. The specific capacitance (C_s) can be calculated by equation 1:^{5,6}

$$C_s = \epsilon_0 \epsilon_r S_A / d \quad (1)$$

where ϵ_0 is the electric constant (8.854×10^{-12} F m^{-1}), ϵ_r is the relative dielectric constant of electrolyte which is larger than 1, S_A is the specific surface area of the electrode materials ($m^2 g^{-1}$), and d is the effective thickness of the electrical double layer (charge separation distance, m). The double layer capacitance is usually between 5 and 30 $\mu F cm^{-2}$ depending on the used electrolyte.⁷ Commonly, carbon materials are the most used electrode materials for EDLCs attributed to their low cost, large surface area, high stability and good conductivity.⁸ The specific surface area of carbon materials can reach 3000 $m^2 g^{-1}$ and result in specific capacitance larger than 150 F g^{-1} .^{9, 10} Clearly, this value is several orders of

magnitude greater than conventional capacitors (pF or nF).

The energy of PCs originates from fast faradaic redox reactions of electroactive materials which occur at the interface between electrode and electrolyte,⁶ as illustrated in equation 2.



The theoretical specific capacitance of a pseudocapacitor can be calculated according to equation 3:¹¹

$$C_s = Q/U = nF/(MU) \quad (3)$$

Here, n is the mole number of electrons participating in the redox reaction (mole); Q is the total charges released during the discharge process (C); U is the potential window (V); F is the Faraday constant ($9.64853 \times 10^4 \text{ C mol}^{-1}$) and M is the relative molar mass of the active material (g mol^{-1}). The electrode materials for PCs are mainly transition metal compounds including manganese oxide (MnO_2),¹² nickel oxide (NiO),¹³ cobalt oxide (Co_3O_4),¹⁴ nickel cobaltite (NiCo_2O_4),¹⁵ nickel hydroxide (Ni(OH)_2),¹⁶ vanadium pentoxide (V_2O_5),¹⁷ iron oxide (Fe_3O_4),¹⁸ nickel sulfide (NiS),¹⁹ etc., and conducting polymers including polyaniline (PANI),²⁰⁻²³ polypyrrole (PPy),²⁴⁻²⁶ polythiophene (PTh)^{27,28} and their derivatives.^{29,}

³⁰ According to equation 3, the theoretical specific capacitance values of PCs electrode materials surpass 1000 F g^{-1} or in the range of $100 \sim 400 \mu\text{F cm}^{-2}$ which is one or two orders of magnitude greater than that of EDLCs.³¹ However, for PCs, the redox reactions only occur at the interface between active materials and electrolyte and the diffusion distance of electrolyte into active materials is only $\sim 20 \text{ nm}$ in depth.³² In fact, specific capacitance values of PCs electrode materials are far below their theoretical values due to unsatisfied specific surface area, relatively low conductivity and low mass transfer rate.

Apart from electrode materials, electrolyte also plays a great role in determining the performance of a supercapacitor, especially the cell voltage, energy density (E) and power density (W).³³ E and W of a SC can be calculated by $E = 0.5CV^2$ and $W = V^2/4R$ (R is the internal resistance of the cell), respectively. The

cell voltage of a SC is mainly dependent on the decomposition voltage of the used electrolyte. Generally, there are two types of electrolytes, aqueous and nonaqueous electrolytes.³⁴ With aqueous electrolyte, the cell voltage is often below 1.0 V, which is limited by the decomposition voltage of aqueous electrolyte (1.23 V) and electrode polarization.^{35,36} However, the cell voltage of a SC based on nonaqueous electrolyte could be larger than 3.0 V.^{33,37} Hence, SCs built with nonaqueous electrolytes usually exhibit larger energy density than their counterparts with aqueous electrolytes. In fact, commercial SCs are usually fabricated with nonaqueous electrolytes. However, the application of nonaqueous electrolytes is largely hindered by their high cost, high toxicity, security problems and rigorous conditions for fabricating SCs. In fundamental researches, aqueous electrolytes are widely used due to their low cost, easy availability and eco-friendliness. Moreover, a new configuration of supercapacitor named asymmetric supercapacitor (ASC) has also been developed in order to improve E and W of SCs based on aqueous electrolyte.^{34,38} In a typical ASC, two types of electrode materials with different working electrochemical potential range are used: one with high power density but low energy density (mainly carbon materials), another one with high energy density but low power density (conducting polymers and/or transition metal compounds). Compared with conventional symmetric SCs, ASCs can take advantage of the different potential windows of the two electrodes to broaden the maximum operating voltage of a cell system above 1.5 V, resulting in an obvious improvement in E and W.³⁹⁻⁴¹

There are many issues should be taken into consideration for designing and preparing electrode materials for supercapacitors. First, it is important to explore novel active materials with high surface to bulk ratio (high surface area) to enlarge the interface between electrode and electrolyte.³ Second, high conductivity is necessary to improve the utilization efficiency and rate performance of electrode materials.⁴² Third, rational porous structure is beneficial for quick electrolyte diffusion and boosting rate

performance.⁴³ Hence constructing supercapacitor electrode materials with large specific surface area, rational porosity and high electronic conductivity is highly preferred.³ Among the carbon material family, graphene is the newest member and its unique properties have attracted increasing attention in recent years, especially in fields of energy storage and transfer. In this article, we focus on the development of 3D graphene-based electrode materials in recent years for binder-free fabrication of supercapacitors.

1.2 Preparation and properties of graphene

Graphene (GE), as defined by the International Union of Pure and Applied Chemistry (IUPAC), is two-dimensional (2D) planar single layer made up by sp^2 carbon atoms. GE has attracted great attention in many fields since its debut in 2004 owing to its unique structural features and the resulting outstanding physical and chemical properties. Up to now, there are a lot of reviews summarizing the properties, preparation and applications of GE-based materials.⁴⁴⁻⁴⁹ Ideal graphene sheets achieved by mechanical exfoliation technique have proven to have a lot of extraordinary properties, such as highly ordered structure, excellent optical transparency, high thermal conductivity (5000 W mK^{-1}), large surface area ($2630 \text{ m}^2 \text{ g}^{-1}$), strong chemical durability, high young's modulus (1 TPa), high electron mobility ($2.5 \times 10^5 \text{ cm}^2 \text{ V}^{-1} \text{ s}^{-1}$) and high electrical conductivity (7200 S m^{-1}) etc.^{50, 51}

In fact, although IUPAC defines GE as a monolayer of carbon atoms, bilayers, trilayers and multilayers of GE are actually produced in practical synthesis, and the size, thickness and properties of GE prepared by different methods vary greatly. Generally, there are two approaches for preparation of GE: "top-down" and "bottom-up".^{50, 52} In the "top-down" way, GE materials are prepared by mechanical/chemical exfoliation of graphite powder/rod and unrolling/splitting of carbon nanotubes.⁵³⁻⁵⁷ GE prepared from mechanical exfoliation is considered to be ideal graphene sheets with low defects. However, mechanical exfoliation

process has low throughput and it is unlikely to be an ideal method for large-scale preparation of GE. Chemical exfoliation is regarded as an fascinate alternative method of mechanical exfoliation to prepare GE from graphite.⁵⁸ In a chemical exfoliation process, exfoliation of graphite is accomplished by intercalation and exfoliation of graphite via an intermediate named graphite intercalation compounds (GIC).⁵⁹ A GIC is composed of ions or molecules inserted between layers of graphene that leave the layered structure of graphite intact.⁶⁰ After oxidation through Hummers' method or other approaches, a water-dispersible graphite oxide can be achieved. Graphite oxide is a layered stack of puckered graphene sheets and it can be completely exfoliated into single layer graphene oxide (GO) upon the additional mechanical energy (for example ultrasonic treatment) due to the strong interactions between solvent and the oxygen-containing functionalities (carboxyl, carbonyl, epoxy and hydroxyl groups) introduced into the basal planes and edges of graphene sheets during the oxidation.^{61, 62} In the "bottom-up" approaches, GE can be synthesized from small molecular precursors by total organic synthesis or chemical vapor deposition (CVD).^{50, 63} Total organic synthesis is complex and the obtained GE is limited in size and scale. Actually, GE preparation through total organic synthesis is still in progress.^{64, 65} GE can also be prepared through pyrolyzation of gas precursors (methane (CH₄), ethylene, acetylene, ethanol, etc.) via CVD at high temperature with or without substrates.^{63, 66-68} GE prepared by CVD normally exhibits low defects but with limited outputs compared to chemically derived GE using GO as precursor. Compared to other precursors, GO has two outstanding characteristics when serve as versatile building blocks for various GE structures: (1) GO can be large-scale produced using low price graphite as raw material via cost-efficient chemical methods,⁶⁹ and (2) GO is amphiphilic and can form stable aqueous colloids to facilitate the preparation of GE structures (films, papers, hydrogels, etc.) by simple and cheap solution processes (like filtration, dipping, layer by layer assembling, dropping and casting etc.), both of which are important for the

large-scale applications of GE.⁷⁰⁻⁷³

Attributed to the unique structural features, GE materials hold great promise for potential applications in many technological fields such as nanoelectronics, sensors, nanocomposites, energy storage and conversion.^{46, 60, 74-80} In the case of supercapacitors, GE materials play an irreplaceable role because of their excellent properties.⁸¹⁻⁸³ Firstly, GE has a very high theoretically specific surface area of $2630 \text{ m}^2 \text{ g}^{-1}$ which is among the highest specific surface area carbon materials.⁸⁴ This structural feature makes GE materials highly desirable for the formation of electrochemical double layers. The interfacial electrical double-layer capacitance on one side of a GE sheet was measured to be about $21 \mu\text{F cm}^{-2}$ and the theoretical gravimetric specific double-layer capacitance of GE is calculated to be approximately 550 F g^{-1} .⁸⁵ Secondly, GE materials, especially chemically modified graphene, can be prepared at relatively low cost and in large scale (tons) by using graphite as precursor.⁶⁹ Thirdly, the high electrical conductivity of GE ensures its large power density and excellent rate performance. Fourthly, high thermal, mechanical, chemical, and electrochemical stabilities of GE can guarantee the long cycle life of supercapacitors.⁸⁶ Fifthly, GE materials can not only be used directly in 2D nanosheet form, but also be built into various 3D self-supported structures, including papers, films, hydrogels, aerogels, foams and fibers, to fabricate conductive, additive- and binder-free electrodes for supercapacitors.^{78, 87} Finally, but not last, GE-based structures are ideal substrates to support other active materials for supercapacitors due to their ample specific surface area, good conductivity and tunable structures.^{88, 89}

1.3 Objective

In recent years, self-supported and binder-free electrode materials have been developed very quickly for supercapacitor application.^{37, 90-96} Generally, discrete powdery materials have to be blended with insulated polymer binders (like polyvinylidene fluoride and polytetrafluoroethylene) and additional conductive

agents (like carbon black) to prepare electrodes. The addition of binders could increase the contact resistance between active materials and requires the addition of conductive agents to reserve the electric conductivity of electrodes. Moreover, the addition of binders and conductive agents can not only result in “dead volume” and “dead weight” of electrodes, but also increase the polarization of the electrode which may lead to the decay of rate performance. Recent studies demonstrated that some specially engineered self-supported 3D structures can be fabricated into electrodes directly without the help of binders and conductive agents, and therefore showed additional advantages over powdery materials.^{42, 97-100} Compared to other binder-free electrode materials, graphene-based materials exhibit the obvious advantages, e.g. low weight, various configuration methods, controllable structure and flexibility etc. There have been several reviews focusing on the preparation and capacitance performance of graphene-based electrode materials for supercapacitors.^{81-83, 101-104} However, there is no review especially concerning the design, preparation and performance of 3D graphene-based materials for binder-free fabrication of supercapacitors. In this article, as shown in Scheme 1, we will summarize the state-of-art progress in preparation and capacitance performance of binder-free supercapacitors constructed from 3D graphene and their composite materials. Herein, we highlight symmetric supercapacitors (electrical double layer capacitors and pseudocapacitors) based on graphene, graphene/transition metal compound hybrids, graphene/conducting polymer composites, and asymmetric supercapacitors based on above materials. The influence of drying and reduction processes on the structure, porosity and capacitance performance of the self-standing GE materials built by solution processes is specially discussed in this review since many interesting and breakthrough work have been done in this field. Finally, concluding remarks and the outlook on the rational design, construction of 3D graphene-based nanostructures for supercapacitor application are presented.

2. Self-supporting graphene materials for electrical double layer capacitors (EDLCs)

2.1 Self-supporting unitary graphene materials for EDLCs

Owing to the high specific surface area and electrical conductivity, unitary GE can be fabricated into self-supported structures via solution processes and CVD approaches, and the constructed 3D structures can be directly used as high performance binder-free electrode materials for EDLCs, as listed in Table 1.¹⁰⁵⁻¹⁰⁹ Graphene oxide, the fascinate precursor of graphene, can be built into various self-supported forms via solution processes and then converted to highly conductive reduced graphene oxide (rGO) structures by various reduction methods.^{71, 110-114}

2.1.1 Self-supporting unitary graphene materials prepared from solution process for electrical double layer capacitors

2.1.1.1 Effect of drying process on the structure and capacitance performance of self-supporting unitary graphene materials

Thanks to strong interactions among GO sheets, various GO structures including films, papers, hydrogels, etc. could be assembled by solution processes like dipping-coating,¹¹⁵⁻¹¹⁷ casting,¹¹⁸⁻¹²⁰ filtering,¹²¹⁻¹²³ layer-by-larger assembly,^{117, 124} spraying,^{107, 125, 126} hydrothermal assembly¹²⁷⁻¹²⁹ and wet spinning.^{26, 130, 131} The resulting GO structures need to be dried and reduced to the corresponding rGO counterparts for supercapacitor applications. The drying process has great influence on the porous structure and specific surface area of resulting products, and thus on their capacitance performance.

Direct drying wet GO structures in an ordinary way often generates compact films/papers due to structural contraction caused by strong capillary forces, which leads to shrinkage and overlap of GO or rGO nanosheets.¹¹⁷ The compact structures are unfavorable for rapid electrolyte diffusion and usually exhibit low specific surface area, leading to poor capacitance performance.^{107, 117, 132} For example, the

rGO/filter paper hybrid prepared by filtering and vacuum drying at 100 °C only exhibited a low specific capacitance (C_s) of 120 F g⁻¹ at 1 mV s⁻¹.¹³³ For a hydrazine-reduced rGO paper supported on flexible polycaprolactone/polyurethane film, after drying at ambient temperature its specific capacitance (C_s) can reach 218 F g⁻¹ at 0.5 A g⁻¹. However, the C_s quickly decreased to 110 F g⁻¹ when current density increases to 1.5 A g⁻¹, indicating the poor rate capacitance performance.¹³⁴ For the GO/GE hybrid film prepared by dropping mixed dispersion of GO/GE on glass carbon electrode and the following air drying at room temperature, the maximum C_s can only reach 120 F g⁻¹ at 0.2 A g⁻¹ and it rapidly decreased below 80 F g⁻¹ when current density increased to 2 A g⁻¹.¹³⁵

In order to prevent the aggregation of GO or rGO sheets and retain the porous structures during drying process, supercritical fluid drying and freeze drying techniques are usually applied to the preparation of porous rGO aerogels/films/papers.^{82, 119, 120, 127, 136} In a direct drying process, a liquid-vapor meniscus can be formed due to the surface tension of solvent and a capillary pressure gradient formed in the pore walls. Capillary force arisen from capillary pressure gradient is strong enough to collapse most part of the pore volume.¹³⁷ To preserve the porosity, it is vital to annihilate the surface tension of liquid. Replacing this liquid by a supercritical fluid with much lower surface tension is a convenient way. Supercritical fluid drying is a traditional drying technique for the preparation of aerogel/xerogel. In the process of supercritical fluid drying, the formation of a liquid-vapor meniscus is prevented.¹³⁸ Hence, the pore collapse phenomenon can be avoided and the porous texture can be released with intactness via supercritical fluid drying.¹³⁹ Freeze drying technique is another efficient approach to preserve the porosity. In the course of freeze drying, the capillary stress is limited by sublimation water from solid to the gas phase under vacuum. Freeze drying is achieved by making the system around triple point boundary of water and lowering the temperature. In fact, ice particles formed during freeze drying process can function

as green hard templates to reserve the porous texture.⁴⁴

Gao et al.¹³⁶ studied the capacitance performance of cellulose nanofiber/rGO aerogel which was prepared by supercritical CO₂ drying the corresponding hybrid hydrogels. The 3D porous structure was retained by supercritical CO₂ drying and the restacking of rGO sheets was inhibited by the introduction of cellulose nanofibers. C_s of the all-solid-state flexible supercapacitor reached 203 F g⁻¹ at current density of 0.7 mA cm⁻² and still reserved 134 F g⁻¹ when current density increased to 11.2 mA cm⁻².

Flexible and porous GO films can be directly obtained by casting or dropping concentrated GO solution on substrates and then freeze-drying by taking advantage of the strong interactions among GO sheets. After being reduced, porous and high conductive rGO films can be used for EDLCs.^{118,119} A rGO paper with the thickness of 10 μm was prepared and used as electrode material for supercapacitor by Liu and coauthors through pressing freeze-dried and 200 °C heat reduced rGO paper at 10 MPa.¹²⁰ During the freeze drying and heat reduction processes, ripples and wrinkles were formed on rGO sheets which prevented them from aggregation. Mechanical pressing led to the recovery of π-π conjugate of rGO sheets and an electronic conductivity of 10 S cm⁻¹ was obtained. The supercapacitor based on the as-prepared rGO paper displayed excellent rate performance and stability. A C_s of 172 F g⁻¹ was obtained at 1 A g⁻¹ and it can be still kept at 100 F g⁻¹ when current density was raised two orders of magnitude to 100 A g⁻¹. The excellent rate performance is far better than that of the directly dried and highly compact GE materials.¹³⁴ Moreover, after cycling at 20 A g⁻¹ for 5000 times, 99% capacitance was retained.

2.1.1.2 Effect of reduction approaches on the structure and capacitance performance of self-supporting unitary graphene materials

Besides drying process, reduction methods and processes also play a great role in controlling the porous texture and conductivity of resulted rGO structures and thus their capacitance performance. The basal

planes and edges of GO bear different oxygen-functional groups, such as carboxyl, carbonyl, hydroxyl, and epoxy groups, which make GO hydrophilic.⁷³ The presence of these functional groups destroys the planar sp^2 -hybridized carbons of graphene and converts them to sp^3 -hybridized carbons.¹⁴⁰ Hence, the π - π electronic conjugation is destroyed in GO sheets, leading to significant decrease in electrical conductivity. In fact, GO is insulating in nature.¹⁴¹ Therefore, it is necessary to reduce GO to rGO to improve electrical conductivity for supercapacitor application. Lots of methods, including chemical reduction, electrochemical reduction and thermal (including photothermal) reduction techniques have been used to reduce GO to rGO.^{123, 142} The electrical conductivity of rGO is in the range of 200–42 000 S m^{-1} hinging on the type of reducing agent, reduction time, reduction temperature, annealing temperature, and annealing time.¹¹³ Reduction process should be well controlled since rGO sheets tend to agglomerate and form graphitic structures when strong reducing agents are used, which result in sharp decrease in hydrophilic and dispersibility.¹⁴³ Moderate reduction with some oxygen functional groups left is preferred because the remaining oxygen functional groups can not only contribute pseudocapacitance to the total capacitance of rGO, but also facilitate better interaction between rGO sheets and the electrolyte.¹¹³

In a chemical reduction process, reducing agents like hydrazine monohydrate, hydroxylamine, sodium borohydride, hydroquinone, hydroiodic acid (HI), phenylenediamine, D-glucose, L-ascorbic acid and vitamin-C are often used.¹⁴³⁻¹⁴⁵ A type of multilayered graphene film was prepared through filtering process by Li's group.¹⁴⁶ In their experiments, ammonia and hydrazine were added into GO solution and the reduction process was carried out at 90 °C for 1 h. The resulting solution was filtered by vacuum suction to obtain rGO film. The wet film was then peeled off and washed before exchanging water with the electrolyte to assemble supercapacitor. As shown in Fig. 1 A-C, the obtained rGO film displayed good flexibility and the film was built by highly packed rGO nanosheets (Fig. 1D). From the results of the

electrochemical tests displayed in Fig. 1E-G, the obtained wet film exhibited greatly improved capacitance performance compared to its dried form. The maximum C_s of wet rGO film reached 215 F g^{-1} and 156.5 F g^{-1} was retained at ultrahigh current density of 1080 A g^{-1} . In comparison, freeze-dried or thermal-annealed samples showed much poorer rate performances. For instance, C_s of the freeze-dried film was below 25 F g^{-1} under the current density of 200 A g^{-1} and that of the thermal-annealed film almost decreased to zero when the current density exceeded 20 A g^{-1} . The outstanding performance of the wet rGO film is attributed to the readily available high specific surface area and good conductivity. Water in the wet film serves as an effective “spacer” to prevent the restacking and aggregation of rGO sheets. Electrostatic repulsions from negative charged groups on rGO sheets and the repulsive hydration forces between hydrated rGO sheets can efficiently resist the restacking of rGO sheets, which make the hydrated rGO sheets remain significantly separated and surface area available although combined together in a nearly parallel manner. A wet rGO film with area density of 0.045 mg cm^{-2} exhibited a sheet resistivity of $1860 \text{ } \Omega \text{ square}^{-1}$, while that of the corresponding freeze-dried sample is $740 \text{ } \Omega \text{ square}^{-1}$. The high conductivity of wet rGO film indicates that the rGO sheets are well connected.

Li's group further modified their method to prepare liquid electrolyte-mediated chemically-converted graphene (EM-CCG) films for supercapacitors with high volumetric energy densities.³³ The reduction process was carried out by adding ammonia and hydrazine into GO solution and holding temperature at $100 \text{ }^\circ\text{C}$ for 3 h. The preparation process of EM-CCG films is depicted in Fig. 2A. The resulting solution was filtered to obtain CCG gel film and then the film was peeled off and washed before exchanging water with a ratio-controlled volatile (water)/non-volatile (sulfuric acid (H_2SO_4) or 1-ethyl-3-methylimidazolium tetrafluoroborate (EMIMBF₄)) miscible solution. Finally, the films were clipped by two glass slides and moved to a vacuum oven with a high vacuum of 10 Pa for 12 h. The water inside the gel film was

evaporated, while the remained non-volatile liquid can make the CCG sheets solvated. Hence, porous yet densely packed CCG films with high ion-accessible surface area and low ion-transport resistance were obtained. As shown in Fig. 2 B-F, by increasing the ratio of volatile to nonvolatile liquids, the packing density of flexible CCG films could be controlled from 0.13 to 1.33 g cm³. The capacitance performance of these solvated CCG films is much higher than that of fully dried sample as indicated by Fig. 2 G-I. On the other hand, at 0.1 A g⁻¹, the C_s of EM-CCG films only dropped little from 203.2 to 191.7 F g⁻¹ with density increased from 0.13 to 1.33 g cm³ whilst that of fully dried CCG film (1.49 g cm³) only exhibited 155.2 F g⁻¹. The difference became more obvious when the films were tested at higher current density. For example, C_s of the EM-CCG films all exceeded 100 F g⁻¹ at 100 A g⁻¹, whereas the dried CCG film only yielded 10.2 F g⁻¹. The volumetric energy density against the whole EC stack of supercapacitors based on EM-CCG films reached 59.9 Wh L⁻¹ which was three times the value of dried CCG film (~18.4 Wh L⁻¹). The extremely high performance of EM-CCG films could be attributed to their novel structure with high ion-accessible surface area, continuous ion transport network and low ion transport resistance.

Electrochemical reduction is another promising method to remove oxygen functional groups on GO sheets.¹¹³ Electrochemical reduction of GO structures can be conducted in common electrochemical cells using a buffer solution at ambient temperature. With electrochemical reduction methods, GO reduction is realized by the electron exchange between GO sheets and electrodes, without the need of special reducing agents. Therefore, electrochemical reduction process is considered a “green” approach since it could avoid the use of toxic reductants (e.g. hydrazine) and eliminate byproducts.^{141, 147}

On the other hand, GO can be deposited on conductive substrates via electrochemical methods like electrodeposition, electrophoresis and electrospray, and the subsequent electrochemical reduction to rGO for supercapacitor application.^{106, 125, 145, 148-150} Shi et al. reported a type of EDLCs based on

three-dimensional interpenetrating rGO electrodes built by one-step electrochemical reduction of GO on a gold foil in 0.1 M lithium perchlorate solution at 1.2 V for 5-60 s, followed by further reduction in 1 M lithium perchlorate solution at 1.2 V for another 30 s.¹⁵¹ The impedance phase angle of EDLCs was as large as -84° at 120 Hz with a small RC time constant of 1.35 ms, which is comparable to that of a commercial aluminum electrolytic capacitor. EDLCs fabricated from the 3D interpenetrating graphene microstructure exhibited ultrahigh rate capability and high specific capacitance. In the electrochemical measurements, the cyclic voltammetric (CV) curve remained quasi-rectangular with only a little variance even at an ultrahigh scan rate of 400 V s^{-1} . C_s reached 487 mF cm^{-2} at 40 mA cm^{-2} and only decreased for 7% at 800 mA cm^{-2} . The EDLCs also showed good stability with almost no changed capacitance even after 10, 000 cycles at 700 mA cm^{-2} . The reported electrochemical reduction technique is environmentally friendly, fast, cheap, convenient and readily scalable to industrial levels. The as-built EDLCs showed the potential of substituting aluminum electrolytic capacitors in ac line-filtering.

Another efficient reduction method for GO reduction is thermal treatment. Annealing conditions, such as temperature, time and environment, play important roles in controlling the structure and performance of the resulted rGO materials.^{152, 153} Cho and co-authors studied the post-heating temperature on the physical and electrochemical capacitive properties of hydroiodic acid (HI)-reduced graphene oxide paper.¹¹⁸ The HI-reduced graphene oxide paper was prepared by drying GO solution in a Petri dish, peeling off and the following reduction in HI solution (55%) at 95°C for 1 h. The HI-reduced graphene oxide paper was finally annealed at different temperatures (200, 400, 600, 800, and 1000°C) in an environment of 15% H_2 in Ar gas for 0.5 h. Annealing temperature exhibited great influence on the specific surface area, the content of oxygen functional groups, electrical conductivity, and capacitance performance of the obtained rGO papers. It was found that the surface area and electrical conductivity of rGO papers increase with

increasing annealing temperatures, while the content of oxygen functional groups showed opposite tendency. The rGO paper annealed at 200 °C with a specific surface area of 264.4 m² g⁻¹ and an electrical conductivity of 6.32 S cm⁻² exhibited the maximum specific capacitance (225 F g⁻¹) among all the annealed samples.

Through an interesting leavening strategy, Chen's group reported a mild thermal reduction process to prepare porous and cross-linked rGO foams without adding any spacers or templates.¹⁵⁴ The leavening process is illustrated in Fig. 3A. Typically, to obtain rGO foams, the compact GO films prepared through filtering were hung above hydrazine monohydrate in an autoclave and heated at 90 °C for 10 h. The role of hydrazine vapor is to trigger the chemical reduction of GO to rGO with the rapid release of gaseous species (H₂O and CO₂). The compact layered structures can help to maintain the rapid evolution of gaseous species during reduction process, while the gaseous species can be simultaneously diffused into the compact layered films to form porous rGO foams with volume expansion. The volume expansion ratio of the resulting rGO foams could be easily controlled when the amount of hydrazine is below 40 μL. As shown in Fig. 3 B and C, this leavening strategy effectively hindered the self-agglomeration of graphene sheets and resulted in continuously cross-linked foams (with low resistance < 100 Ω sq.⁻¹). The flexible and freestanding rGO foams could be functioned as both current collectors and electrodes for supercapacitors owing to their good mechanical strength and high conductivity. It should be noted that the calculated Cs of the obtained rGO foams (110 F g⁻¹) is much larger than that of compact rGO films (17 F g⁻¹).

In the last five years, photothermal reduction has also emerged as an appealing alternative method to conventional thermal and chemical reduction of GO and has been thoroughly investigated. Compared to conventional thermal and chemical reduction routes, photothermal reduction shows many distinctive

advantages, such as green process, simplicity, tunable reduction degree, high efficiency, low cost, and the flexibility for the fabrication and integration of GE-based microdevices.^{114, 155-157} Photothermal reduction mechanism is based on photothermal effect. GO structures can absorb and confine light energy, leading to rapid temperature increase (400–500 °C) within a few milliseconds upon exposure to intense light sources.¹⁵⁸ According to Smirnov's threshold effect, the photon energy that can initiate GO reduction should exceed 3.2 eV.¹⁵⁹ In this case, the photothermal effect would commonly exist when the light source used for GO reduction contains a relatively wide wavelength range (e.g., ≈ 390 nm).¹¹⁴ Therefore, any visible light that can provide enough light energy could be used for photothermal reduction of GO and a dramatic and high degree reduction of GO can be realized under ambient conditions.^{123, 160} The light sources for photothermal reduction of GO include sunlight, UV light, Xe lamp, Hg lamp, laser and so on.¹¹⁴

Photothermal reduction of GO is a convenient and versatile method in fabricating flexible and patterning GE-based supercapacitor devices.^{123, 125, 142, 157} Ajayan and co-workers reported a scalable fabrication of a new type of rGO-GO-rGO structured, monolithic EDLCs by laser reduction and patterning of hydrated GO films.¹⁶¹ The free-standing hydrated GO films were prepared by vacuum filtration and the following laser reduction by a CO₂ laser printer. The ability to laser reduce GO into conductive rGO enables the facile and non-toxic fabrication of various patterns and shapes of rGO-GO-rGO structures with both in-plane and sandwich configurations in a single hydrated GO film, as displayed in Fig. 4. The active electrode material of rGO reduced by laser heating hydrated GO film was porous due to the gas released from the decomposition of oxygen functional groups and evaporation of water under localized laser heating. The substantial amount of trapped water ($\sim 16\%$ wt) in the unreduced GO makes it simultaneously an electrical insulator and a good ionic conductor, empowering it to serve as both a solid-state electrolyte and an

electrode separator with ion transport characteristics. The supercapacitor fabricated from laser-reduced hydrated GO film with an in-plane circular geometry structure displayed the highest area capacitance (0.51 mF cm^{-2}) which was nearly twice that of the sandwich structure. In addition, the performance of the devices could be further improved by introducing external electrolytes.

Kaner's research team also fabricated a type of high performance supercapacitors based on flexible GE film via laser scribing.⁵⁶ In their experiments, commercially available inexpensive LightScribe CD/DVD optical drive was used to realize the direct laser-reduction of GO films which were pre-synthesized by either vacuum filtering or drop-casting GO dispersions. GO films were first dried under ambient condition for 24 h and then affixed on top of a LightScribe enabled DVD media disc, and finally moved into the DVD optical drive for laser treatment by the infrared laser inside it. The laser irradiation initiated the simultaneous exfoliation and reduction of GO sheets, and generated an open network of rGO, as shown in Fig. 5. This structure can effectively inhibit the agglomeration of rGO sheets and facilitate the electrolyte accessibility to the rGO surface. The as-prepared rGO films with a large surface area of $1520 \text{ m}^2 \text{ g}^{-1}$ are highly electrical conductive (1738 S m^{-1}) and mechanically robust (with only $\sim 1\%$ change in the electrical resistance of the film after 1000 bending cycles), and could be directly used as both current collector and active material for supercapacitor application. For the symmetric supercapacitors based on rGO films, the CV curves still maintained nearly rectangular shape with scan rate as high as 10 V s^{-1} in $1 \text{ M H}_3\text{PO}_4$ electrolyte, even though no binders, no conductive additives, or no metal current collector were used. The area capacitance of the rGO films was calculated to be 3.67 mF cm^{-2} in $1 \text{ M H}_3\text{PO}_4$ electrolyte and 4.04 mF cm^{-2} in $1 \text{ M H}_2\text{SO}_4$ electrolyte at 1 A g^{-1} . The device also exhibited a very high rate capability with a capacitance above 1.84 mF cm^{-2} even when tested under an ultrafast charge/discharge rate of 1000 A g^{-1} on the 0.1-s time scale. A flexible all-solid-state supercapacitor built with PVA/ H_3PO_4 polymer gelled

electrolyte showed excellent cycling stability (> 97% of the initial capacitance was retained even been cycled 10,000 times) and high stability over 4 months of testing. Moreover, energy losses, the operating current and voltage of supercapacitor devices could be regulated by using tandem parallel and serial assemblies.

Kaner's group further modified their experiments and developed a readily scalable fabrication of laser-scribed GE micro-supercapacitor (LSG-MSC) over large areas by direct laser writing on GO films in a standard LightScribe DVD burner.¹⁶² As shown in Fig. 6A-F, the interdigitated rGO electrode circuits designed by computer could be readily "writing" on the disc in a standard LightScribe DVD burner via using the precision of a laser. Note that the process does not require masks, post-processing, expensive materials or clean room operations, like conventional micro-fabrication methods. More than 100 micro-supercapacitors could be built on a single disc in 0.5 h or less. With such method, rGO film with conductivity of $2.35 \times 10^3 \text{ S m}^{-1}$ and specific surface area of $1500 \text{ m}^2 \text{ g}^{-1}$ can be synthesized. Extremely thin and completely flexible all-solid-state micro-supercapacitor devices with interdigitated microelectrodes in planar in different configurations were fabricated. The in planar micro-devices showed better capacitance performance compared to the sandwich structure as displayed in Fig. 6G and H. Moreover, the more interdigitated electrodes per unit area, the more energy and power could be obtained from the micro-devices due to the shortened ionic diffusion pathway between two microelectrodes. The micro-supercapacitor device with 16 interdigitated microelectrodes exhibited a stack specific capacitance of 3.05 F cm^{-3} at 16.8 mA cm^{-3} , and 60% of this value was maintained when charged under $1.84 \times 10^4 \text{ mA cm}^{-3}$. The micro-supercapacitor devices also exhibited exceptional stability regardless of the degree of twisting or bending and the electrolytes used (aqueous hydrogel polymer electrolytes (PVA/H₂SO₄) and viscous ionogel (fumed silica nanopowder mixed with 1-butyl-3-methylimidazolium

bis(trifluoromethylsulfonyl)imide)). What's more, the micro-supercapacitor devices could be assembled in tandem parallel and serial to regulate their energy losses, operating current and voltage, as presented in Fig. 6 I, K.

2.1.1.3 Self-supporting unitary graphene materials prepared by hydrothermal assembly for EDLCs

Apart from aforementioned filtering, casting, electrodeposition, electrophoresis and electrospray methods, hydrothermal assembly is another facile solution-process method for fabricating self-supporting unitary graphene materials. The as-prepared rGO structures are very suitable for supercapacitor application due to the simple preparing process and novel structure characteristics, including 3D interconnected porosity, large specific surface area and high conductivity.^{26, 128, 163-165} Shi et al.¹⁶⁶ successfully prepared a mechanically strong, electrically conductive, thermally stable and highly porous self-assembled rGO hydrogel (SGH). The SGH was fabricated by one-step hydrothermal reduction and assembly of GO aqueous at 180 °C. The specific capacitance of SGH reached 175 F g⁻¹. Shi et al. reported another cheap, facile, and effective method for preparing rGO hydrogel/nickel foam composite electrode (G-Gel/NF) by immersing a piece of nickel foam into GO solution containing vitamin C and the following reduction at 60 °C for 2 h.¹⁶⁷ The as-prepared G-Gel/NF can be directly used as electrode for supercapacitor without drying. The G-Gel/NF showed excellent rate performance attributed to the high conductivity of nickel foam, interconnected porosity and large ions-available surface area ($\geq 1260 \pm 48 \text{ m}^2 \text{ g}^{-1}$). The CV curve still maintained a quasi-rectangular shape, even at a high scan rate of 10 V s⁻¹. C_s of the G-Gels/NF was 45.6 mF cm⁻² at 0.67 mA cm⁻² and retained 36.2 mF cm⁻² when current density rises to 183.3 mA cm⁻² (516.3 A g⁻¹). Their works have attracted great attentions and lots of rGO materials have been prepared via the hydrothermal technique and applied as electrode materials for supercapacitors.^{127, 129, 168-170}

Qu et al. synthesized a type of novel graphene fiber by a facile one-step dimensionally-confined

hydrothermal strategy, in which Teflon-lined autoclave was replaced by glass pipeline with a 0.4 mm inner diameter.¹⁷¹ The as-prepared graphene fiber showed robust mechanical strength, good conductivity and flexibility, which render it suitable for flexible/stretchable energy-storage devices.¹⁷² The authors designed and fabricated a unique all GE core–sheath fiber (GF@3D-G) through the electrodeposition and reduction of a sheath of 3D porous rGO network over hydrothermally prepared GE fiber (core).¹⁷³ The high conductivity of the GE fiber core and the highly exposed surface area of 3D rGO network were well combined within the GE core–sheath fiber, thus offering great advantages as flexible electrodes for fiber-based supercapacitor (Fig. 7 A, B). The GE core–sheath fiber showed a conductivity of 10–20 S cm⁻¹ and large tensile stress about 160 MPa. Therefore, such fibers could be fabricated into twined supercapacitor devices with specific capacitance ca. 1.2–1.7 mF cm⁻² in PVA/H₃PO₄ gel polyelectrolyte which is much larger than that of bare GE fiber (Fig. 7 C-I).

Recently, Duan et al. reported a type of holey rGO hydrogel framework (HGF) built from holey rGO sheets via H₂O₂-assisted hydrothermal method with simultaneous reduction of GO, etching of nanopores in rGO sheets and self-assembly of rGO into 3D network structures, as illustrated in Fig. 8A-C.³⁷ During the hydrothermal process, the carbon atoms near the more active defective sites of GO sheets could be partially oxidized and etched by H₂O₂ molecules, leading to carbon vacancies, which gradually extend to larger nanopores. The etching reaction could occur across the whole rGO sheets and result in numerous in-plane pores with a few nanometers since the defective carbon sites are distributed throughout the basal plane of rGO sheets, as presented in Fig. 8D.¹⁷⁴ Brunauer–Emmett–Teller (BET) specific surface area of the freeze-dried holey rGO aerogel was measured to be 830 m² g⁻¹ which is more than three times the value of non-holey rGO aerogel (~260 m² g⁻¹) built by pristine rGO sheets (Fig. 8E). Freestanding compact holey rGO hydrogel films with a high packing density of 0.71 g cm⁻³ could be obtained by mechanically

compressing holey rGO hydrogel without complete restacking while maintaining the original solvated state (Fig. 8F, G). The compact and flexible holey rGO hydrogel films showed excellent electrical conductivity ($\sim 1,000 \text{ S m}^{-1}$) and were mechanically strong enough to be directly used as the EDLCs electrodes. The nanopores in holey rGO sheets are large enough to act as the ion diffusion shortcuts between different rGO sheets to greatly accelerate the ion transport across the whole film and enable the entire surface area ion-available. The large ion-available specific surface area, 3D interconnected porous structure and high conductivity resulted in the large specific capacitance and excellent rate performance of the holey rGO hydrogel films. CV curves at a high scan rate of 1 V s^{-1} still kept nearly rectangular shape and the charge/discharge plots at 100 A g^{-1} retained nearly triangular for supercapacitors tested in 6 M KOH electrolyte (Fig. 8H, I). The electrodes fabricated from holey rGO hydrogel films exhibited a C_s of 310 F g^{-1} at 1 A g^{-1} which is 1.5 fold of the non-hole rGO electrodes (208 F g^{-1}). When the current density increased to 100 A g^{-1} , the C_s of holey rGO hydrogel film electrodes retained 237 F g^{-1} , while that of the non-hole rGO hydrogel films was only 131 F g^{-1} (Fig. 8J). Moreover, the holey rGO hydrogel films exhibited outstanding capacitance performance (298 F g^{-1} or 212 F cm^{-3} at 1 A g^{-1}) and good stability in organic electrolyte (91% capacitance retention over 10,000 cycles at 20 A g^{-1}).

2.1.1.4 Self-supporting unitary graphene materials prepared by wet spinning for EDLCs

Recently it was found that GO can form graphene oxide liquid crystals (GOLC) in a twist-grain-boundary phase-like model with simultaneous long-range helical frustrations and lamellar ordering, which has led to the opportunity for continuous wet spinning of GOLC into macroscopic GO fibers.^{172, 175-178} The simple, green and cost-effective manufacturing process, outstanding mechanical strength and electrical properties make wet spinning GOLC a promising approach in preparing GE fibers for various applications.¹⁷⁹⁻¹⁸²

Aboutalebi, et al. developed a large-scale flexible fabrication of highly porous and high-performance multifunctional GO and rGO fibers and yarns by taking advantage of the intrinsic soft self-assembly behavior of ultralarge GO sheets liquid crystalline dispersions.¹⁸³ In their experiments, wet-spinning of ultralarge GO sheets liquid crystalline dispersions was conducted using a custom-built wet-spinning apparatus and acetone was used as coagulation bath. The obtained GO fibers were dried by air at ambient temperature and were then reduced by annealing at 220 °C overnight under vacuum. In the synthesis, acetone plays an important role in the formation of highly porous structure attributing to its very fast dehydration rate. Therefore, large sheet size and high interlayer spacing were simultaneously maintained even after thermal reduction. The as-prepared rGO fiber exhibited high conductivity of $2508 \pm 632 \text{ S m}^{-1}$, a superhigh specific surface area of $2210 \text{ m}^2 \text{ g}^{-1}$ ($2605 \text{ m}^2 \text{ g}^{-1}$ before reduction), an excellent mechanical strength with Young's modulus of $10.13 \pm 2.25 \text{ GPa}$, and ultimate stress of $49.3 \pm 3 \text{ MPa}$. The interconnected porous structure, suitable interlayer spacing and high conductivity endowed rGO fibers with excellent capacitance performance. The authors fabricated a range of different configuration electrodes and devices and evaluated their capacitance performances. The results showed that rGO fiber yarns were the only practical form for real-life device applications. C_s of the rGO fiber yarns reached 409 F g^{-1} at 1 A g^{-1} and retained 56 F g^{-1} at 100 A g^{-1} . The supercapacitor also displayed good stability with no obvious capacitance loss even after 5000 cycles of test at 10 A g^{-1} . Both rGO fibers and rGO yarns showed outstanding tensile strength and could be easily built into conductive textiles. This work demonstrated the opportunities of the application of GE in wearable electronic gadgets.

2.1.1.5 Capacitance performance of self-supporting unitary graphene materials prepared via other solution processes

GE materials can also be prepared by “dipping and coating” and “layer by layer assembly” approaches

via GO solution process attributing to the amphiphilic property of GO.^{22, 116, 184} During the preparation processes, porous substrates (e.g. nickel foam and alumina fiber blanket) can also serve as hard templates to offer 3D networks in building porous GE structures.^{115, 185}

Huang et al. reported a simple strategy to prepare 3D rGO/Ni foam hybrid for supercapacitor by a “dipping and drying” process.¹¹⁵ Typically, Ni foam was repeatedly dipped into GO dispersion and air dried at room temperature, and the resulting GO/Ni foam composite was finally reduced by ascorbic acid at 60 °C. The as-prepared rGO/Ni foam hybrid displayed good rate capacitance performance. The CV curve kept a rectangular-like shape even at a high scan rate of 2 V s⁻¹. C_s of the rGO/Ni foam hybrid reached 152 F g⁻¹ at 0.36 A g⁻¹ and retained 107 F g⁻¹ when current density increased more than 250 folds to 90.9 A g⁻¹. The mass of the electrode could be greatly decreased by etching most of the Ni foam away (reduced from 30 mg cm⁻² to less than 5 mg cm⁻²). C_s of the etched rGO/Ni foam hybrid reached ~128 F g⁻¹ at 0.36 A g⁻¹ and retained 105 F g⁻¹ at 10 A g⁻¹.

Ye and coworkers presented the preparation and capacitance performance of a rGO aerogel/Ni foam hybrid.¹⁸⁶ The rGO aerogel/Ni foam hybrid was prepared by two steps. First, Ni foam sheet filled with GO solution was suddenly frozen with liquid nitrogen and freeze-dried to get GO aerogel/Ni foam hybrid. Second, the obtained GO aerogel/Ni foam hybrid was thermally reduced to rGO aerogel/Ni foam hybrid by annealing at 400 °C for 1 h. The as-prepared rGO aerogel showed a large specific surface area of 463 m² g⁻¹ and a high electrical conductivity of 71.4 S m⁻¹. C_s of the rGO aerogel/Ni foam hybrid reached 366 F g⁻¹ at a current density of 2 A g⁻¹ and retained 186 F g⁻¹ at 20 A g⁻¹.

In another work, Yan et al. reported the capacitance performance of a 3D microchannel-network rGO foam which was prepared by using alumina fiber blanket (AFB) as sacrificial template.¹⁸⁵ In their experiments, AFB covered with GO sheets was annealed in N₂ atmosphere at 500 °C for 2 h to reduce GO.

AFB template was then etched away by hydrofluoric acid followed by washing and lyophilization. The obtained rGO foam showed a high conductivity of 13.6 S cm^{-1} and a C_s of 216 F g^{-1} at 0.5 A g^{-1} .

Gao et al. fabricated a type of paper-based transparent flexible thin film supercapacitors using cellulose nanofiber/rGO hybrid paper as electrode material and charge collector via a simple dipping-coating and HI reduction processes.¹⁸⁷ The as-prepared cellulose nanofiber/rGO hybrid paper showed a transmittance of $\sim 56\%$ (at 550 nm). An all-solid-state supercapacitor based on the cellulose nanofiber/rGO hybrid paper and $\text{H}_2\text{SO}_4/\text{PVA}$ gel electrolyte exhibited a high area capacitance of about 1.73 mF cm^{-2} , attributed to the self anti-stacking of distorted rGO sheets and internal nanoscale electrolyte reservoirs.

2.1.2 Self-supporting unitary graphene materials prepared via CVD for EDLCs

Compared to solution process, GE structures produced from CVD showed much lower defects, higher conductivity due to the absence of defects and intersheet junction contact resistance, and they could be directly used without post-treatments (reduction).^{108, 188-190} For preparing self-supporting GE structures for supercapacitor application by a CVD process, gaseous precursors (methane (CH_4), ethylene, acetylene, ethanol, hexane, etc.) are pyrolyzed on substrates (Si wafer, Ni foam, Cu foil, stainless steel mesh, etc.) to form GE films with high conductivity and low defects.¹⁹¹⁻¹⁹⁴ Miller and coworkers synthesized vertically oriented GE sheets directly on Ni substrates by radio frequency plasma-enhanced chemical vapor deposition at $1000 \text{ }^\circ\text{C}$ using CH_4 as precursor.¹⁹⁵ The vertically oriented GE sheets exhibited a large specific surface area of $\sim 1100 \text{ m}^2 \text{ g}^{-1}$. Meanwhile, the dominant exposed edge planes can greatly enhance charge storage as compared with that of traditional GE sheets relying on basal plane surfaces. Such structure can also minimize the ionic and electronic resistances and the fabricated EDLCs have RC time constants of less than 0.2 s which is much shorter than that of typical EDLCs ($\sim 1 \text{ s}$). EDLCs fabricated

from the vertically oriented GE nanosheets showed ~50% higher capacitance in the organic electrolyte (1M tetraethylammonium-tetrafluoroborate salt in propylene carbonate) than that from aqueous electrolyte (25% KOH) prototypes. The impedance phase angle of the vertically oriented GE nanosheet EDLCs reached -45° at $\sim 15,000$ Hz in comparison with 0.15 Hz for the activated carbon capacitor and $\sim 30,000$ Hz for the electrolytic capacitor. (Resistance and reactance have equal magnitudes at a phase angle of -45° , making this frequency convenient for comparison purposes.)¹⁹⁵ At 120 Hz, the impedance phase angle of the GE nanosheet EDLCs is approximately -82° which is quite near to that of the aluminum electrolytic capacitor (approximately -83°). Therefore the as-built EDLCs showed promising ability in substituting aluminum electrolytic capacitors in ac line-filtering. The study also aroused great interest in preparing vertically-oriented graphene via radio frequency plasma-enhanced chemical vapor deposition for ac line-filtering application.^{109, 196-199}

Zhang et al. reported the preparation and capacitance performance of a carpet of partially split MWCNTs and graphene nanoribbons (GNRs) prepared by longitudinally splitting vertically aligned multiwalled carbon nanotube carpets (VA-CNTs) via potassium (K) vapor.⁵³ The K vapor intercalation and subsequent methanol quenching triggered the split of VA-CNTs. Partially split regions were formed since the reaction was confined in the outer MWCNT layers. The free-standing split VA-CNT carpet was used as both a current collector and an electrode material. Compared to the pristine VA-CNT carpet, the splitting process increased the C_s value by ~ 4 folds (106.2 F g^{-1}) at a small current density ($< 10 \text{ A g}^{-1}$), and surpassed by ~ 3 folds at high current density ($> 280 \text{ A g}^{-1}$). The enhanced capacitance performance of the split VA-CNTs could be ascribed to the increased ion-accessible surface area after splitting ($191 \text{ m}^2 \text{ g}^{-1}$ before split and $308 \text{ m}^2 \text{ g}^{-1}$ after split), and the retained conductivity of the hybrid with its vertical conductive paths based on the preserved GNR alignment.

Peng and coauthors reported an in-situ unzipping approach to directly split a CNT sponge (prepared via CVD at 860 °C using a precursor solution of ferrocene in dichlorobenzene) into a GNR or GNR–CNT hybrid aerogel.⁵⁴ The unzipping process could be controlled by the amount of KMnO_4 in H_2SO_4 . The unzipping process not only converted hydrophobic CNT sponge into hydrophilic GNR aerogel, but also grafted oxygen-contained function groups onto the nanoribbon edges. After unzipping, the resulted GNR aerogel inherited the 3D network and high porosity of the original CNT sponge and displayed a bulk conductivity of 7.4 S m^{-1} which could be further improved to 36 S m^{-1} by hydrazine vapor reduction. Moreover, after unzipping, the GNR aerogel showed a specific surface area of $113.1 \text{ m}^2 \text{ g}^{-1}$ which is much larger than that of the CNT sponge ($62.8 \text{ m}^2 \text{ g}^{-1}$). The original CNT sponge showed a quite low C_s value of 15.16 F g^{-1} due to its hydrophobic property. In comparison, the C_s value of GNR aerogel increased to 92.61 F g^{-1} and could be further improved to 114.8 F g^{-1} after reduction by hydrazine vapor.

2.2 Self-supporting graphene-based carbon/carbon hybrids for EDLCs

GE and GO sheets can not only be directly built into various architectures for EDLCs application themselves, but also be fabricated with other carbon structures, such as carbon black (CB),²⁰⁰ carbon nanotube (CNT),²⁰¹ carbon nanofiber (CNF)²⁰² and other carbon materials^{55, 203, 204} to form binary or ternary carbon hybrids for EDLCs application, as showed in Table 2. Self-supporting graphene-based carbon/carbon hybrids can be prepared via either “bottom-up” or “top-down” approaches.²⁰⁵⁻²⁰⁸ In “bottom-up” approaches, including filtration, electrospray, electrophoresis, etc., building blocks like CB, CNT, CNF can function as spacers to effectively prevent GO from aggregation to maintain a suitable interlayer distance and simultaneously act as conductive channels for rapid electron transfer.^{97, 200, 203, 209-213} In “top-down” approaches, highly conductive and 3D interconnected porous GE structures prepared via

CVD are excellent substrates to support other carbon materials.^{214, 215}

2.2.1 Graphene-based carbon/carbon hybrids prepared by solution process for EDLCs

Haddon and co-workers prepared a type of single wall carbon nanotube (SWCNT)/reduced graphene oxide hybrid films by drop-casting and drying the blends of NaBH₄-reduced rGO and the purified electric arc-produced SWCNTs over a stainless steel current collector.²¹⁶ C_s of the hybrid films with same contents of SWCNT and rGO reached 222 F g⁻¹ at the current density of 1A g⁻¹ in the ionic liquid of BMIMBF₄, which is the largest value of the hybrid films with different SWCNT contents. However, C_s of pure SWCNTs and rGO was measured to be only 66 F g⁻¹ and 6 F g⁻¹, respectively. The significantly enhanced capacity of the hybrid material was attributed to the synergistic effect between SWCNTs and rGO.

In another work, Yoon et al. reported a simple approach to fabricate highly dense, opened-edge, and vertically aligned rGO/SWCNT hybrid electrodes, involving simple thermal reduction with low heating rate (0.14 °C min⁻¹ up to 1000 °C for 1 h), hand-rolling and freeze cutting processes, as showed in Fig. 9A.²¹⁷ The GO/oxidized SWCNT dispersion with less than 5_{wt}% of oxidized SWCNT was casted on a Petri dish and dried at room temperature overnight to prepare GO/oxidized SWCNT film. In the synthesis, SWCNTs function as spacers to prevent restacking of rGO sheets and to maintain a suitable interlayer distance after thermal reduction, which is beneficial to obtain high conductivity of hybrid film. After hand-rolling and freeze cutting processes, vertically aligned rGO (VArGO) /SWCNT hybrid with a high packing density (1.18 g cm⁻³) were successfully achieved. Because of their high conductivity, vertically aligned and open-edge structure, the rGO/SWCNT hybrid electrodes displayed good rate capacitance performance with rectangular CV curves even at a high scan rate of 20 V s⁻¹ (Fig. 9 B). Surprisingly, even when the film thickness of the VArGO electrode was increased, its volumetric and areal capacitances were maintained. Note that although the vertically aligned rGO/SWCNT hybrid electrode exhibited a C_s value of

only $145 \pm 1 \text{ F g}^{-1}$ at 0.5 A g^{-1} in 6 M KOH electrolyte due to its relatively low specific surface area ($123.78 \text{ m}^2 \text{ g}^{-1}$), C_s of $123 \pm 1 \text{ F cm}^{-3}$ was obtained at 20 A g^{-1} which is much better than the performance of the rGO-powder electrode ($1 \pm 1 \text{ F cm}^{-3}$ at 10 A g^{-1}) and rGO-film electrode ($2 \pm 1 \text{ F cm}^{-3}$ at 7.5 A g^{-1}) (Fig. 9C, D).

Gao et al. proposed a coaxial wet-spinning assembly approach using GO and CNT mixed dispersion as the inner spinning dope and the sodium carboxymethyl cellulose (CMC) aqueous solution as the outer spinning dope to continuously spin polyelectrolyte (CMC)-wrapped GE/CNT core-sheath fibers. The prepared carbon hybrids can be used as safe electrodes in assembling two-ply yarn supercapacitors (rGO + CNT@CMC YSC), as illustrated in Fig. 10A-C.²¹⁸ The polymer sheath of CMC is an electrically insulative but ionically conductive polyelectrolyte, which endow the fiber electrodes free of short circuit when intertwined together, while allowing ions to smoothly penetrate into the electrodes simultaneously. The CMC sheath can also enhance the mechanical strength of the resulting rGO@CMC coaxial fiber (tensile stress is about 70 MPa). On the other hand, the introduction of CNTs into rGO sheets can prevent the aggregation of rGO sheets and greatly enhance the ion-accessible surface area of the core fibers, which is beneficial for improving energy storage of GE+CNT hybrid fibers when used as yarn supercapacitor electrodes. The rGO+CNT@CMC YSCs showed much better capacitance performance with specific area capacitance of 177 mF cm^{-2} at 0.1 mA cm^{-2} compared to the values of CNT@CMC YSCs (47 mF cm^{-2}) and rGO@CMC YSCs (127 mF cm^{-2}) with $\text{H}_3\text{PO}_4/\text{PVA}$ solid electrolyte. The capacitance of the rGO+CNT@CMC YSCs could be further largely improved to 269 mF cm^{-2} by using liquid electrolyte ($1 \text{ M H}_2\text{SO}_4$ aqueous solution). The coaxial fiber YSCs were flexible and robust enough to endure the repeated and long-term bending and the capacitance only dropped 2% at 200 cycles of bending and rose persistently to 111% at 1,000 cycles of bending. More significantly, a cloth supercapacitor superior to

commercial capacitor was further woven from two 0.4 m-long coaxial rGO+CNT@CMC fibers. The cloth supercapacitor could work under different bending states, as illustrated in Fig. 10D and E. The combination of scalable coaxial wet-spinning technology and excellent performance of yarn supercapacitors paves a way to wearable and safe electronics.²¹⁸

2.2.2 Graphene-based carbon/carbon hybrids prepared by CVD for EDLCs

3D interconnected porous GE structures prepared by CVD are another type of high conductive substrates to support other carbon materials for application in EDLCs.²¹⁹ Yan et al. reported the preparation and capacitance performance of vertical CNT forests/GE hybrid with seamless contact on Ni foam via two-step CVD process using CH₄ and ethylene as carbon sources.²²⁰ In the hybrid structure, GE serves as a linking agent between the CNT/metal interfaces which offers better interfacial contacts. However, due to the hydrophobic property, a relatively low C_s of 104 F g⁻¹ was obtained from the composite at 0.2 A g⁻¹ in 6 M KOH electrolyte.

Wang et al. reported a one-step ambient pressure CVD process for the simple and scalable fabrication of 3D few-layer GE/MWCNT hybrid nanostructures on Ni foam using acetylene (C₂H₂) as carbon source.²²¹ The as-grown GE/MWCNT hybrid nanostructures exhibited a large specific surface area of 743 m² g⁻¹. However, the pristine GE/MWCNT hybrid is hydrophobic with a large contact angle of 142°, resulting in a low C_s of 55 F g⁻¹ at 50 mV s⁻¹ in 6 M KOH electrolyte. To enhance the surface wettability, the as-prepared GE/MWCNT hybrid was soaked in 6 M KOH aqueous at 80 °C to mildly activate the surface properties of the carbon hybrid. The post-treated GE/MWCNT hybrid showed a much smaller contact angle of 18° and greatly improved capacitance performance (233 F g⁻¹ at 50 mV s⁻¹). Therefore, surface wettability is significantly important for enhancing the capacitance performance of CVD-prepared carbon materials.

Recently, Zhi et al. reported the fabrication and capacitance performance of silver nanowires/3D-graphene foam/ordered mesoporous carbon composite (Ag-GF-OMC).¹⁹⁰ GE foam was prepared by CVD at 1000 °C using Ni foam as template and CH₄ as carbon source. The specific surface area of the Ag-GF-OMC reached 484 m² g⁻¹ which is higher than those of pristine OMC (312 m² g⁻¹) and GF-OMC (405 m² g⁻¹). The Ag-GF-OMC hybrid exhibited good mechanical strength and high electrical conductivity up to 762 S cm⁻¹ which is much larger than that of GF-OMC (413 S cm⁻¹). The flexible supercapacitors based on Ag-GF-OMC electrodes displayed a much higher C_s of 213 F g⁻¹ in 6 M KOH aqueous electrolyte compared to the pristine OMC electrode (39 F g⁻¹) and GF-OMC (139 F g⁻¹).

2.3 Self-supporting functionalized graphene materials for EDLCs

Pristine graphene sheets are hydrophobic in nature, which leads to most of their surface area ions-inaccessible and results in poor capacitance performance.²²² Therefore it is necessary to modulate the electronic structure, surface and local chemical environment of GE for novel device application.²²³ However, surface-functionalization of pristine graphene sheets is very difficult, if not impossible, due to its chemical stability and poor solubility.^{224, 225} As an alternative way, the solution-processable GO sheet with reactive oxygen-containing groups at both the edge and basal plane is one of the most popular and more practical raw materials for functionalization of graphene.²²⁶⁻²²⁸ There are mainly two approaches for functionalization of GE sheets: doping with heteroatoms (nitrogen, boron, sulfur, phosphorus, etc.)^{163, 229-233} and modifying with compounds (hydroquinone, 1-pyrenecarboxylic acid, 2-aminoanthraquinone, benzoxazole, benzimidazole, etc.).²³⁴⁻²³⁷ Both methods can ameliorate the surface chemical properties and avoid the aggregation of GE sheets.²³⁸ Therefore, the utilization ratio of GE sheets can be boosted and thus their capacitance performance can be enhanced through surface functionalization. Besides, the

functionalization of GE often introduces partial pseudocapacitance to the total capacitance of GE-based materials.²³⁹⁻²⁴¹

2.3.1 Heteroatom-doped self-supporting graphene materials for EDLCs

As illustrated in Fig. 11, Li et al. demonstrated the direct synthesis of hybrid carbon (N-GE/PC) films woven from nitrogen-doped multi-layer GE/porous carbon by CVD on Ni gauze templates with CH₄ as carbon source and ammonia as nitrogen source.²⁴² The N-GE/PC core-shell hybrids exhibited a uniform and continuous structure and the structural parameters, including density, pore size distribution and purity of the carbon could be adjusted by tuning the feeding rates of CH₄ and reaction time. The capacitance performance of the N-GE/PC hybrids was greatly influenced by the diameter of Ni wires. It was found that small-diameter N-GE/PC hybrids are preferred for EDLCs application, with the specific area capacitance of 23.4 $\mu\text{F cm}^{-2}$ for wires with diameter of 35 μm . C_s of the N-GE/PC hybrids reached 173 F g⁻¹ in 1 M Na₂SO₄, which is about 150% higher than that of the undoped GE/PC-film-based counterparts.

Yu et al. developed a scalable method to continuously produce a hierarchical structured carbon microfiber.⁹⁵ The hybrid was fabricated by an interconnected network of aligned SWCNTs with interposed nitrogen-doped rGO sheets via using a silica capillary column as a hydrothermal microreactor, as shown in Fig. 12A and B. In the synthesis, different mass ratio of nitric-acid-oxidized SWCNTs and GO were mixed to form hybrid microfibers with ethylenediamine (EDA) as both the nitrogen dopant and reduction agent for GO sheets during the hydrothermal process. It was found that continuous hybrid fibers can not be formed when the mass ratio of GO is below 50 wt%, and the density, specific surface area and the conductivity of the resulting hybrid fibers increased with increasing SWNTs fraction, but the tensile strength decreased from ~200 MPa to ~75 MPa with the addition of SWNTs fraction. Such method for preparation of SWCNT/rGO hybrid fibers has the following advantages. Firstly, in the hybrid, GO serves

as a good surfactant to disperse SWNTs, while oxidized SWCNTs can efficiently hinder the restacking of rGO sheets and offer a 3D conductive network simultaneously (Fig. 12C and D). Secondly, N-doping can not only enhance the wettability of rGO sheets, but also contribute pseudocapacitance to the total capacitance. Thirdly, EDA could function as a molecular “end-anchoring” reagent to bind the oxidized SWNTs and GO.²⁴³ Among all the hybrid fibers, the hybrid fiber with 50 wt% oxidized SWCNTs and 2.8 at% of nitrogen element (fiber 3) showed the best structure character with the largest specific surface area of $396 \text{ m}^2 \text{ g}^{-1}$, the highest electrical conductivity of 102 S cm^{-1} and the biggest density of $0.59 \pm 0.04 \text{ g cm}^{-3}$ and therefore displayed the best capacitance performance. The fiber 3 showed a large specific volumetric capacitance of 305 F cm^{-3} in H_2SO_4 electrolyte or 300 F cm^{-3} in PVA/ H_3PO_4 solid-state electrolyte (Fig. 12E). An all-solid-state micro-supercapacitor with PVA/ H_3PO_4 gel electrolyte, free from binder, current collector and separator, exhibited a high volumetric energy density of $\sim 6.3 \text{ mWh cm}^{-3}$ which is comparable to that of 4 V–500 μAh thin-film lithium batteries. Moreover, the supercapacitor showed a high power density more than 100 folds higher than that of batteries, as well as good rate capability and a long cycle life.

Qu et al. prepared a type of ultralight and N-doped graphene aerogel by hydrothermal assembling of GO solution in the presence of pyrrole, followed by freeze-drying and high-temperature calcining the as-prepared rGO hydrogel.²²³ Pyrrole molecule not only acted as nitrogen source for nitrogen doping, but also played an important role in the formation of 3D porous GO hydrogel. Pyrrole molecule has a typical conjugated structure with electron-rich N atom, and it could be easily anchored on the surface and edge of GO sheets through hydrogen-bonding and π - π interaction. Therefore, the presence of pyrrole could effectively prevent the self-stacking of GO sheets during hydrothermal process, and accordingly increase the available GO sheets for forming large volume 3D GO hydrogel with thin connection walls.²²³ The

as-prepared porous N-doped GE aerogel with N/C atomic ratio of 4.9% showed a ultralight density of $2.1 \pm 0.3 \text{ mg cm}^{-3}$, high conductivity of $1.2 \pm 0.2 \times 10^3 \text{ S m}^{-1}$, and a relatively high specific surface area of approximately $280 \text{ m}^2 \text{ g}^{-1}$. The excellent structure characters and outstanding physical properties endow the ultralight N-doped GE aerogel with good capacitance performance. C_s of the N-doped GE aerogel reached 484 F g^{-1} at 1 A g^{-1} which is very close to the theoretical electrical double-layer capacitance of 550 F g^{-1} of pure GE and 415 F g^{-1} of C_s was maintained at 100 A g^{-1} . Moreover, the ultralight N-doped GE aerogel also showed good performances in inflaming retarding, high-efficiency adsorption and efficient catalysis for oxygen reduction reaction.

Through hydrothermal reaction and freeze-drying processes, Wu et al. demonstrated a simplified prototype device of high-performance all-solid-state supercapacitor based on 3D nitrogen and boron co-doped monolithic GE aerogels using GO and ammonia boron trifluoride (NH_3BF_3) as precursors.²⁴⁴ The nitrogen and boron co-doping in carbon networks could facilitate charge transfer between neighboring carbon atoms and thus enhance the electrochemical performance of carbon-based materials.^{245, 246} By directly pressing the as-prepared macroporous B, N-codoped GE aerogel, electrode with a 3D interconnected architecture could be fabricated under physical pressure, which is favorable for electron transport and ion diffusion in bulk electrode. The B, N-codoped GE aerogel incorporated with $\sim 3.0\%_{\text{at}}$ nitrogen element and $\sim 0.6\%_{\text{at}}$ boron element exhibited a moderate specific surface area of $249.0 \text{ m}^2 \text{ g}^{-1}$. The all-solid-state supercapacitor based on B, N-codoped GE aerogel and PVA/ H_2SO_4 gel electrolyte delivered specific capacitance of 62 F g^{-1} at 5 mV s^{-1} which is larger than those of undoped GE aerogel (43 F g^{-1}), N-doped GE aerogel (52 F g^{-1}), B-doped GE aerogel (55 F g^{-1}) and undoped GE paper (29 F g^{-1}).

2.3.2 Self-supporting graphene materials functionalized with small molecules for EDLCs

Wu et al. studied the capacitance performance of a functionalized rGO hydrogel. In the experiments,

rGO sheets were covalently grafted by redox active small organic molecules of 2-aminoanthraquinone (AAQ).²⁴¹ The AAQ-modified rGO hydrogel displayed a specific capacitance of 258 F g^{-1} at 0.3 A g^{-1} which is about 133.7% the value of pristine rGO hydrogel (193 F g^{-1}). The improved capacitance of the modified rGO hydrogel was attributed to the pseudocapacitance of AAQ molecules. Due to the 3D porous structure of rGO hydrogel and good conductivity of rGO sheets, the functionalized rGO hydrogel could retain a larger specific capacitance compared to the unmodified counterpart even at a high current density of 90 A g^{-1} .

Ghosh et al. reported the preparation and capacitance performance of 1-pyrenecarboxylic acid (PCA)-functionalized graphene film.²²⁵ In their experiments, graphene flakes were wedged out of graphite powder with the help of molecular wedge of PCA in a mixture of methanol and water. The resulting GE dispersion was then filtered to get PCA-functionalized free-standing GE film. The large-scale sp^2 hybridized C–C network in GE layer was not disrupted via this approach, which reserved the high conductivity of GE flakes. PCA is an amphiphilic functional agent. In the PCA-functionalized graphene, GE sheets were π -functionalized with the hydrophobic aromatic hydrocarbons of PCA and the hydrophilic –COOH groups of PCA dangled out-of plane from the GE surface, making GE surface accessible by KOH aqueous electrolyte. The PCA-modified GE film exhibited significantly enhanced capacitance performance compared to the non-functionalized GE film. The specific capacitance of PCA-modified GE film ($\sim 200 \text{ F g}^{-1}$) is more than six folds of the value of pristine GE film ($\sim 30 \text{ F g}^{-1}$).

Duan and coworkers reported the synthesis of 3D interconnected and functionalized GE hydrogels through a convenient one-step hydrothermal assembling process of GO using hydroquinones as the reducing and functionalizing molecules simultaneously.²⁴⁷ The specific surface area of the functionalized GE hydrogel reached $\sim 1380 \text{ m}^2 \text{ g}^{-1}$ by the methylene blue (MB) dye adsorption method and $\sim 297 \text{ m}^2 \text{ g}^{-1}$

was retained for the freeze-dried sample. The as-prepared functionalized GE hydrogels displayed good mechanical strength and could be used directly as the supercapacitor electrodes. The mass loading of hydroquinone on the functionalized GE hydrogels was estimated to be about 17 wt%. Electrochemical tests unraveled the coexistence of both pseudocapacitance and the electrical double-layer capacitance. A C_s of 441 F g⁻¹ was obtained from the functionalized GE hydrogels at 1 A g⁻¹ in 1 M H₂SO₄ electrolyte, which is more than two-fold the value of unfunctionalized GE hydrogels (211 F g⁻¹). The flexible all-solid-state supercapacitor based on the functionalized GE hydrogels and PVA/H₂SO₄ gel electrolyte showed a large C_s value of 412 F g⁻¹ at 1 A g⁻¹, 74% capacitance retention at 20 A g⁻¹ and 87% capacitance retention after 10 000 cycles.

3. Free-standing graphene hybrids for pseudocapacitors (PCs)

3.1 Free-standing graphene/conducting polymer hybrids for PCs

Conducting polymers including polyaniline (PANI), polypyrrole (PPy), polythiophene (PTh), are one type of important electrode materials for pseudocapacitors attributing to their large theoretical capacitance, ease of synthesis, good electric conductivity and low cost.^{27, 248-252} Generally, conducting polymers have several redox states and can be polymerized either chemically or electrochemically from the relevant monomers.^{24, 253, 254} The electrical conductivity of conducting polymers can be controlled over the full range from insulator to metal by doping.²⁵⁵ However, the supercapacitors based on conducting polymers often show poor cyclic stability and unsatisfied specific capacitance values which are far below their theoretical capacitance. The low capacitance performance could be ascribed to the low utilization ratio and poor mechanical stability caused by volumetric changes in the doping/dedoping process.²⁵⁶ In order to improve the capacitance performance of conducting polymer-based supercapacitors, researchers preferred

to grow nanostructured conducting polymers on conductive carbon substrates.^{21, 257-261} In this case, carbon substrates offer a conductive pathway for rapid electron transfer and the volumetric changes are greatly restricted. Therefore, conducting polymers/carbon composites usually show improved stability and rate performance compared to pristine conducting polymers.^{248, 262} Self-supporting GE structures are excellent substrates in hosting conducting polymers attributing to their controllable structures, large surface area, good conductivity and robust mechanical property. The capacitance performances of some binder-free GE/conducting polymer hybrid electrodes are summarized in Table 3.⁸⁸

3.1.1 Free-standing graphene/polyaniline hybrids for PCs

Among the studied conducting polymers, PANI has been considered as the most useful one for supercapacitor application due to its versatile preparation methods, high conductivity and multiple redox states. PANI-based electrode exhibited the largest theoretical pseudocapacitance ($\sim 2000 \text{ F g}^{-1}$ in H_2SO_4 electrolyte) among all the conducting polymers.^{11, 263} The preparation and capacitance performances of various free-standing PANI/GE composites have been extensively studied in the past few years.^{23, 261, 264, 265} The results demonstrated that binder-free and self-supported PANI/GE hybrids showed improved specific capacitance, rate performance and cyclic stability compared to pristine PANI structure and the composites are promising electrode materials for pseudocapacitors.^{262, 266}

Cong et al. reported the preparation and capacitance performance of a flexible PANI/rGO composite paper which was fabricated by electrodeposition of uniform PANI nanorods on highly conductive rGO paper, as illustrated in Fig. 13A.²⁶² The rGO paper with a low density of 0.2 g cm^{-3} and a high conductivity of $15 \text{ } \Omega \text{ sq}^{-1}$ was first prepared by one-step HI reduction-solution assembly method. The content of PANI in PANI/rGO composite paper could be simply adjusted by changing the electropolymerization time (Fig. 13B). The PANI/rGO composite paper with 22.3 wt% of PANI exhibited a much larger C_s of 763 F g^{-1} at 1

A g^{-1} compared to the value of rGO paper (180 F g^{-1}) and PANI film (520 F g^{-1}). Moreover, the PANI/rGO paper electrode presented a better cyclic stability with a capacitive retention of 82 % after 1000 cycles in comparison with 51.9 % of PANI film electrode.

Wang and co-workers reported the preparation of PANI deposited on the oriented graphene hydrogel (OGH) film via in situ chemical polymerization.²⁶⁷ The as-prepared PANI@OGH film showed good mechanical strength with Young's modulus of $140 \pm 10 \text{ MPa}$, about 4 times that of the OGH film. The authors found that the coating thickness of PANI and the porous structure have great influence on the capacitance performance of the resulting PANI/OGH film. The coating thickness of PANI was controlled by the polymerization time and the PANI@OGH film with 48_{wt}% PANI offered the highest specific capacitance of 530 F g^{-1} at 10 A g^{-1} (based on the total weight of PANI and rGO) among the studied four samples. The C_s of PANI@OGH film with 48_{wt}% PANI was estimated to be in the range of 938 to 1104 F g^{-1} at 10 A g^{-1} which is larger than its freeze-dried counterpart (780 to 910 F g^{-1}) at the same condition. Remarkably, the PANI@OGH film with 48_{wt}% PANI showed good rate performance with a capacitance retention ratio of 96% at 100 A g^{-1} and excellent stability with 93% capacitance retained even being cycled at 100 A g^{-1} for 10,000 cycles.

High conductive and porous GE networks prepared by CVD are also good substrates for PANI-based nanostructures.^{20, 268, 269} Kulkarni et al. reported the capacitance performance of PANI nanofibers/GE framework in $1 \text{ M H}_2\text{SO}_4$ electrolyte.²⁷⁰ In the synthesis, PANI nanofibers were deposited on 3D porous GE framework (prepared by CVD at $1000 \text{ }^\circ\text{C}$ using CH_4 as carbon source) by in situ chemical polymerization. The PANI/GE showed much higher capacitance of 1002 F g^{-1} than the PANI deposited on stainless steel (435 F g^{-1}) and good stability with 86.5% capacitance retained after 5000 cycles at 4 mA cm^{-2} .

3.1.2 Hybrids of free-standing graphene with other conducting polymers for PCs

In addition to PANI, PPy is another type of most studied conducting polymers for supercapacitor application and a lot of work has been conducted on the preparation and capacitance performance research of binder-free PPy/GE composites.²⁷¹⁻²⁷³ Generally, self-supported PPy/GE hybrids fabricated by in situ polymerization often show enhanced capacitance performance compared to the counterparts built through layer-by-layer assembly, filter, etc. with rGO sheets and PPy nanostructures prepared in advance.²⁷⁴⁻²⁷⁶ The improved capacitance performance can be attributed to the greatly reduced contact resistance in the interface between PPy and GE (rGO). Zhao et al. demonstrated the preparation and capacitance performance of highly compression-tolerant PPy/rGO hydrogel, as shown in Fig. 14.⁹³ In the preparation, pyrrole (Py) monomer was introduced into the hydrothermal assembly of rGO hydrogel. After reduction process, the as-prepared Py-contained rGO hydrogel was electrochemically polymerized to form PPy/rGO hydrogel. The introduction of Py in the hydrothermal process can effectively prevent the restacking of GO sheets, which is beneficial for the formation of highly elastic 3D PPy/rGO hydrogel with maximized surface area. The freeze-dried PPy/rGO hydrogel exhibited a S_A of $144 \text{ m}^2 \text{ g}^{-1}$ and a high electrical conductivity of about $3 \times 10^3 \text{ S m}^{-1}$. The specific capacitance of PPy/rGO hydrogel reached 350 F g^{-1} at 1.5 A g^{-1} in 3 M NaClO_4 electrolyte, which is much larger than that of compact PPy film (ca. 50 F g^{-1}) and pure 3D graphene (151 F g^{-1}). Moreover, the supercapacitor based on PPy/rGO hydrogel displayed excellent stability with no significant variant in the CV curves under 50% compression and after 1000 cycles.

Ding et al. developed a facile and straightforward approach to continuously fabricate highly conductive and mechanically flexible rGO/PPy hybrid fibers with a measured tensile strength of up to 80 MPa via wet-spinning strategy.²⁶ Flexible and lightweight fiber electrodes can be fabricated from the rGO/PPy

hybrid fibers for supercapacitor. The GO/PPy composite fibers were first prepared by wet spinning hybrid dispersion of GO and PPy in FeCl_3 solution via a needle of single-capillary with different diameter. After dried at room temperature, the GO/PPy composite fibers were reduced to rGO/PPy composite fibers by dipping into HI solution at 80°C for 8 h. The authors also studied the influence of the diameter of rGO/PPy fibers on the capacitance performance. It was found that the rGO/PPy composite fiber with a diameter of $35\ \mu\text{m}$ exhibited the best capacitance performance of $115\ \text{mF cm}^{-2}$ at $0.2\ \text{mA cm}^{-2}$ in $1\ \text{M NaClO}_4$ electrolyte and $107.2\ \text{mF/cm}^2$ at $0.24\ \text{mA cm}^{-2}$ in H_2SO_4 -PVA gel electrolyte.

Chen et al. presented an approach to prepare GO/PPy nanowire film for supercapacitor application.²⁴ A microporous Al_2O_3 film was used as template to mold electrodeposited GO/PPy composite and the GO/PPy nanowire film was left after removing the Al_2O_3 template. Attributed to the higher conductivity, larger ion-accessible surface area and the intimate contact between the GO/PPy nanowires and substrate, the synthesized GO/PPy nanowire film showed enhanced capacitance performance compared to PPy nanowire film. The GO/PPy nanowire film with GO mass percent of 30% exhibited the largest specific capacitance of $960\ \text{F g}^{-1}$ among all the composite films at $10\ \text{mV s}^{-1}$ in $1\ \text{M NaCl}$ electrolyte which is six times that of the pure PPy nanowires ($\sim 160\ \text{F g}^{-1}$).

Apart from PANI and PPy, poly (3, 4-ethylenedioxythiophene) (PEDOT), a representative of thiophene-type conducting polymer, is another good candidate for supercapacitor applications attributed to its controllable electrical conductivity and environmental stability.^{27,28} Chu et al. reported the capacitance performance of a self-supported PEDOT/GE hybrid which was prepared by electrodeposition of PEDOT on GE paper supported by carbon fiber cloth.²⁷ The specific capacitance of the hybrid decreases with the increase of electrodeposition time, and a maximum value of $714.93\ \text{F g}^{-1}$ was achieved for the sample with a deposition time of 3 min.

3.2 Free-standing graphene/transition metal compound hybrids for PCs

Transition metal compounds including oxides, hydroxides and sulfides are another type of pseudocapacitor electrode materials which possess theoretical specific capacitance larger than 1000 F g^{-1} .⁸⁹ Except high price ruthenium oxide, compounds of other transition metals (Ni, Co, Mn, Fe, V, Mo, etc.) traditionally used in pseudocapacitors are relatively low-cost and can be tuned into various nanostructures.^{18, 278-288, 289-296} However, pure transition metal compounds often suffer from low electrical conductivity, poor mechanical strength and inferior stability. Combining with highly conductive and porous GE frameworks is an effective approach to enhance the capacitance performance of transition metal compounds. Table 4 summarizes the capacitance performances of various binder-free GE/transition metal compounds.

3.2.1 Free-standing graphene/MnO₂ hybrids for PCs

Compared to other transition metal compounds, manganese dioxide (MnO₂) shows many advantages: a high theoretical specific capacitance of 1370 F g^{-1} , low cost, environmental friendliness, easy preparation and controllable nanostructures.²⁹⁷ Remarkably, MnO₂/C composites with intimate contact can be obtained via a simple but effective in situ redox reaction between MnO_4^- and carbon.^{91, 298-300} In these hybrid materials, the contact resistance between MnO₂ and carbon substrates can be greatly reduced, which could result in high utilization ratio of MnO₂ and good rate performance.³⁰¹⁻³⁰³ Moreover, MnO₂-based electrodes can be tested in “green” and mild aqueous electrolytes (mostly Na₂SO₄ electrolyte), resulting in low corrosion of supercapacitors and littler pollution to the environment.

Various free-standing MnO₂/GE hybrids have been prepared and they showed good performance for pseudocapacitors.³⁰⁴⁻³⁰⁸ Flexible electrical insulators including cellulose paper, cotton textiles, polyamide-66 nanofabrics, commercial sponges, polyester textiles, can be converted to electrical

conductive substrates via coating a layer of CNTs or GO film.^{116, 133, 187, 309-311} Low cost, high mechanical strength, good flexibility and high porosity of the pristine electrical-insulating materials and the simple preparation of corresponding electrical-conductive counterparts endow these hybrid materials important roles in fabricating flexible electrodes for supercapacitors.^{17, 212, 312-316} Ge et al. reported the synthesis of rGO/MnO₂ composites supported on commercial polyester fiber sponge (Sponge@rGO@MnO₂).³¹⁷ The fabrication process is illustrated in Fig. 15a. Commercial polyester fiber sponge with 3D interconnected porous structure (Fig. 15b and e) was used as flexible skeleton to host GO sheets via a simple and low-cost “dip and dry” process. The as-prepared sponge@GO was then converted to sponge@rGO by HI reduction (Fig. 15c and f). Supercapacitor based on the sponge@rGO showed a high power density of 94 kW kg⁻¹ and an ultralarge scan rate of 200 V s⁻¹. By repeating the dipping process in Mn(CH₃COO)₂ and KMnO₄ solution in sequence, flower-like MnO₂ particles were deposited on the sponge@rGO (Fig. 15d and g). The sponge@rGO@MnO₂ with three repeated dipping processes showed the best capacitance performance among all the composites with a C_s value of 450 F g⁻¹ at 2 mV s⁻¹, high power density of 47 kW kg⁻¹ and good stability with ~90% capacitance retained after 10,000 cycles under 10 V s⁻¹.

Cheng et al. reported the preparation and capacitance performance of conductive, highly flexible, compact and mechanically robust GE/MnO₂/CNTs nanocomposite films.³¹⁸ The hybrid films were prepared by filtering mixed solutions of desired amounts of functionalized few-walled carbon nanotubes (fFWNTs) suspension and GE/MnO₂ dispersion. In the hybrid films, GE sheets function as high surface area and conductive substrate to support MnO₂ nanostructure and CNTs offer interconnected conductive networks among GE/MnO₂ nanosheets, which can prevent the aggregation of GE/MnO₂ nanosheets and ensure the fully utilization of MnO₂ simultaneously. The incorporation of CNTs plays a vital role for the performance of the resulting hybrid films. GE/MnO₂ without fFWNTs could not form a continuous and

flexible film by filtering. A GE/MnO₂/CNTs film with 25_{wt}% of CNTs and a thickness of 30 μm showed superior mechanical properties with a Young's modulus of 2.3 GPa and a tensile strength of 48 MPa. The GE/MnO₂/CNTs films could be directly used as electrodes for supercapacitor without current collectors and binders. The specific capacitances of the GE/MnO₂/CNTs electrode with 25_{wt}% of CNTs were measured to be 326 F g⁻¹ at 10 mV s⁻¹ and 148 F g⁻¹ at 500 mV s⁻¹. Moreover, the flexible film electrode exhibited no obvious change in electrochemical properties under shape deformation. Meanwhile, the film electrode showed only about 5% capacitance loss after 1000 cycles at 4 A g⁻¹. A rod-shaped capacitor could be assembled by rolling up two GE/MnO₂/CNTs films and the specific capacitance of the full cell reached 70 F g⁻¹ at 10 mV s⁻¹. The maximum power density of the assembled full cell can reach 170 kW kg⁻¹ based on the mass of GE/MnO₂/CNTs films and 42 kW kg⁻¹ based on the total mass of the whole cell.

He et al. studied the capacitance performance of the freestanding and flexible MnO₂/GE composites fabricated by electrodeposition of MnO₂ on GE framework.³¹⁹ In this work, GE was first prepared via CVD at 1000 °C with Ni foam as catalyst and template and CH₄ as carbon source. The 3D freestanding, lightweight (0.7 to 0.75 mg cm⁻²), porous, ultrathin (<200 μm), flexible and highly conductive (55 S cm⁻¹) GE network is an excellent substrate to support MnO₂ nanostructure. The mass loading of MnO₂ could be simply adjusted by controlling the deposition time and current, and an ultralarge mass percent of 92.9% MnO₂ was achieved. A gravimetric specific capacitance of 465 F g⁻¹ was obtained from the MnO₂/GE hybrids with a MnO₂ mass loading of 0.1 mg cm⁻² at 2 mV s⁻¹. It was also found that the gravimetric specific capacitance decreases with increasing MnO₂ mass percent due to the increased resistance and decreased utilization of MnO₂.

To improve the mass loading of MnO₂ so as to increase the area specific capacitance, CNTs or carbon nanofibers (CNFs) can be grown on GE networks to act as additional conductive substrate.^{12, 202, 320, 321}

Wang et al. fabricated a GE/MWNT/MnO₂ nanowire (GMM) hybrid foam via a two-step approach.³²² Firstly, the conductive GE/MWNT (GM) foam was deposited on Ni foam by a one-step ambient pressure CVD process using C₂H₂ as carbon source. Secondly, α -MnO₂ nanowires synthesized by hydrothermal process were conformally coated onto UV-ozone treated GM foam by bath deposition. In the hybrid structure, the few-layer GE foam functioned as both a current collector and a buffer layer which boosted the charge transfer from active materials (MnO₂ nanowires and CNTs) to current collectors and endowed the electrochemical stability of Ni foam by isolating it from the electrolyte. In addition, the embedment of CNTs roots into the GE layer provided a seamless connection between CNTs and GE film, which can reduce the contact resistance and enhance the mechanical stability of the hybrid simultaneously. Symmetrical supercapacitor based on the GMM foam exhibited a broad operational voltage window of 1.6 V in 2 M Li₂SO₄ aqueous electrolyte. An ultralarge C_s value of 1108.79 F g⁻¹ was achieved at 1.89 A g⁻¹ along with a superior energy density of 391.7 Wh kg⁻¹. Moreover, the supercapacitor based on GMM foam also exhibited an ultrahigh power density of 799.84 kW kg⁻¹ and excellent stability with 97.94% capacitance retention after 13000 cycles.

3.2.2 Hybrids of free-standing graphene with other transition metal compounds for PCs

Besides MnO₂, other transition metal compounds including Co₂O₃, Co₃O₄, Co(OH)₂, Co₃S₄, NiO, Ni(OH)₂, Ni₃S₂, NiCo₂O₄, Fe₃O₄, V₂O₅, RuO₂, etc. are also promising electrode materials contributing pseudocapacitance to supercapacitors.^{279, 280, 282, 290} By combining with GE to build self-supporting structures, the resulting hybrids often show improved performances in power density, rate performance and cyclic stability.³²³⁻³³²

Cao et al. reported the capacitance performance of a NiO/GE foam hybrid prepared by electrodeposition of petal-like NiO film on GE foam.³³³ The 3D porous and conductive GE foam was obtained via CVD

using ethanol as carbon source and Ni foam as catalyst and sacrificial template. The obtained NiO/GE composite showed a high specific capacitance of $\sim 816 \text{ F g}^{-1}$ at 5 mV s^{-1} which is more than twice that of NiO/Ni foam (305 F g^{-1}). Dong et al. prepared a Co_3O_4 nanowires/GE foam composite via a hydrothermal procedure by using the same GE foam substrate.¹⁴ The 3D hierarchical porous structure of Co_3O_4 nanowires/GE foam and the rough surface of individual Co_3O_4 nanowires together offered a large accessible surface area endowing the high utilization of Co_3O_4 . C_s of the composite reached 768 F g^{-1} at 10 A g^{-1} and was further increased to $\sim 1100 \text{ F g}^{-1}$ after 500 cycles due to electrochemical activation.

Wang et al. synthesized a NiO/GE foam composite by hydrothermal growth of NiO nanoflakes on 3D graphene scaffolds.³³³ 3D graphene was first prepared by microwave plasma enhanced chemical vapor deposition (MPCVD) using Ni foam as catalyst and template and CH_4 as carbon source. The preparation process is illustrated in Fig. 16. Typically, 3D GE was deposited on the surface of Ni foam via the MPCVD system which was different from the 2D GE sheets obtained from traditionally CVD process. In the hydrothermal procedure, different concentrations of NiCl_2 solution were used to tune the structure of NiO. The results revealed that the NiO/GE foam prepared from 40 mM NiCl_2 solution (NGC-40 mM) showed the best capacitance performance. The NGC-40 mM with a specific surface area of $227.2 \text{ m}^2 \text{ g}^{-1}$ exhibited a high C_s of $\approx 1829 \text{ F g}^{-1}$ at 3 A g^{-1} and a large energy density of 138 Wh kg^{-1} in 1 M NaOH electrolyte. Moreover, the NGC-40 mM also showed good stability with capacitance retention of 81% after 5000 cycles at 15 A g^{-1} .

Shim et al. reported the capacitance performance of a 3D ternary system based on $\text{NiCo}_2\text{O}_4/\text{rGO}/\text{Ni}$ foam hybrid prepared by two-step electrodeposition and a thermal transformation process.¹⁵ In this system, NiCo_2O_4 nanoparticles with small size of 3 to 5 nm were deposited on the thin rGO nanosheets. The small size ensured the full utilization of NiCo_2O_4 nanoparticles and thus resulted in high pseudocapacitance. The

large surface area and high conductivity of rGO are favorable for the high mass loading of NiCo_2O_4 nanoparticles and rapid electron and ion transport. The hybrid showed a high specific capacitance of 2260 F g^{-1} at current densities of 1 A g^{-1} and good stability with 92.8% capacitance retention after 10000 cycles at 3 A g^{-1} .

In another work, Wang et al. studied the preparation and capacitance performance of a 3D $\text{RuO}_2/\text{CNT}/\text{GE}/\text{Ni}$ foam composite.³³⁴ The CNT/GE/Ni foam hybrid was prepared by depositing CNT/GE layer on Ni foam via one-step CVD process using C_2H_2 as carbon source. The CNT/GE/Ni foam hybrid then functioned as substrate to hold the ultra-fine hydrous RuO_2 crystalline with size around 1-2 nm through a simple dip-coating process. Excellent capacitance performance was achieved from the $\text{RuO}_2/\text{CNT}/\text{GE}/\text{Ni}$ foam composite ascribed to the hierarchical and porous structure, the seamless connected CNT/GE conductive framework and ultra-fine size of hydrous RuO_2 crystalline. Symmetric supercapacitor based on the $\text{RuO}_2/\text{CNT}/\text{GE}/\text{Ni}$ foam composite could be cycled reversibly in a wide voltage window of 1.5 V in 2 M Li_2SO_4 electrolyte which is much larger than the majority voltage window in aqueous electrolyte ($\sim 1.0 \text{ V}$). A high C_s value of 502.78 F g^{-1} and a large energy density of 39.28 Wh kg^{-1} were obtained from the as-built supercapacitor.

4. Binder-free graphene-based asymmetric supercapacitors

Generally, electrical double layer capacitors show high power density but low energy density while pseudocapacitors exhibit high energy density but low power density. In order to explore supercapacitors with both high energy density and power density, a new configuration of supercapacitor was developed which is named asymmetric supercapacitor (ASC).^{34, 335-337} In a typical ASC, two types of different electrode materials working in different electrochemical potential ranges are used: one shows high power

density but low energy density (mainly carbon materials), another one displays high energy density but low power density (conducting polymers and/or transition metal compounds).³³⁸⁻³⁴¹ Compared with conventional symmetric SCs, ASCs can take advantage of the different potential windows of the two electrodes to broaden the maximum operating voltage of a cell system above 1.5 V, leading to a remarkable improvement in E and W.^{101, 342, 343} Table 5 summarizes the capacitance performances of various asymmetric supercapacitors fabricated from binder-free GE-based materials.

Attributed to aforementioned advantages, GE and its composites also show excellent performance in the application of ASC.^{131, 310, 344-346} For instance, Lee et al. fabricated a prototype of flexible, asymmetric supercapacitor device with high areal capacitance by using rGO/MnO₂ paper as positive electrode and rGO paper as negative electrode.³⁴⁷ The capacitance performance was tested between 0 and 1.5 V in 1 M Na₂SO₄ electrolyte. The rGO/MnO₂ paper was fabricated by well-separated and continuously aligned rGO/MnO₂ sheets. The dynamic mechanical analysis revealed the good mechanical properties of the rGO/MnO₂ paper with a tensile strength of about 8.79 MPa and a Young's modulus of 9.84 GPa. The electrical conductivities were found to be $565 \pm 26 \text{ S m}^{-1}$ for rGO paper and $532 \pm 137 \text{ S m}^{-1}$ for rGO/MnO₂ paper with 20 wt% MnO₂ nanoparticles, respectively. The 3D interconnected porous structure, good mechanical properties and high conductivity endowed the as-prepared hybrid papers promising electrode materials for flexible supercapacitor. In the ASC device, the paper materials were directly connected to a metal clip as working electrode without any metallic current collectors. Areal capacitance of 897 mF cm^{-2} (243 F g^{-1}) at 50 mA g^{-1} was achieved from the rGO/MnO₂ paper electrode which is nearly four folds of the rGO paper electrode with 234 mF cm^{-2} (67 F g^{-1}). The areal capacitance of a bent asymmetric device with active mass of 15 mg reached 113 mF cm^{-2} (0.34 F) at 10 mA g^{-1} and it could power 8 LED decorating light bulbs for at least 25 s. The asymmetric supercapacitor device also showed

excellent cyclic stability with no significant difference in the bent and flat states and after 3600 cycles in bent state.

Choi et al.³⁴⁸ built a type of ASC with an embossed chemically modified graphene (e-CMG) film as negative electrode and MnO₂ coated e-CMG (MnO₂/e-CMG) as positive electrode. The MnO₂/e-CMG electrode was fabricated by a replicating and embossing technique with polystyrene colloidal particles as a sacrificial template. The resulting flexible e-CMG films showed a 3D interconnected macroporous structure which offered large ion-accessible surface area, facilitated rapid ionic transport in the whole electrode, and preserved high electronic conductivity (1204 S m⁻¹). In the MnO₂/e-CMG hybrid, MnO₂ was uniformly deposited on the e-CMG film via in situ redox reaction between NaMnO₄ and e-CMG film. Attributed to the novel structure, e-CMG and MnO₂/e-CMG films showed better performances compared to their counterparts (CMG film and MnO₂/CMG film) prepared via a template-free approach. The specific surface areas of the e-CMG and MnO₂/e-CMG films reached 194.20 and 142.01 m² g⁻¹, respectively, which are more than ten folds those of their corresponding template-free samples (18.52 m² g⁻¹ for CMG film and 13.59 m² g⁻¹ for MnO₂/CMG film). The specific capacitances of CMG film, e-CMG film, MnO₂/CMG film and MnO₂/e-CMG film were measured to be 93, 202, 137 and 389 F g⁻¹, respectively. As shown in Fig. 17, the ASC assembled with e-CMG film and MnO₂/e-CMG film exhibited high stability when tested in a wide voltage window of 2.0 V in 1 M Na₂SO₄ electrolyte. The maximum energy density and power density are 44 Wh kg⁻¹ and 25 kW kg⁻¹, respectively. Moreover, the as-assembled ASC also showed good cyclic stability with a high capacitance retention rate of 95% after 1000 cycles at 1 A g⁻¹.

In another report, Zhang et al. developed a flexible all-solid-state ASC with an electrochemically reduced GO (ERGO) and CNT hybrid (CNT-ERGO) foam as negative electrode and MnO₂/ERGO foam as positive electrode.⁴⁰ The CNT-ERGO foam was prepared by electrochemical reduction of CNT-GO foam.

The MnO₂/ERGO foam was synthesized by simultaneous electrodeposition of MnO₂ nanowires and electrochemical reduction of GO in 0.1 M Mn(OAc)₂ solution in the potential range of -1.5 to 1.4 V (vs. SCE). The C_s of MnO₂-ERGO foam, CNT-ERGO foam and ERGO foam electrodes were measured to be 422.5, 280.4 and 156.9 F g⁻¹ at 1 A g⁻¹ in 1.0 M Na₂SO₄ electrolyte, respectively. The C_s of the as-built all-solid-state ASC reached 69.4 F g⁻¹ with potassium polyacrylate/KCl gel electrolyte. The all-solid-state ASC could be cycled reversibly in a wide voltage region of 0 to 1.8 V with a maximum energy density of 31.8 Wh kg⁻¹, the highest power density of 9188.1 W kg⁻¹ and a capacitance retention rate of 84.4% after 10000 cycles.

Recently, Liu et al. designed a flexible and lightweight ASC using MnO₂/CNT/GE foam as the positive electrode and PPy/CNT/GE foam as the negative electrode.³⁹ The 3D flexible CNT/GE foam was prepared via a two-step CVD process with CH₄ and C₂H₄ as carbon source, respectively. The as-prepared CNT/GE foam displayed hierarchical porous structure, good flexibility, large surface area and high conductivity, which renders it an ideal substrate for preparation of hybrid materials (Fig. 18A-C). MnO₂ and PPy were deposited on the CNT/GE foam by a hydrothermal procedure and an in situ polymerization process, respectively. The as-built ASC could be tested in a wide voltage window of 1.6 V in 0.5 M Na₂SO₄ electrolyte, as shown in Fig. 18D-F. The ASC showed a high energy density of 22.2 Wh kg⁻¹, large power density of 10.3 kW kg⁻¹ and robust cyclic stability with 90.2% of the capacitance reserved even after 10000 cycles.

Chen et al. developed a configuration of ASC with Ni-Co-S nanosheet arrays supported on carbon fiber cloth as positive electrode and a hydrothermal-reduced porous rGO film as negative electrode.⁹⁴ The Ni-Co-S nanosheet arrays were electrodeposited on the surface of carbon fiber cloth and their structure can be controlled by varying the concentrations of NiCl₂ in the electrodeposition solution. The maximum C_s of

the Ni-Co-S nanosheet arrays can reach 1418 F g^{-1} at 5 A g^{-1} and can retain 1285 F g^{-1} at 100 A g^{-1} . The C_s of rGO film reached 332 F g^{-1} at 4 A g^{-1} and retained 171 F g^{-1} at 100 A g^{-1} . The as-built ASC was tested in 1 M KOH electrolyte with a voltage window of 1.8 V . The cell capacitance was measured to be 133 F g^{-1} (263 mF cm^{-2}) at 2 A g^{-1} and retained 74 F g^{-1} (146 mF cm^{-2}) at 30 A g^{-1} . The ASC showed a high energy density of 60 Wh kg^{-1} , large power density of 28.8 kW kg^{-1} and robust cyclic stability with 63.2% of the capacitance reserved even after 50000 cycles.

5. Conclusions and perspective

As stated above, graphene-based materials (including graphene oxide and reduced graphene oxide) are versatile building blocks in assembling freestanding structures as binder-free electrode materials for supercapacitors. However, among the used synthesis methods, each approach has its pros and cons. CVD process can produce highly conductive graphene structures with low defects but is limited by its low outputs, relatively high cost and strong hydrophobic property of the products. Hydrothermal assembly is an effective way in preparing 3D porous graphene hydrogels. However, the products are limited by the size of reactor (Teflon-lined autoclave) and have to be dried via supercritical fluid-drying and freeze-drying techniques to reserve their porous structures. At the same time, various frameworks like papers, textiles, polymer foams and Ni foam can be used as low-cost substrates and templates to fabricate self-supported graphene hybrids. However, the introduction of these substrates will increase the weight and volume of the products. On the other hand, graphene films and papers show good flexibility but are confined in low scale production. Thus, there are still many challenges in large-scale and cost-efficient preparation of graphene-based and self-supported high performance electrode materials for supercapacitors. To further enhance the capacitance performance of graphene-based freestanding materials, the following aspects

should be taken into consideration and more work should be carried out to overcome the current drawbacks.

- (1) The restacking of graphene sheets should be reduced to a minimum to obtain a 3D structure with maximum specific surface area, proper interlayer spacing and 3D interconnected porosity. The suppression of restacking can result in a 3D porous structure with open pores which is favorable for the easy access and quick diffusion of electrolyte ions. Since only the ions-accessible surface has contribution to the overall capacitance, the 3D open network structures can yield the maximum theoretical surface area, thus leading to enhanced capacitive performance. Therefore, rational design of porous graphene structures with proper interlayer space is crucial in fabricating self-supporting graphene electrode materials with high performance. Introduction of other small-sized and conductive “spacers”, like CNT, CNF, is thought to be a valid approach for preparing 3D porous and conductive GE materials. On the other hand, in-plane nanoholes are also beneficial for the rapid diffusion of electrolyte. Considering the volumetric energy density, the interlayer space should be as small as possible. In short, GE materials with proper interlayer space below 2 nm and appropriate amount in-plane nanoholes are favorable for the fabrication of supercapacitors with high volumetric energy density.
- (2) The reduction process should be well controlled. Generally, most of the free-standing graphene architectures are derived from graphene oxide structures. Graphene oxide is electrically insulated and it has to be reduced to conductive reduced graphene oxide (rGO) for electrode application. However, excessive reduction often results in hydrophobic products with most of surface electrolyte-inaccessible. Therefore, there should be a balance between conductivity and hydrophilicity. Rational reduction process should be adopted while simultaneously keeping a minimum level of heteroatom groups present in rGO sheets. These heteroatom groups can then act as pillars, preventing the restacking of rGO sheets

and meanwhile contributing pseudocapacitance to the total capacitance. Among all the aforementioned reduction methods, thermal reduction without post-treatment is considered to be the simplest, greenest and the most efficient approach for practical application. In a thermal reduction process, annealing temperature should be carefully selected to balance the conductivity and hydrophilicity of the resulting rGO products. According to the related literatures, a moderate temperature between 200 and 600 °C is proper. Meanwhile, photothermal reduction is considered to be one of the most effective ways to fabricate flexible electronics and microelectronics.

- (3) Much work has to be done on the reduction of internal resistance of electrodes since internal resistance can greatly influence the rate performance and power density of the as-built supercapacitors. In this case, larger graphene sheets are preferred in assembly of free-standing structures than smaller sized graphene sheets. Larger sized sheet often has less grain boundaries, more uninterrupted surface and reduced graphene junctions, which is essential for achieving both higher conductivity and better rate capacitance performance. For graphene hybrids, in situ deposited composites often exhibit lower contact resistance and better rate performance compared to mechanical mixed blends.
- (4) Substrate-free self-standing graphene materials are more welcome than substrates-contained counterparts, since the introduction of additional substrates will increase the cost, add “dead weight” and limit the application of the resulting materials in some cases. Fortunately, substrate-free graphene materials can be fabricated by many approaches. Moreover, some of the substrate-free graphene materials even could be functioned as electrode materials and simultaneously current collector, which can simplify the preparation procedure of electrodes, decrease the cost, and minimize the size and weight of the final devices.
- (5) Great attention should be paid to the mechanical properties of GE materials for practical applications.

Generally, ascribing to the good flexibility and elasticity of polymers, GE/conducting polymer hybrids display better mechanical property than GE/transition metal compound composites. Attributed to the strong van der Waal forces between rGO sheets, GE films/papers/gels obtained from solution processes usually present better flexibility and mechanical strength than the GE materials prepared by CVD. However, many solution process methods are actually unsuitable for large scale production. The rise of wet spinning and electrospinning technologies bring the preparation of GE materials into a new era. Up to now, a lot of studies have been performed on the preparation of ultralong (hundred meters), flexible and conductive GE fibers with excellent mechanical strength through wet spinning process, and on the fabrication of wearable supercapacitor devices based on the prepared GE fibers. Meanwhile, electrospinning is another important technology for the preparation of 3D continuous micro/nano fibers. GE nanofiber mats/films/papers made by electrospinning are considered to possess superior mechanical strength and can be built into flexible and wearable electronics directly without the knitting process like GE fibers obtained from wet spinning process. However, there is still no report on the preparation and capacitance performance of pristine GE materials and their composites made by electrospinning. Some technical issues still need to be overcome. Nonetheless, wet spinning and electrospinning are deemed as two promising routes for the large-scale production of GE materials for commercial application.

Overall, free-standing graphene-based materials are promising electrode materials for supercapacitors. The key issues in the fabrication of high performance graphene-based supercapacitor devices lie in the fully utilization of the prominent intrinsic properties of graphene, especially its extremely high surface area, strong mechanical strength and extraordinarily high conductivity, and the enhancements in the synergistic effect between graphene substrates and the supported active components. With the rapid advances in material engineering and technology, especially the progress in laser writing graphene devices, wet

spinning and electrospinning graphene fiber technology, inkjet and screen printing technology, it is foreseeable that the binder-free, flexible, portable and wearable graphene-based supercapacitor devices will experience rapid development in recent years.

Acknowledgements

This work was supported by the National Natural Science Foundation of China (No. 21275136) and the Natural Science Foundation of Jilin province, China (No. 201215090).

References

1. M. Winter and R. J. Brodd, *Chem. Rev.*, 2005, 105, 1021-1021.
2. S. W. Lee, B. M. Gallant, H. R. Byon, P. T. Hammond and Y. Shao-Horn, *Energy Environ. Sci.*, 2011, 4, 1972-1985.
3. P. J. Hall, M. Mirzaeian, S. I. Fletcher, F. B. Sillars, A. J. R. Rennie, G. O. Shitta-Bey, G. Wilson, A. Cruden and R. Carter, *Energy Environ. Sci.*, 2010, 3, 1238-1251.
4. P. Sharma and T. S. Bhatti, *Energy Convers. Manage.*, 2010, 51, 2901-2912.
5. P. Simon and Y. Gogotsi, *Nat. Mater.*, 2008, 7, 845-854.
6. G. Wang, L. Zhang and J. Zhang, *Chem. Soc. Rev.*, 2012, 41, 797-828.
7. A. G. Pandolfo and A. F. Hollenkamp, *J. Power Sources*, 2006, 157, 11-27.
8. T. Chen and L. M. Dai, *Mater. Today*, 2013, 16, 272-280.
9. Y. W. Zhu, S. Murali, M. D. Stoller, K. J. Ganesh, W. W. Cai, P. J. Ferreira, A. Pirkle, R. M. Wallace, K. A. Cychosz, M. Thommes, D. Su, E. A. Stach and R. S. Ruoff, *Science*, 2011, 332, 1537-1541.
10. M. Sevilla and R. Mokaya, *Energy Environ. Sci.*, 2014, 7, 1250-1280.

11. H. Li, J. Wang, Q. Chu, Z. Wang, F. Zhang and S. Wang, *J. Power Sources*, 2009, 190, 578-586.
12. G. Zhu, Z. He, J. Chen, J. Zhao, X. Feng, Y. Ma, Q. Fan, L. Wang and W. Huang, *Nanoscale*, 2014, 6, 1079-1085.
13. W. Liu, C. Lu, X. Wang, K. Liang and B. K. Tay, *J. Mater. Chem. A*, 2014, DOI: 10.1039/C4TA04023F.
14. X. Dong, H. Xu, X. Wang, Y. Huang, M. B. Chan-Park, H. Zhang, L. Wang, W. Huang and P. Chen, *ACS Nano*, 2012, 6, 3206-3213.
15. V. H. Nguyen and J. J. Shim, *J. Power Sources*, 2015, 273, 110-117.
16. L. Q. Wang, X. C. Li, T. M. Guo, X. B. Yan and B. K. Tay, *Int. J. Hydrogen Energy*, 2014, 39, 7876-7884.
17. I. Shakir, Z. Ali, J. Bae, J. Park and D. J. Kang, *Nanoscale*, 2014, 6, 4125-4130.
18. M. Liu and J. Sun, *J. Mater. Chem. A*, 2014, 2, 12068-12074.
19. H. M. Zhang, X. Z. Yu, D. Guo, B. H. Qu, M. Zhang, Q. H. Li and T. H. Wang, *ACS Appl. Mater. Interfaces*, 2013, 5, 7335-7340.
20. Y. Z. Xie, Y. Liu, Y. D. Zhao, Y. H. Tsang, S. P. Lau, H. T. Huang and Y. Chai, *J. Mater. Chem. A*, 2014, 2, 9142-9149.
21. S. J. He, X. W. Hu, S. L. Chen, H. Hu, M. Hanif and H. Q. Hou, *J. Mater. Chem.*, 2012, 22, 5114-5120.
22. S. P. Zhou, H. M. Zhang, Q. Zhao, X. H. Wang, J. Li and F. S. Wang, *Carbon*, 2013, 52, 440-450.
23. M. Sawangphruk, M. Suksomboon, K. Kongsupornsak, J. Khuntilo, P. Srimuk, Y. Sanguansak, P. Klunbud, P. Suktha and P. Chiochan, *J. Mater. Chem. A*, 2013, 1, 9630-9636.
24. Z. Chen, D. S. Yu, W. Xiong, P. P. Liu, Y. Liu and L. M. Dai, *Langmuir*, 2014, 30, 3567-3571.
25. F. Liu, S. Wang, G. Han, R. Liu, Y. Chang and Y. Xiao, *J. Appl. Polym. Sci.*, 2014, 131.
26. X. T. Ding, Y. Zhao, C. G. Hu, Y. Hu, Z. L. Dong, N. Chen, Z. P. Zhang and L. T. Qu, *J. Mater. Chem. A*,

- 2014, 2, 12355-12360.
27. S. Lee, M. S. Cho, H. Lee, J. D. Nam and Y. Lee, *J. Mater. Chem.*, 2012, 22, 1899-1903.
28. Y. Q. Han, M. X. Shen, Y. Wu, J. J. Zhu, B. Ding, H. Tong and X. G. Zhang, *Synth. Met.*, 2013, 172, 21-27.
29. Jaidev and S. Ramaprabhu, *J. Mater. Chem.*, 2012, 22, 18775-18783.
30. S. Dhibar, P. Bhattacharya, D. Ghosh, G. Hatui and C. K. Das, *Ind. Eng. Chem. Res.*, 2014, 53, 13030-13045.
31. E. Raymundo-Pinero, V. Khomenko, E. Frackowiak and F. Beguin, *J. Electrochem. Soc.*, 2005, 152, A229-A235.
32. C. C. Hu, K. H. Chang, M. C. Lin and Y. T. Wu, *Nano Lett.*, 2006, 6, 2690-2695.
33. X. W. Yang, C. Cheng, Y. F. Wang, L. Qiu and D. Li, *Science*, 2013, 341, 534-537.
34. F. X. Wang, S. Y. Xiao, Y. Y. Hou, C. L. Hu, L. L. Liu and Y. P. Wu, *RSC Adv.*, 2013, 3, 13059-13084.
35. V. Khomenko, E. Raymundo-Piñero and F. Béguin, *J. Power Sources*, 2006, 153, 183-190.
36. Q. T. Qu, P. Zhang, B. Wang, Y. H. Chen, S. Tian, Y. P. Wu and R. Holze, *J. Phys. Chem. C*, 2009, 113, 14020-14027.
37. Y. Xu, Z. Lin, X. Zhong, X. Huang, N. O. Weiss, Y. Huang and X. Duan, *Nat Commun*, 2014, 5, 4554.
38. J. T. Zhang and X. S. Zhao, *ChemSusChem*, 2012, 5, 818-841.
39. J. Liu, L. Zhang, H. B. Wu, J. Lin, Z. Shen and X. W. Lou, *Energy Environ. Sci.*, 2014, 7, 3709-3717.
40. Z. Zhang, F. Xiao, L. Qian, J. Xiao, S. Wang and Y. Liu, *Adv. Energy Mater.*, 2014, 4.
41. D. Yu, K. Goh, Q. Zhang, L. Wei, H. Wang, W. Jiang and Y. Chen, *Adv. Mater.*, 2014, 26, 6790-6797.
42. S. Chabi, C. Peng, D. Hu and Y. Zhu, *Adv. Mater.*, 2013, 26, 2440-2445.
43. S. Han, D. Wu, S. Li, F. Zhang and X. Feng, *Adv. Mater.*, 2014, 26, 849-864.

44. D. Wu, F. Zhang, H. Liang and X. Feng, *Chem. Soc. Rev.*, 2012, 41, 6160-6177.
45. D. Wei and J. Kivioja, *Nanoscale*, 2013, 5, 10108-10126.
46. D. C. Wei and Y. Q. Liu, *Adv. Mater.*, 2010, 22, 3225-3241.
47. V. Singh, D. Joung, L. Zhai, S. Das, S. I. Khondaker and S. Seal, *Prog. Mater. Sci.*, 2011, 56, 1178-1271.
48. A. K. Geim, *Science*, 2009, 324, 1530-1534.
49. M. M. Liu, R. Z. Zhang and W. Chen, *Chem. Rev.*, 2014, 114, 5117-5160.
50. M. J. Allen, V. C. Tung and R. B. Kaner, *Chem. Rev.*, 2010, 110, 132-145.
51. K. S. Novoselov, V. I. Fal'ko, L. Colombo, P. R. Gellert, M. G. Schwab and K. Kim, *Nature*, 2012, 490, 192-200.
52. J. M. Tour, *Chem. Mater.*, 2014, 26, 163-171.
53. C. G. Zhang, Z. W. Peng, J. Lin, Y. Zhu, G. D. Ruan, C. C. Hwang, W. Lu, R. H. Hauge and J. M. Tour, *ACS Nano*, 2013, 7, 5151-5159.
54. Q. Y. Peng, Y. B. Li, X. D. He, X. C. Gui, Y. Y. Shang, C. H. Wang, C. Wang, W. Q. Zhao, S. Y. Du, E. Z. Shi, P. X. Li, D. H. Wu and A. Y. Cao, *Adv. Mater.*, 2014, 26, 3241-3247.
55. C. H. Wang, X. D. He, Y. Y. Shang, Q. Y. Peng, Y. Y. Qin, E. Z. Shi, Y. B. Yang, S. T. Wu, W. J. Xu, S. Y. Du, A. Y. Cao and Y. B. Li, *J. Mater. Chem. A*, 2014, 2, 14994-15000.
56. M. F. El-Kady, V. Strong, S. Dubin and R. B. Kaner, *Science*, 2012, 335, 1326-1330.
57. L. Wu, W. Li, P. Li, S. Liao, S. Qiu, M. Chen, Y. Guo, Q. Li, C. Zhu and L. Liu, *Small*, 2014, 10, 1421-1429.
58. S. Park and R. S. Ruoff, *Nat. Nanotechnol.*, 2010, 5, 309-309.
59. T. Morishita, A. J. Clancy and M. S. P. Shaffer, *J. Mater. Chem. A*, 2014, 2, 15022-15028.

60. J. K. Wassei and R. B. Kaner, *Acc. Chem. Res.*, 2013, 46, 2244-2253.
61. Y. Hernandez, V. Nicolosi, M. Lotya, F. M. Blighe, Z. Y. Sun, S. De, I. T. McGovern, B. Holland, M. Byrne, Y. K. Gun'ko, J. J. Boland, P. Niraj, G. Duesberg, S. Krishnamurthy, R. Goodhue, J. Hutchison, V. Scardaci, A. C. Ferrari and J. N. Coleman, *Nat.Nanotechnol*, 2008, 3, 563-568.
62. M. Z. Cai, D. Thorpe, D. H. Adamson and H. C. Schniepp, *J. Mater. Chem.*, 2012, 22, 24992-25002.
63. Y. Zhang, L. Y. Zhang and C. W. Zhou, *Acc. Chem. Res.*, 2013, 46, 2329-2339.
64. F. M. Koehler and W. J. Stark, *Acc. Chem. Res.*, 2013, 46, 2297-2306.
65. L. Chen, Y. Hernandez, X. L. Feng and K. Mullen, *Angew. Chem. Int. Ed.*, 2012, 51, 7640-7654.
66. C. Mattevi, H. Kim and M. Chhowalla, *J. Mater. Chem.*, 2011, 21, 3324-3334.
67. A. Dato, V. Radmilovic, Z. Lee, J. Phillips and M. Frenklach, *Nano Lett.*, 2008, 8, 2012-2016.
68. Z. Bo, Y. Yang, J. H. Chen, K. H. Yu, J. H. Yan and K. F. Cen, *Nanoscale*, 2013, 5, 5180-5204.
69. M. Segal, *Nat.Nanotechnol*, 2009, 4, 611-613.
70. C. Cheng and D. Li, *Adv. Mater.*, 2013, 25, 13-30.
71. O. C. Compton and S. T. Nguyen, *Small*, 2010, 6, 711-723.
72. V. C. Tung, M. J. Allen, Y. Yang and R. B. Kaner, *Nat.Nanotechnol*, 2009, 4, 25-29.
73. D. R. Dreyer, A. D. Todd and C. W. Bielawski, *Chem. Soc. Rev.*, 2014, 43, 5288-5301.
74. Y. W. Zhu, S. Murali, W. W. Cai, X. S. Li, J. W. Suk, J. R. Potts and R. S. Ruoff, *Adv. Mater.*, 2010, 22, 3906-3924.
75. R. S. Edwards and K. S. Coleman, *Nanoscale*, 2013, 5, 38-51.
76. S. J. Guo and S. J. Dong, *Chem. Soc. Rev.*, 2011, 40, 2644-2672.
77. X. Huang, X. Y. Qi, F. Boey and H. Zhang, *Chem. Soc. Rev.*, 2012, 41, 666-686.
78. J. Zhu, D. Yang, Z. Yin, Q. Yan and H. Zhang, *Small*, 2014, 10, 3480-3498.

79. H. J. Choi, S. M. Jung, J. M. Seo, D. W. Chang, L. M. Dai and J. B. Baek, *Nano Energy*, 2012, 1, 534-551.
80. N. Mahmood, C. Z. Zhang, H. Yin and Y. L. Hou, *J. Mater. Chem. A*, 2014, 2, 15-32.
81. J. Chen, C. Li and G. Q. Shi, *J. Phys. Chem. Lett.*, 2013, 4, 1244-1253.
82. X. H. Cao, Z. Y. Yin and H. Zhang, *Energy Environ. Sci.*, 2014, 7, 1850-1865.
83. Y. Huang, J. J. Liang and Y. S. Chen, *Small*, 2012, 8, 1805-1834.
84. M. D. Stoller, S. J. Park, Y. W. Zhu, J. H. An and R. S. Ruoff, *Nano Lett.*, 2008, 8, 3498-3502.
85. J. L. Xia, F. Chen, J. H. Li and N. J. Tao, *Nat.Nanotechnol*, 2009, 4, 505-509.
86. U. N. Maiti, J. Lim, K. E. Lee, W. J. Lee and S. O. Kim, *Adv. Mater.*, 2014, 26, 615-619.
87. J. Zhang, F. Zhao, Z. P. Zhang, N. Chen and L. T. Qu, *Nanoscale*, 2013, 5, 3112-3126.
88. N. A. Kumar and J. B. Baek, *Chem. Commun.*, 2014, 50, 6298-6308.
89. Z. S. Wu, G. M. Zhou, L. C. Yin, W. Ren, F. Li and H. M. Cheng, *Nano Energy*, 2012, 1, 107-131.
90. S. He, C. Hu, H. Hou and W. Chen, *J. Power Sources*, 2014, 246, 754-761.
91. S. He and W. Chen, *J. Power Sources*, 2014, 262, 391-400.
92. S. J. He, L. L. Chen, C. C. Xie, H. Hu, S. L. Chen, M. Hanif and H. Q. Hou, *J. Power Sources*, 2013, 243, 880-886.
93. Y. Zhao, J. Liu, Y. Hu, H. H. Cheng, C. G. Hu, C. C. Jiang, L. Jiang, A. Y. Cao and L. T. Qu, *Adv. Mater.*, 2013, 25, 591-595.
94. W. Chen, C. Xia and H. N. Alshareef, *ACS Nano*, 2014, 8, 9531-9541.
95. D. S. Yu, K. Goh, H. Wang, L. Wei, W. C. Jiang, Q. Zhang, L. M. Dai and Y. Chen, *Nat.Nanotechnol*, 2014, 9, 555-562.
96. Z. P. Zhou and X. F. Wu, *J. Power Sources*, 2013, 222, 410-416.

97. Y. S. Moon, D. Kim, G. Lee, S. Y. Hong, K. K. Kim, S. M. Park and J. S. Ha, *Carbon*, 2015, 81, 29-37.
98. U. M. Patil, M. S. Nam, J. S. Sohn, S. B. Kulkarni, R. Shin, S. Kang, S. Lee, J. H. Kim and S. C. Jun, *J. Mater. Chem. A*, 2014, 2, 19075-19083.
99. X. Yu and H. S. Park, *Carbon*, 2014, 77, 59-65.
100. R. Sun, H. Chen, Q. Li, Q. Song and X. Zhang, *Nanoscale*, 2014, 6, 12912-12920.
101. Y. B. Tan and J. M. Lee, *J. Mater. Chem. A*, 2013, 1, 14814-14843.
102. L. L. Zhang, R. Zhou and X. S. Zhao, *J. Mater. Chem.*, 2010, 20, 5983-5992.
103. L. Dong, Z. X. Chen, D. Yang and H. B. Lu, *RSC Adv.*, 2013, 3, 21183-21191.
104. A. Ambrosi, C. K. Chua, A. Bonanni and M. Pumera, *Chem. Rev.*, 2014, 114, 7150-7188.
105. L. Huang, C. Li and G. Q. Shi, *J. Mater. Chem. A*, 2014, 2, 968-974.
106. Y. R. Li, K. X. Sheng, W. J. Yuan and G. Q. Shi, *Chem. Commun.*, 2013, 49, 291-293.
107. B. Mendoza-Sanchez, B. Rasche, V. Nicolosi and P. S. Grant, *Carbon*, 2013, 52, 337-346.
108. T. Chen, Y. H. Xue, A. K. Roy and L. M. Dai, *ACS Nano*, 2014, 8, 1039-1046.
109. G. F. Ren, X. Pan, S. Bayne and Z. Y. Fan, *Carbon*, 2014, 71, 94-101.
110. D. Li, M. B. Muller, S. Gilje, R. B. Kaner and G. G. Wallace, *Nat. Nanotechnol.*, 2008, 3, 101-105.
111. J. J. Shao, W. Lv and Q. H. Yang, *Adv. Mater.*, 2014, 26, 5586-5612.
112. S. H. Lee, D. H. Lee, W. J. Lee and S. O. Kim, *Adv. Funct. Mater.*, 2011, 21, 1338-1354.
113. T. Kuila, A. K. Mishra, P. Khanra, N. H. Kim and J. H. Lee, *Nanoscale*, 2013, 5, 52-71.
114. Y. L. Zhang, L. Guo, H. Xia, Q. D. Chen, J. Feng and H. B. Sun, *Adv. Optical Mater.*, 2014, 2, 10-28.
115. H. F. Huang, L. Q. Xu, Y. M. Tang, S. L. Tang and Y. W. Du, *Nanoscale*, 2014, 6, 2426-2433.
116. Y. S. Wang, S. M. Li, S. T. Hsiao, W. H. Liao, P. H. Chen, S. Y. Yang, H. W. Tien, C. C. M. Ma and C. C. Hu, *Carbon*, 2014, 73, 87-98.

117. S. Biswas and L. T. Drzal, *ACS Appl. Mater. Interfaces*, 2010, 2, 2293-2300.
118. S. H. Tamboli, B. S. Kim, G. Choi, H. Lee, D. Lee, U. M. Patil, J. Lim, S. B. Kulkarni, S. C. Jun and H. H. Cho, *J. Mater. Chem. A*, 2014, 2, 5077-5086.
119. K. Chen, F. Liu, S. Song and D. Xue, *CrystEngComm*, 2014, 16, 7771-7776.
120. F. Liu, S. Song, D. Xue and H. Zhang, *Adv. Mater.*, 2012, 24, 1089-1094.
121. Y. R. Kang, Y. L. Li, F. Hou, Y. Y. Wen and D. Su, *Nanoscale*, 2012, 4, 3248-3253.
122. S. D. Perera, R. G. Mariano, N. Nijem, Y. Chabal, J. P. Ferraris and K. J. Balkus, *J. Power Sources*, 2012, 215, 1-10.
123. Z. Bo, W. G. Zhu, X. Tu, Y. Yang, S. Mao, Y. He, J. H. Chen, J. H. Yan and K. F. Cen, *J. Phys. Chem. C*, 2014, 118, 13493-13502.
124. Z. W. Lei, T. Mitsui, H. Nakafuji, M. Itagaki and W. Sugimoto, *J. Phys. Chem. C*, 2014, 118, 6624-6630.
125. F. Xiang, J. Zhong, N. Y. Gu, R. Mukherjee, I. K. Oh, N. Koratkar and Z. Y. Yang, *Carbon*, 2014, 75, 201-208.
126. M. Beidaghi, Z. F. Wang, L. Gu and C. L. Wang, *J. Solid State Electrochem.*, 2012, 16, 3341-3348.
127. X. Z. Wu, J. Zhou, W. Xing, G. Q. Wang, H. Y. Cui, S. P. Zhuo, Q. Z. Xue, Z. F. Yan and S. Z. Qiao, *J. Mater. Chem.*, 2012, 22, 23186-23193.
128. Y. Q. Sun, Q. Wu and G. Q. Shi, *Phys. Chem. Chem. Phys.*, 2011, 13, 17249-17254.
129. L. Zhang and G. Q. Shi, *J. Phys. Chem. C*, 2011, 115, 17206-17212.
130. T. Q. Huang, B. N. Zheng, L. Kou, K. Gopalsamy, Z. Xu, C. Gao, Y. N. Meng and Z. X. Wei, *RSC Adv.*, 2013, 3, 23957-23962.
131. B. N. Zheng, T. Q. Huang, L. Kou, X. L. Zhao, K. Gopalsamy and C. Gao, *J. Mater. Chem. A*, 2014, 2,

- 9736-9743.
132. C. M. Chen, Q. Zhang, C. H. Huang, X. C. Zhao, B. S. Zhang, Q. Q. Kong, M. Z. Wang, Y. G. Yang, R. Cai and D. S. Su, *Chem. Commun.*, 2012, 48, 7149-7151.
133. Z. Weng, Y. Su, D.-W. Wang, F. Li, J. Du and H.-M. Cheng, *Adv. Energy Mater.*, 2011, 1, 917-922.
134. Z. X. Tai, X. B. Yan and Q. J. Xue, *J. Power Sources*, 2012, 213, 350-357.
135. W. Du, S. Qi, B. Zhou, P. Sun, L. Zhu and X. Jiang, *Electrochim. Acta*, 2014, 146, 353-358.
136. K. Z. Gao, Z. Q. Shao, J. Li, X. Wang, X. Q. Peng, W. J. Wang and F. J. Wang, *J. Mater. Chem. A*, 2013, 1, 63-67.
137. V. Chabot, D. Higgins, A. P. Yu, X. C. Xiao, Z. W. Chen and J. J. Zhang, *Energy Environ. Sci.*, 2014, 7, 1564-1596.
138. A. C. Pierre and G. M. Pajonk, *Chem. Rev.*, 2002, 102, 4243-4265.
139. S. Nardecchia, D. Carriazo, M. Luisa Ferrer, M. C. Gutierrez and F. del Monte, *Chem. Soc. Rev.*, 2013, 42, 794-830.
140. D. R. Dreyer, S. Park, C. W. Bielawski and R. S. Ruoff, *Chem. Soc. Rev.*, 2010, 39, 228-240.
141. S. F. Pei and H. M. Cheng, *Carbon*, 2012, 50, 3210-3228.
142. Q. Zhang, K. Scrafford, M. T. Li, Z. Y. Cao, Z. H. Xia, P. M. Ajayan and B. Q. Wei, *Nano Lett.*, 2014, 14, 1938-1943.
143. C. K. Chua and M. Pumera, *Chem. Soc. Rev.*, 2014, 43, 291-312.
144. J. Yang and L. D. Zou, *Electrochim. Acta*, 2014, 130, 791-799.
145. Z. Q. Niu, L. Zhang, L. Liu, B. W. Zhu, H. B. Dong and X. D. Chen, *Adv. Mater.*, 2013, 25, 4035-4042.
146. X. W. Yang, J. W. Zhu, L. Qiu and D. Li, *Adv. Mater.*, 2011, 23, 2833.
147. H. L. Guo, X. F. Wang, Q. Y. Qian, F. B. Wang and X. H. Xia, *ACS Nano*, 2009, 3, 2653-2659.

148. S. J. An, Y. W. Zhu, S. H. Lee, M. D. Stoller, T. Emilsson, S. Park, A. Velamakanni, J. H. An and R. S. Ruoff, *J. Phys. Chem. Lett.*, 2010, 1, 1259-1263.
149. X. J. Liu, X. Qi, Z. Zhang, L. Ren, G. L. Hao, Y. D. Liu, Y. Wang, K. Huang, X. L. Wei, J. Li, Z. Y. Huang and J. X. Zhong, *RSC Adv.*, 2014, 4, 13673-13679.
150. G. K. Ramesha and S. Sampath, *J. Phys. Chem. C*, 2009, 113, 7985-7989.
151. K. X. Sheng, Y. Q. Sun, C. Li, W. J. Yuan and G. Q. Shi, *Sci. Rep.*, 2012, 2, 247.
152. S. Y. Wang, B. Pei, X. S. Zhao and R. A. W. Dryfe, *Nano Energy*, 2013, 2, 530-536.
153. X. Han, M. R. Funk, F. Shen, Y. C. Chen, Y. Li, C. J. Campbell, J. Dai, X. Yang, J. W. Kim, Y. Liao, J. W. Connell, V. Barone, Z. Chen, Y. Lin and L. Hu, *ACS Nano*, 2014, 8, 8255-8265.
154. Z. Q. Niu, J. Chen, H. H. Hng, J. Ma and X. D. Chen, *Adv. Mater.*, 2012, 24, 4144-4150.
155. Y. Zhou, Q. L. Bao, B. Varghese, L. A. L. Tang, C. K. Tan, C. H. Sow and K. P. Loh, *Adv. Mater.*, 2010, 22, 67-71.
156. L. J. Cote, R. Cruz-Silva and J. X. Huang, *J. Am. Chem. Soc.*, 2009, 131, 11027-11032.
157. V. Strong, S. Dubin, M. F. El-Kady, A. Lech, Y. Wang, B. H. Weiller and R. B. Kaner, *ACS Nano*, 2012, 6, 1395-1403.
158. S. Gilje, S. Dubin, A. Badakhshan, J. Farrar, S. A. Danczyk and R. B. Kaner, *Adv. Mater.*, 2010, 22, 419.
159. V. A. Smirnov, A. A. Arbuzov, Y. M. Shul'ga, S. A. Baskakov, V. M. Martynenko, V. E. Muradyan and E. I. Kresova, *High Energ. Chem.*, 2011, 45, 57-61.
160. J. J. Liang, Y. S. Chen, Y. F. Xu, Z. B. Liu, L. Zhang, X. Zhao, X. L. Zhang, J. G. Tian, Y. Huang, Y. F. Ma and F. F. Li, *ACS Appl. Mater. Interfaces*, 2010, 2, 3310-3317.
161. W. Gao, N. Singh, L. Song, Z. Liu, A. L. M. Reddy, L. J. Ci, R. Vajtai, Q. Zhang, B. Q. Wei and P. M.

- Ajayan, *Nat.Nanotechnol.*, 2011, 6, 496-500.
162. M. F. El-Kady and R. B. Kaner, *Nat. Commun.*, 2013, 4, 1475.
163. Y. Chang, G. Han, D. Fu, F. Liu, M. Li and Y. Li, *J. Power Sources*, 2014, 252, 113-121.
164. P. Chen, J. J. Yang, S. S. Li, Z. Wang, T. Y. Xiao, Y. H. Qian and S. H. Yu, *Nano Energy*, 2013, 2, 249-256.
165. K. Gopalsamy, Z. Xu, B. N. Zheng, T. Q. Huang, L. Kou, X. L. Zhao and C. Gao, *Nanoscale*, 2014, 6, 8595-8600.
166. Y. Xu, K. Sheng, C. Li and G. Shi, *ACS Nano*, 2010, 4, 4324-4330.
167. J. Chen, K. X. Sheng, P. H. Luo, C. Li and G. Q. Shi, *Adv. Mater.*, 2012, 24, 4569-4573.
168. Y. X. Xu, Z. Y. Lin, X. Q. Huang, Y. Liu, Y. Huang and X. F. Duan, *ACS Nano*, 2013, 7, 4042-4049.
169. K. X. Sheng, Y. X. Xu, C. Li and G. Q. Shi, *New Carbon Mater.*, 2011, 26, 9-15.
170. J. L. Shi, W. C. Du, Y. X. Yin, Y. G. Guo and L. J. Wan, *J. Mater. Chem. A*, 2014, 2, 10830-10834.
171. Z. L. Dong, C. C. Jiang, H. H. Cheng, Y. Zhao, G. Q. Shi, L. Jiang and L. T. Qu, *Adv. Mater.*, 2012, 24, 1856-1861.
172. H. Cheng, C. Hu, Y. Zhao and L. Qu, *NPG Asia Mater*, 2014, 6, e113.
173. Y. N. Meng, Y. Zhao, C. G. Hu, H. H. Cheng, Y. Hu, Z. P. Zhang, G. Q. Shi and L. T. Qu, *Adv. Mater.*, 2013, 25, 2326-2331.
174. K. Erickson, R. Erni, Z. Lee, N. Alem, W. Gannett and A. Zettl, *Adv. Mater.*, 2010, 22, 4467-4472.
175. Z. Xu and C. Gao, *Nat. Commun.*, 2011, 2, 571.
176. C. S. Xiang, C. C. Young, X. Wang, Z. Yan, C. C. Hwang, G. Ceriotti, J. Lin, J. Kono, M. Pasquali and J. M. Tour, *Adv. Mater.*, 2013, 25, 4592-4597.
177. Y. Zhao, C. C. Jiang, C. G. Hu, Z. L. Dong, J. L. Xue, Y. N. Meng, N. Zheng, P. W. Chen and L. T. Qu,

- ACS Nano*, 2013, 7, 2406-2412.
178. Z. Xu and C. Gao, *Acc. Chem. Res.*, 2014, 47, 1267-1276.
179. R. Jalili, S. H. Aboutalebi, D. Esrafilzadeh, R. L. Shepherd, J. Chen, S. Aminorroaya-Yamini, K. Konstantinov, A. I. Minett, J. M. Razal and G. G. Wallace, *Adv. Funct. Mater.*, 2013, 23, 5345-5354.
180. H. P. Cong, X. C. Ren, P. Wang and S. H. Yu, *Sci. Rep.*, 2012, 2, 613.
181. Z. Xu, Y. Zhang, P. G. Li and C. Gao, *ACS Nano*, 2012, 6, 7103-7113.
182. J. K. Sun, Y. H. Li, Q. Y. Peng, S. C. Hou, D. C. Zou, Y. Y. Shang, Y. B. Li, P. X. Li, Q. J. Du, Z. H. Wang, Y. Z. Xia, L. H. Xia, X. L. Li and A. Y. Cao, *ACS Nano*, 2013, 7, 10225-10232.
183. S. H. Aboutalebi, R. Jalili, D. Esrafilzadeh, M. Salari, Z. Gholamvand, S. A. Yamini, K. Konstantinov, R. L. Shepherd, J. Chen, S. E. Moulton, P. C. Innis, A. I. Minett, J. M. Razal and G. G. Wallace, *ACS Nano*, 2014, 8, 2456-2466.
184. P. P. Yu, Y. Z. Li, X. Zhao, L. H. Wu and Q. H. Zhang, *Langmuir*, 2014, 30, 5306-5313.
185. J. Yan, Y. Ding, C. Hu, H. Cheng, N. Chen, Z. Feng, Z. Zhang and L. Qu, *J. Mater. Chem. A*, 2014, 2, 16786-16792.
186. S. B. Ye, J. C. Feng and P. Y. Wu, *ACS Appl. Mater. Interfaces*, 2013, 5, 7122-7129.
187. K. Z. Gao, Z. Q. Shao, X. Wu, X. Wang, Y. H. Zhang, W. J. Wang and F. J. Wang, *Nanoscale*, 2013, 5, 5307-5311.
188. Y. Gao, Y. S. Zhou, W. Xiong, L. J. Jiang, M. Mahjouri-samani, P. Thirugnanam, X. Huang, M. M. Wang, L. Jiang and Y. F. Lu, *APL Mater.*, 2013, 1, 012101.
189. J. J. Yoo, K. Balakrishnan, J. S. Huang, V. Meunier, B. G. Sumpter, A. Srivastava, M. Conway, A. L. M. Reddy, J. Yu, R. Vajtai and P. M. Ajayan, *Nano Lett.*, 2011, 11, 1423-1427.
190. J. Zhi, W. Zhao, X. Y. Liu, A. R. Chen, Z. Q. Liu and F. Q. Huang, *Adv. Funct. Mater.*, 2014, 24,

- 2013-2019.
191. W. Chen, Z. L. Fan, G. F. Zeng and Z. P. Lai, *J. Power Sources*, 2013, 225, 251-256.
192. Z. Bo, Z. H. Wen, H. Kim, G. H. Lu, K. H. Yu and J. H. Chen, *Carbon*, 2012, 50, 4379-4387.
193. Z. Bo, W. G. Zhu, W. Ma, Z. H. Wen, X. R. Shuai, J. H. Chen, J. H. Yan, Z. H. Wang, K. F. Cen and X. L. Feng, *Adv. Mater.*, 2013, 25, 5799-5806.
194. P. Xu, J. Kang, J. B. Choi, J. Suhr, J. Yu, F. Li, J. H. Byun, B. S. Kim and T. W. Chou, *ACS Nano*, 2014, 8, 9437-9445.
195. J. R. Miller, R. A. Outlaw and B. C. Holloway, *Science*, 2010, 329, 1637-1639.
196. M. Z. Cai, R. A. Outlaw, S. M. Butler and J. R. Miller, *Carbon*, 2012, 50, 5481-5488.
197. J. R. Miller, R. A. Outlaw and B. C. Holloway, *Electrochim. Acta*, 2011, 56, 10443-10449.
198. M. Z. Cai, R. A. Outlaw, R. A. Quinlan, D. Premathilake, S. M. Butler and J. R. Miller, *ACS Nano*, 2014, 8, 5873-5882.
199. D. H. Seo, Z. J. Han, S. Kumar and K. Ostrikov, *Adv. Energy Mater.*, 2013, 3, 1316-1323.
200. Y. Wang, J. Chen, J. Cao, Y. Liu, Y. Zhou, J. H. Ouyang and D. Jia, *J. Power Sources*, 2014, 271, 269-277.
201. J. Lin, C. G. Zhang, Z. Yan, Y. Zhu, Z. W. Peng, R. H. Hauge, D. Natelson and J. M. Tour, *Nano Lett.*, 2013, 13, 72-78.
202. Y. He, W. Chen, J. Zhou, X. Li, P. Tang, Z. Zhang, J. Fu and E. Xie, *ACS Appl. Mater. Interfaces*, 2013, 6, 210-218.
203. C. Li, C. Hu, Y. Zhao, L. Song, J. Zhang, R. Huang and L. Qu, *Carbon*, 2014, 78, 231-242.
204. Q. Chen, Y. Hu, C. G. Hu, H. H. Cheng, Z. P. Zhang, H. B. Shao and L. T. Qu, *Phys. Chem. Chem. Phys.*, 2014, 16, 19307-19313.

205. F. S. Wen, C. X. Hao, J. Y. Xiang, L. M. Wang, H. Hou, Z. B. Su, W. T. Hu and Z. Y. Liu, *Carbon*, 2014, 75, 236-243.
206. H. R. Byon, S. W. Lee, S. Chen, P. T. Hammond and Y. Shao-Horn, *Carbon*, 2011, 49, 457-467.
207. J. Yan, T. Wei, B. Shao, F. Q. Ma, Z. J. Fan, M. L. Zhang, C. Zheng, Y. C. Shang, W. Z. Qian and F. Wei, *Carbon*, 2010, 48, 1731-1737.
208. Z. Q. Niu, J. J. Du, X. B. Cao, Y. H. Sun, W. Y. Zhou, H. H. Hng, J. Ma, X. D. Chen and S. S. Xie, *Small*, 2012, 8, 3201-3208.
209. M. Wang, J. Oh, T. Ghosh, S. Hong, G. Nam, T. Hwang and J. D. Nam, *RSC Adv.*, 2014, 4, 3284-3292.
210. S. Y. Wang and R. A. W. Dryfe, *J. Mater. Chem. A*, 2013, 1, 5279-5283.
211. Z. D. Huang, B. A. Zhang, S. W. Oh, Q. B. Zheng, X. Y. Lin, N. Yousefi and J. K. Kim, *J. Mater. Chem.*, 2012, 22, 3591-3599.
212. B. You, J. Jiang and S. Fan, *ACS Appl. Mater. Interfaces*, 2014, 6, 15302-15308.
213. H. F. Ju, W. L. Song and L. Z. Fan, *J. Mater. Chem. A*, 2014, 2, 10895-10903.
214. W. Wang, S. R. Guo, I. Ruiz, M. Ozkan and C. S. Ozkan, *ECS Transactions*, 2013, 50, 37-44.
215. H. Cheng, Z. Dong, C. Hu, Y. Zhao, Y. Hu, L. Qu, N. Chen and L. Dai, *Nanoscale*, 2013, 5, 3428-3434.
216. N. Jha, P. Ramesh, E. Bekyarova, M. E. Itkis and R. C. Haddon, *Adv. Energy Mater.*, 2012, 2, 438-444.
217. Y. Yoon, K. Lee, S. Kwon, S. Seo, H. Yoo, S. Kim, Y. Shin, Y. Park, D. Kim, J. Y. Choi and H. Lee, *ACS Nano*, 2014, 8, 4580-4590.
218. L. Kou, T. Huang, B. Zheng, Y. Han, X. Zhao, K. Gopalsamy, H. Sun and C. Gao, *Nat Commun*, 2014, 5, 3754.
219. D. H. Seo, S. Yick, Z. J. Han, J. H. Fang and K. Ostrikov, *ChemSusChem*, 2014, 7, 2317-2324.
220. Z. Yan, L. L. Ma, Y. Zhu, I. Lahiri, M. G. Hahm, Z. Liu, S. B. Yang, C. S. Xiang, W. Lu, Z. W. Peng, Z.

- Z. Sun, C. Kittrell, J. Lou, W. B. Choi, P. M. Ajayan and J. M. Tour, *ACS Nano*, 2013, 7, 58-64.
221. W. Wang, S. R. Guo, M. Penchev, I. Ruiz, K. N. Bozhilov, D. Yan, M. Ozkan and C. S. Ozkan, *Nano Energy*, 2013, 2, 294-303.
222. L. Rodriguez-Perez, M. A. Herranz and N. Martin, *Chem. Commun.*, 2013, 49, 3721-3735.
223. Y. Zhao, C. G. Hu, Y. Hu, H. H. Cheng, G. Q. Shi and L. T. Qu, *Angew. Chem. Int. Ed.*, 2012, 51, 11371-11375.
224. L. M. Dai, *Acc. Chem. Res.*, 2013, 46, 31-42.
225. S. Ghosh, X. H. An, R. Shah, D. Rawat, B. Dave, S. Kar and S. Talapatra, *J. Phys. Chem. C*, 2012, 116, 20688-20693.
226. Z. Y. Lin, Y. Liu, Y. G. Yao, O. J. Hildreth, Z. Li, K. Moon and C. P. Wong, *J. Phys. Chem. C*, 2011, 115, 7120-7125.
227. H. T. Liu, Y. Q. Liu and D. B. Zhu, *J. Mater. Chem.*, 2011, 21, 3335-3345.
228. D. Chen, H. B. Feng and J. H. Li, *Chem. Rev.*, 2012, 112, 6027-6053.
229. A. Hirsch, J. M. Englert and F. Hauke, *Acc. Chem. Res.*, 2013, 46, 87-96.
230. H. B. Wang, M. S. Xie, L. Thia, A. Fisher and X. Wang, *J. Phys. Chem. Lett*, 2014, 5, 119-125.
231. C. L. Wang, Y. Zhou, L. Sun, Q. Zhao, X. Zhang, P. Wan and J. S. Qiu, *J. Phys. Chem. C*, 2013, 117, 14912-14919.
232. Z. S. Wu, K. Parvez, A. Winter, H. Vieker, X. J. Liu, S. Han, A. Turchanin, X. L. Feng and K. Mullen, *Adv. Mater.*, 2014, 26, 4552-4558.
233. C. N. R. Rao, K. Gopalakrishnan and A. Govindaraj, *Nano Today*, 2014, 9, 324-343.
234. J. Q. Liu, J. G. Tang and J. J. Gooding, *J. Mater. Chem.*, 2012, 22, 12435-12452.
235. W. Ai, W. W. Zhou, Z. Z. Du, Y. P. Du, H. Zhang, X. T. Jia, L. H. Xie, M. D. Yi, T. Yu and W. Huang, *J.*

- Mater. Chem.*, 2012, 22, 23439-23446.
236. C. Z. Zhu, J. F. Zhai and S. J. Dong, *Nanoscale*, 2014, 6, 10077-10083.
237. V. Georgakilas, M. Otyepka, A. B. Bourlinos, V. Chandra, N. Kim, K. C. Kemp, P. Hobza, R. Zboril and K. S. Kim, *Chem. Rev.*, 2012, 112, 6156-6214.
238. W. J. Lee, U. N. Maiti, J. M. Lee, J. Lim, T. H. Han and S. O. Kim, *Chem. Commun.*, 2014, 50, 6818-6830.
239. K. Fujisawa, R. Cruz-Silva, K. S. Yang, Y. A. Kim, T. Hayashi, M. Endo, M. Terrones and M. S. Dresselhaus, *J. Mater. Chem. A*, 2014, 2, 9532-9540.
240. H. L. Guo, P. Su, X. F. Kang and S. K. Ning, *J. Mater. Chem. A*, 2013, 1, 2248-2255.
241. Q. Wu, Y. Q. Sun, H. Bai and G. Q. Shi, *Phys. Chem. Chem. Phys.*, 2011, 13, 11193-11198.
242. X. Li, X. Zang, Z. Li, X. Li, P. Li, P. Sun, X. Lee, R. Zhang, Z. Huang, K. Wang, D. Wu, F. Kang and H. Zhu, *Adv. Funct. Mater.*, 2013, 23, 4862-4869.
243. S. G. Song, Y. H. Xue, L. F. Feng, H. Elbatal, P. S. Wang, C. N. Moorefield, G. R. Newkome and L. M. Dai, *Angew. Chem. Int. Ed.*, 2014, 53, 1415-1419.
244. Z. S. Wu, A. Winter, L. Chen, Y. Sun, A. Turchanin, X. L. Feng and K. Mullen, *Adv. Mater.*, 2012, 24, 5130-5135.
245. S. Y. Wang, E. Iyyamperumal, A. Roy, Y. H. Xue, D. S. Yu and L. M. Dai, *Angew. Chem. Int. Ed.*, 2011, 50, 11756-11760.
246. Z. S. Wu, W. C. Ren, L. Xu, F. Li and H. M. Cheng, *ACS Nano*, 2011, 5, 5463-5471.
247. Y. Xu, Z. Lin, X. Huang, Y. Wang, Y. Huang and X. Duan, *Adv. Mater.*, 2013, 25, 5779-5784.
248. G. A. Snook, P. Kao and A. S. Best, *J. Power Sources*, 2011, 196, 1-12.
249. D. Jacob, P. A. Mini, A. Balakrishnan, S. V. Nair and K. R. V. Subramanian, *Bull. Mater. Sci.*, 2014, 37,

- 61-69.
250. M. Kim, C. Lee and J. Jang, *Adv. Funct. Mater.*, 2014, 24, 2489-2499.
251. Q. Wu, Y. Xu, Z. Yao, A. Liu and G. Shi, *ACS Nano*, 2010, 4, 1963-1970.
252. J. F. Wen, Y. D. Jiang, Y. J. Yang and S. B. Li, *J Mater Sci: Mater Electron*, 2014, 25, 1063-1071.
253. Z. G. Yin and Q. D. Zheng, *Adv. Energy Mater.*, 2012, 2, 179-218.
254. D.-W. Wang, F. Li, J. Zhao, W. Ren, Z.-G. Chen, J. Tan, Z.-S. Wu, I. Gentle, G. Q. Lu and H.-M. Cheng, *ACS Nano*, 2009, 3, 1745-1752.
255. Y. Z. Long, M. M. Li, C. Z. Gu, M. X. Wan, J. L. Duvail, Z. W. Liu and Z. Y. Fan, *Prog. Polym. Sci.*, 2011, 36, 1415-1442.
256. K. Wang, H. P. Wu, Y. N. Meng and Z. X. Wei, *Small*, 2014, 10, 14-31.
257. J. A. Lee, M. K. Shin, S. H. Kim, S. J. Kim, G. M. Spinks, G. G. Wallace, R. Ovalle-Robles, M. D. Lima, M. E. Kozlov and R. H. Baughman, *ACS Nano*, 2012, 6, 327-334.
258. B. Anothumakkool, A. T. A. Torris, S. N. Bhange, M. V. Badiger and S. Kurungot, *Nanoscale*, 2014, 6, 5944-5952.
259. A. Razaq, L. Nyholm, M. Sjodin, M. Stromme and A. Mihranyan, *Adv. Energy Mater.*, 2012, 2, 445-454.
260. L. L. Liu, Z. Q. Niu, L. Zhang, W. Y. Zhou, X. D. Chen and S. S. Xie, *Adv. Mater.*, 2014, 26, 4855-4862.
261. M. Liu, Y. E. Miao, C. Zhang, W. W. Tjiu, Z. Yang, H. Peng and T. Liu, *Nanoscale*, 2013, 5, 7312-7320.
262. H. P. Cong, X. C. Ren, P. Wang and S. H. Yu, *Energy Environ. Sci.*, 2013, 6, 1185-1191.
263. C. Peng, D. Hu and G. Z. Chen, *Chem. Commun.*, 2011, 47, 4105-4107.

264. H. S. Fan, N. Zhao, H. Wang, J. Xu and F. Pan, *J. Mater. Chem. A*, 2014, 2, 12340-12347.
265. Y. N. Meng, K. Wang, Y. J. Zhang and Z. X. Wei, *Adv. Mater.*, 2013, 25, 6985-6990.
266. P. Yu, X. Zhao, Z. Huang, Y. Li and Q. Zhang, *J. Mater. Chem. A*, 2014, 2, 14413-14420.
267. Y. Wang, X. Yang, L. Qiu and D. Li, *Energy Environ. Sci.*, 2013, 6, 477-481.
268. J. Zhang, J. Wang, J. Yang, Y. Wang and M. B. Chan-Park, *ACS Sustainable Chem. Eng.*, 2014, 2, 2291-2296.
269. X. C. Dong, J. X. Wang, J. Wang, M. B. Chan-Park, X. G. Li, L. H. Wang, W. Huang and P. Chen, *Mater. Chem. Phys.*, 2012, 134, 576-580.
270. S. B. Kulkarni, U. M. Patil, I. Shackery, J. S. Sohn, S. Lee, B. Park and S. Jun, *J. Mater. Chem. A*, 2014, 2, 4989-4998.
271. S. Biswas and L. T. Drzal, *Chem. Mater.*, 2010, 22, 5667-5671.
272. A. Davies, P. Audette, B. Farrow, F. Hassan, Z. W. Chen, J. Y. Choi and A. P. Yu, *J. Phys. Chem. C*, 2011, 115, 17612-17620.
273. X. Wang, K. Z. Gao, Z. Q. Shao, X. Q. Peng, X. Wu and F. J. Wang, *J. Power Sources*, 2014, 249, 148-155.
274. J. T. Zhang, P. Chen, B. H. L. Oh and M. B. Chan-Park, *Nanoscale*, 2013, 5, 9860-9866.
275. S. S. Xu, H. X. Yang, K. X. Wang, B. Wang and Q. Xu, *Phys. Chem. Chem. Phys.*, 2014, 16, 7350-7357.
276. L. Y. Li, K. Q. Xia, L. Li, S. M. Shang, Q. Z. Guo and G. P. Yan, *J. Nanopart. Res.*, 2012, 14.
277. C. Y. Chu, J. T. Tsai and C. L. Sun, *Int. J. Hydrogen Energy*, 2012, 37, 13880-13886.
278. X. Peng, L. L. Peng, C. Z. Wu and Y. Xie, *Chem. Soc. Rev.*, 2014, 43, 3303-3323.
279. J. Jiang, Y. Y. Li, J. P. Liu, X. T. Huang, C. Z. Yuan and X. W. Lou, *Adv. Mater.*, 2012, 24, 5166-5180.

280. W. T. Deng, X. B. Ji, Q. Y. Chen and C. E. Banks, *RSC Adv.*, 2011, 1, 1171-1178.
281. S. Liu, S. H. Sun and X. Z. You, *Nanoscale*, 2014, 6, 2037-2045.
282. M. Pumera, Z. Sofer and A. Ambrosi, *J. Mater. Chem. A*, 2014, 2, 8981-8987.
283. C. Z. Yuan, H. B. Wu, Y. Xie and X. W. Lou, *Angew. Chem. Int. Ed.*, 2014, 53, 1488-1504.
284. V. Augustyn, P. Simon and B. Dunn, *Energy Environ. Sci.*, 2014, 7, 1597-1614.
285. S. Faraji and F. N. Ani, *J. Power Sources*, 2014, 263, 338-360.
286. M. J. Zhi, C. C. Xiang, J. T. Li, M. Li and N. Q. Wu, *Nanoscale*, 2013, 5, 72-88.
287. H. L. Wang and H. J. Dai, *Chem. Soc. Rev.*, 2013, 42, 3088-3113.
288. U. M. Patil, J. S. Sohn, S. B. Kulkarni, S. C. Lee, H. G. Park, K. V. Gurav, J. H. Kim and S. C. Jun, *ACS Appl. Mater. Interfaces*, 2014, 6, 2448-2456.
289. X. H. Xia, Y. Q. Zhang, D. L. Chao, C. Guan, Y. J. Zhang, L. Li, X. Ge, I. M. Bacho, J. P. Tu and H. J. Fan, *Nanoscale*, 2014, 6, 5008-5048.
290. D. P. Dubal and R. Holze, *Pure Appl. Chem.*, 2014, 86, 611-632.
291. C. Wu, Q. Shen, R. Mi, S. Deng, Y. Shu, H. Wang, J. Liu and H. Yan, *J. Mater. Chem. A*, 2014, 2, 15987-15994.
292. S. Chen, J. J. Duan, Y. H. Tang and S. Z. Qiao, *Chem. Eur. J.*, 2013, 19, 7118-7124.
293. X. H. Xia, J. P. Tu, Y. J. Mai, R. Chen, X. L. Wang, C. D. Gu and X. B. Zhao, *Chem. Eur. J.*, 2011, 17, 10898-10905.
294. C. Y. Foo, A. Sumboja, D. J. H. Tan, J. Wang and P. S. Lee, *Adv. Energy Mater.*, 2014, 4.
295. H. T. Zhang, X. Zhang, D. C. Zhang, X. Z. Sun, H. Lin, C. H. Wang and Y. W. Ma, *J. Phys. Chem. B*, 2013, 117, 1616-1627.
296. S. Patil, V. Patil, S. Sathaye and K. Patil, *RSC Adv.*, 2014, 4, 4094-4104.

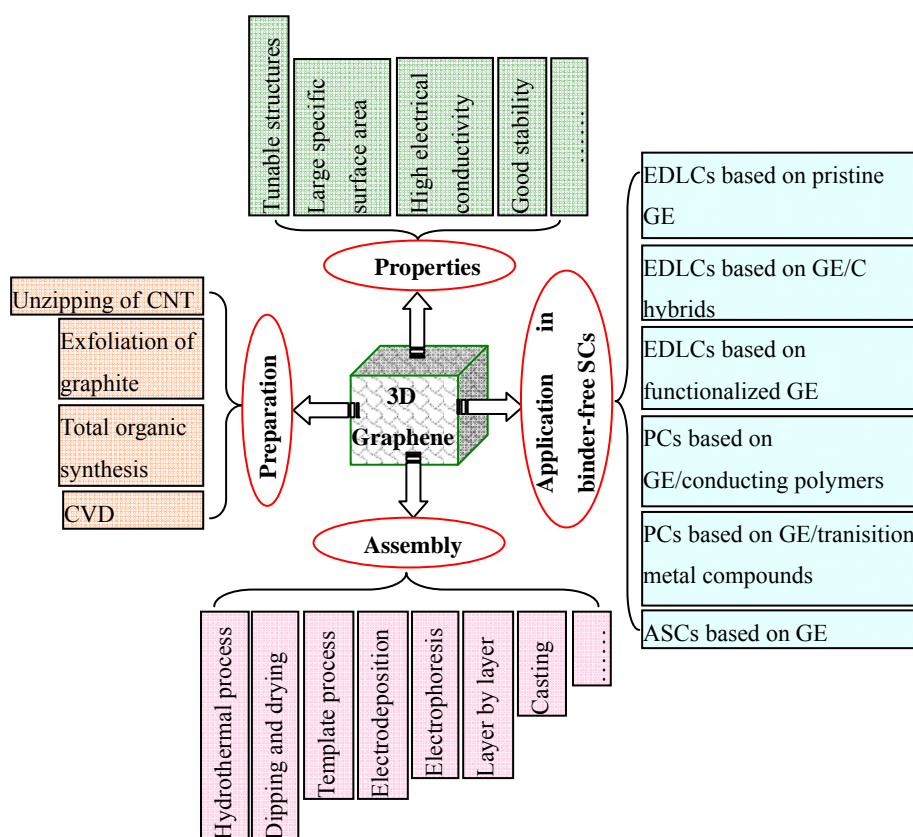
297. W. F. Wei, X. W. Cui, W. X. Chen and D. G. Ivey, *Chem. Soc. Rev.*, 2011, 40, 1697-1721.
298. S. J. He, C. X. Hu, H. Q. Hou and W. Chen, *J. Power Sources*, 2014, 246, 754-761.
299. M. B. Sassin, C. N. Chervin, D. R. Rolison and J. W. Long, *Acc. Chem. Res.*, 2013, 46, 1062-1074.
300. C. Gong, Y. He, J. Zhou, W. Chen, W. Han, Z. Zhang, P. Zhang, X. Pan, Z. Wang and E. Xie, *ACS Appl. Mater. Interfaces*, 2014, 6, 14844-14850.
301. J. H. Kim, S. Lee, J. W. Lee, T. Song and U. Paik, *Electrochim. Acta*, 2014, 125, 536-542.
302. X. L. Zhu, P. Zhang, S. Xu, X. B. Yan and Q. J. Xue, *ACS Appl. Mater. Interfaces*, 2014, 6, 11665-11674.
303. Z. P. Li, Y. J. Mi, X. H. Liu, S. Liu, S. R. Yang and J. Q. Wang, *J. Mater. Chem.*, 2011, 21, 14706-14711.
304. X. C. Dong, X. W. Wang, L. Wang, H. Song, X. G. Li, L. H. Wang, M. B. Chan-Park, C. M. Li and P. Chen, *Carbon*, 2012, 50, 4865-4870.
305. X. M. Li, T. S. Zhao, Q. Chen, P. X. Li, K. L. Wang, M. L. Zhong, J. Q. Wei, D. H. Wu, B. Q. Wei and H. W. Zhu, *Phys. Chem. Chem. Phys.*, 2013, 15, 17752-17757.
306. Q. Chen, Y. N. Meng, C. G. Hu, Y. Zhao, H. B. Shao, N. Chen and L. T. Qu, *J. Power Sources*, 2014, 247, 32-39.
307. T. Zhai, F. X. Wang, M. H. Yu, S. L. Xie, C. L. Liang, C. Li, F. M. Xiao, R. H. Tang, Q. X. Wu, X. H. Lu and Y. X. Tong, *Nanoscale*, 2013, 5, 6790-6796.
308. M. Kim, Y. Hwang and J. Kim, *Phys. Chem. Chem. Phys.*, 2014, 16, 351-361.
309. L. M. Li, E. H. Liu, J. Li, Y. J. Yang, H. J. Shen, Z. Z. Huang and X. X. Xiang, *ACTA PHYS-CHIM SIN*, 2010, 26, 1521-1526.
310. G. H. Yu, L. B. Hu, M. Vosgueritchian, H. L. Wang, X. Xie, J. R. McDonough, X. Cui, Y. Cui and Z. N.

- Bao, *Nano Lett.*, 2011, 11, 2905-2911.
311. V. L. Pushparaj, M. M. Shaijumon, A. Kumar, S. Murugesan, L. Ci, R. Vajtai, R. J. Linhardt, O. Nalamasu and P. M. Ajayan, *Proc. Natl. Acad. Sci. U. S. A.*, 2007, 104, 13574-13577.
312. P. Karthika, N. Rajalakshmi and K. S. Dhathathreyan, *ChemPhysChem*, 2013, 14, 3822-3826.
313. G. Y. Zheng, L. B. Hu, H. Wu, X. Xie and Y. Cui, *Energy Environ. Sci.*, 2011, 4, 3368-3373.
314. C. Z. Yuan, L. R. Hou, D. K. Li, L. F. Shen, F. Zhang and X. G. Zhang, *Electrochim. Acta*, 2011, 56, 6683-6687.
315. M. Pasta, F. La Mantia, L. B. Hu, H. D. Deshazer and Y. Cui, *Nano Res*, 2010, 3, 452-458.
316. G. H. Yu, L. B. Hu, N. A. Liu, H. L. Wang, M. Vosgueritchian, Y. Yang, Y. Cui and Z. A. Bao, *Nano Lett.*, 2011, 11, 4438-4442.
317. J. Ge, H. B. Yao, W. Hu, X. F. Yu, Y. X. Yan, L. B. Mao, H. H. Li, S. S. Li and S. H. Yu, *Nano Energy*, 2013, 2, 505-513.
318. Y. W. Cheng, S. T. Lu, H. B. Zhang, C. V. Varanasi and J. Liu, *Nano Lett.*, 2012, 12, 4206-4211.
319. Y. He, W. Chen, X. Li, Z. Zhang, J. Fu, C. Zhao and E. Xie, *ACS Nano*, 2012, 7, 174-182.
320. W. J. Chen, Y. M. He, X. D. Li, J. Y. Zhou, Z. X. Zhang, C. H. Zhao, C. S. Gong, S. K. Li, X. J. Pan and E. Q. Xie, *Nanoscale*, 2013, 5, 11733-11741.
321. Y. F. Zhang, M. Z. Ma, J. Yang, W. Huang and X. C. Dong, *RSC Adv.*, 2014, 4, 8466-8471.
322. W. Wang, S. R. Guo, K. N. Bozhilov, D. Yan, M. Ozkan and C. S. Ozkan, *Small*, 2013, 9, 3714-3721.
323. L. D. Feng, Y. F. Zhu, H. Y. Ding and C. Y. Ni, *J. Power Sources*, 2014, 267, 430-444.
324. Z. B. Wu, Y. R. Zhu and X. B. Ji, *J. Mater. Chem. A*, 2014, 2, 14759-14772.
325. Y. R. Zhu, X. B. Ji, Z. P. Wu, W. X. Song, H. S. Hou, Z. B. Wu, X. He, Q. Y. Chen and C. E. Banks, *J. Power Sources*, 2014, 267, 888-900.

326. C. M. Zhao, X. Wang, S. M. Wang, Y. Y. Wang, Y. X. Zhao and W. T. Zheng, *Int. J. Hydrogen Energy*, 2012, 37, 11846-11852.
327. U. M. Patil, S. C. Lee, J. S. Sohn, S. B. Kulkarni, K. V. Gurav, J. H. Kim, J. H. Kim, S. Lee and S. C. Jun, *Electrochim. Acta*, 2014, 129, 334-342.
328. Q. Zhang, C. Xu and B. Lu, *Electrochim. Acta*, 2014, 132, 180-185.
329. X. H. Cao, Y. M. Shi, W. H. Shi, G. Lu, X. Huang, Q. Y. Yan, Q. C. Zhang and H. Zhang, *Small*, 2011, 7, 3163-3168.
330. C. H. Jiang, B. B. Zhan, C. Li, W. Huang and X. C. Dong, *RSC Adv.*, 2014, 4, 18080-18085.
331. F. Du, D. S. Yu, L. M. Dai, S. Ganguli, V. Varshney and A. K. Roy, *Chem. Mater.*, 2011, 23, 4810-4816.
332. H. Zhang, A. J. Xie, C. P. Wang, H. S. Wang, Y. H. Shen and X. Y. Tian, *ChemPhysChem*, 2014, 15, 366-373.
333. C. Wang, J. Xu, M. F. Yuen, J. Zhang, Y. Li, X. Chen and W. Zhang, *Adv. Funct. Mater.*, 2014, 24, 6372-6380.
334. W. Wang, S. R. Guo, I. Lee, K. Ahmed, J. B. Zhong, Z. Favors, F. Zaera, M. Ozkan and C. S. Ozkan, *Sci. Rep.*, 2014, 4, 4452.
335. P. Y. Tang, Y. Q. Zhao, C. L. Xu and K. P. Ni, *J. Solid State Electrochem.*, 2013, 17, 1701-1710.
336. W. H. Khoh and J. D. Hong, *Colloids and Surfaces A: Physicochem. Eng. Aspects*, 2014, 456, 26-34.
337. Z. L. Wang, Z. L. Zhu, J. H. Qiu and S. H. Yang, *J. Mater. Chem. C*, 2014, 2, 1331-1336.
338. H. J. Liu and Y. Y. Xia, *Prog. Chem.*, 2011, 23, 595-604.
339. H. C. Gao, F. Xiao, C. B. Ching and H. W. Duan, *ACS Appl. Mater. Interfaces*, 2012, 4, 7019-7025.
340. Y. C. Qiu, Y. H. Zhao, X. W. Yang, W. F. Li, Z. H. Wei, J. W. Xiao, S. F. Leung, Q. F. Lin, H. K. Wu, Y. G. Zhang, Z. Y. Fan and S. H. Yang, *Nanoscale*, 2014, 6, 3626-3631.

341. Y. Jin, H. Y. Chen, M. H. Chen, N. Liu and Q. W. Li, *ACS Appl. Mater. Interfaces*, 2013, 5, 3408-3416.
342. Y. L. Shao, H. Z. Wang, Q. H. Zhang and Y. G. Li, *J. Mater. Chem. C*, 2013, 1, 1245-1251.
343. Y. W. Cheng, H. B. Zhang, S. T. Lu, C. V. Varanasiad and J. Liu, *Nanoscale*, 2013, 5, 1067-1073.
344. H. C. Gao, F. Xiao, C. B. Ching and H. W. Duan, *ACS Appl. Mater. Interfaces*, 2012, 4, 2801-2810.
345. S. D. Perera, M. Rudolph, R. G. Mariano, N. Nijem, J. P. Ferraris, Y. J. Chabal and K. J. Balkus, *Nano Energy*, 2013, 2, 966-975.
346. T. Zhai, S. Xie, M. Yu, P. Fang, C. Liang, X. Lu and Y. Tong, *Nano Energy*, 2014, 8, 255-263.
347. A. Sumboja, C. Y. Foo, X. Wang and P. S. Lee, *Adv. Mater.*, 2013, 25, 2809-2815.
348. B. G. Choi, M. Yang, W. H. Hong, J. W. Choi and Y. S. Huh, *ACS Nano*, 2012, 6, 4020-4028.

Figures and Tables



Scheme 1 Summary of 3D graphene-based nanomaterials: preparation, assembly, properties and applications in binder-free supercapacitors.

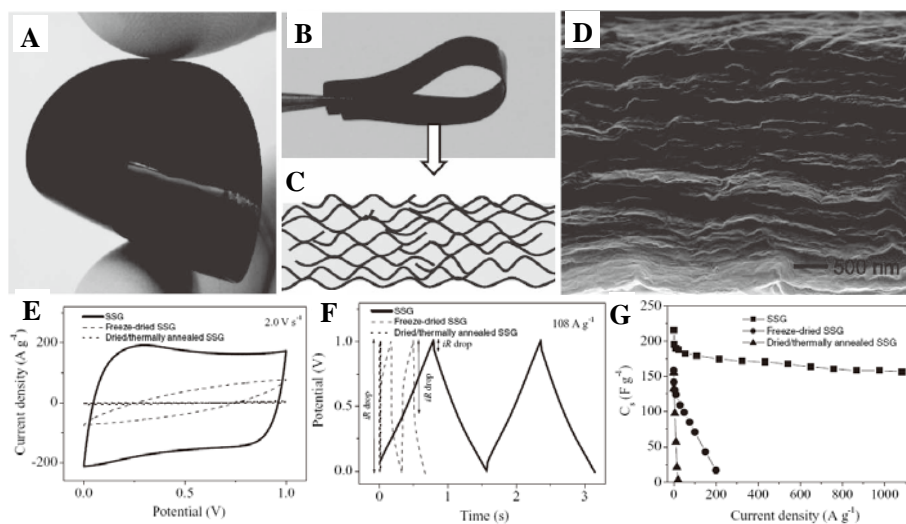


Fig. 1 (A, B) Photographs of the flexible solvated rGO films. (C) Schematic of the cross-section of the solvated rGO film. (D) SEM image showing the cross-section structure of a freeze-dried rGO film. (E) CV curves obtained at a scan rate of 2 V s⁻¹. (F) Charge/discharge plots obtained at the current densities of 108 A g⁻¹. (G) The plots of specific capacitance vs current density. (Reprinted with permission from ref. 146. Copyright 2011 Wiley-VCH)

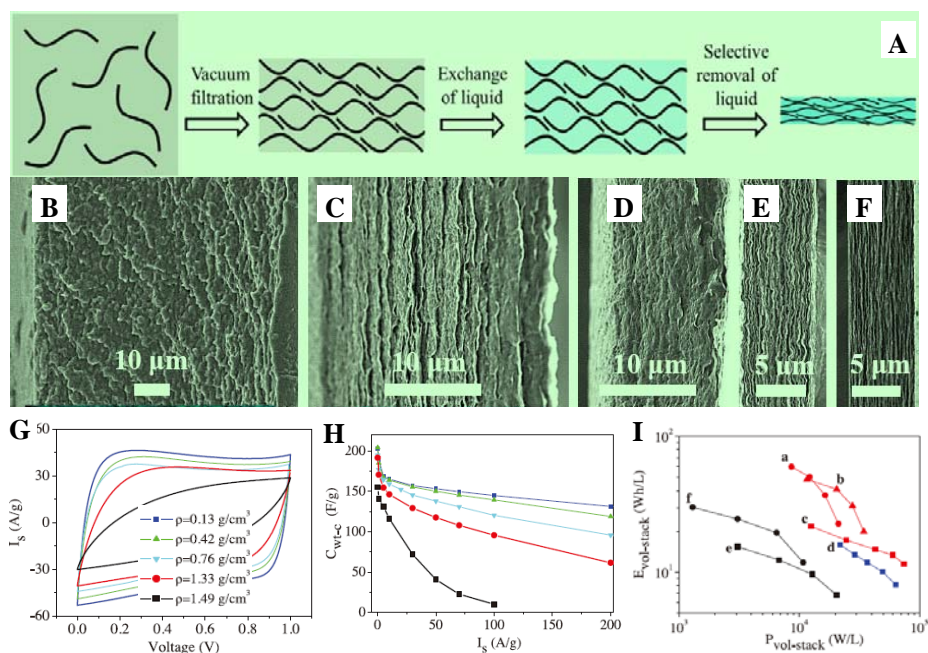


Fig. 2 (A) Schematic of the fabrication process of the EM-CCG film. SEM images of CCG/H₂SO₄ films (B-E) ($\rho=0.13, 0.42, 0.76$ and 1.33 g cm^{-3}) and dried CCG film (F) ($\rho=1.49 \text{ g cm}^{-3}$). (G) CV curves at 0.5 V s^{-1} . (H) Gravimetric specific capacitances with varied current densities. (I) Ragone plots of the EM-CCG films showing the relationships between $E_{\text{vol-stack}}$ and $P_{\text{vol-stack}}$ with the packing density and areal mass loading of CCG: (a) 1.25 g cm^{-3} , 10.0 mg cm^{-2} ; (b) 1.25 g cm^{-3} , 5.0 mg cm^{-2} ; (c) 1.25 g cm^{-3} , 1.0 mg cm^{-2} ; (d) 0.39 g cm^{-3} , 1.0 mg cm^{-2} ; the dried CCG films (1.49 g cm^{-3}) are also presented for comparison with the areal mass loading of (e) 1.0 mg cm^{-2} and (f) 5.0 mg cm^{-2} . The data were obtained from the prototype supercapacitors with EMIMBF₄/AN electrolyte and a working voltage of 3.5 V. (Reproduced with permission from ref. 33. Copyright 2013, the American Association for the Advancement of Science)

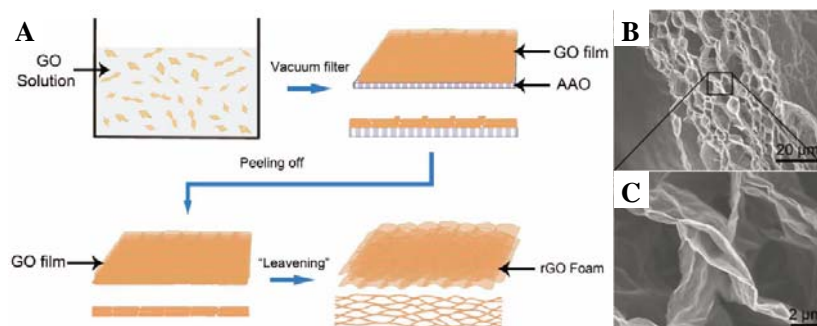


Fig. 3 (A) Schematic illustration of the leavening process for the preparation of rGO foams. (B, C) SEM images of cross-sectional view of rGO foams formed by leavening in an autoclave at 90 °C for 10 h with 80 μL hydrazine monohydrate. (Reprinted with permission from ref. 154. Copyright 2012 Wiley-VCH)

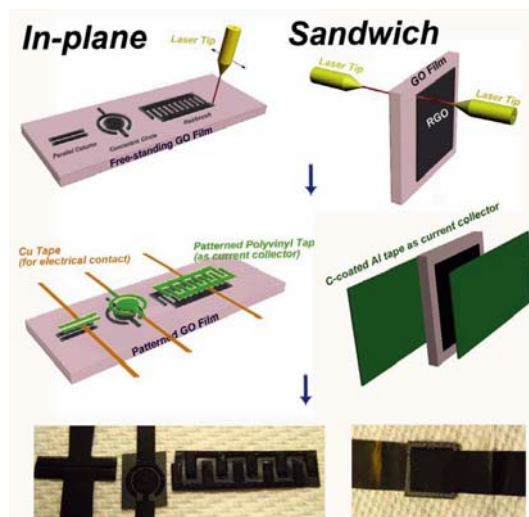


Fig. 4 Schematic drawings illustrating the detailed laser writing process for rGO-GO-rGO supercapacitor devices with in-plane and sandwich geometries. The black contrast in the top schematic stands for rGO and the light contrast to pristine hydrated GO. The bottom row presents the corresponding photographs of the final devices. (Reprinted with permission from ref. 161. Copyright 2011 Nature Publishing Group).

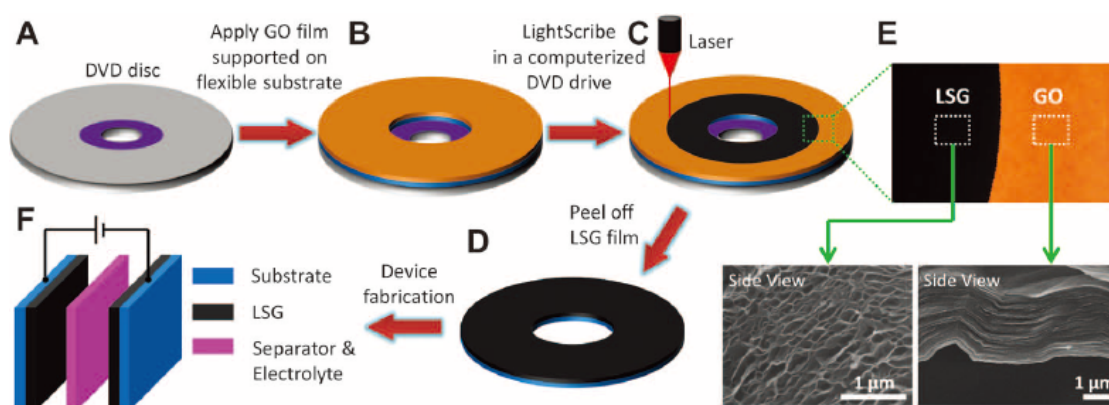


Fig. 5 Schematic diagram of the fabrication process of laser-scribed GE-based supercapacitors (A to D). The photograph shows the color change of golden brown GO film to black laser-scribed GE (E). The cross-sectional SEM images show the well-exfoliated few-layered LSG film by laser-scribing the stacked GO film. The configuration of a symmetric supercapacitor (F). (Reproduced with permission from ref. 56. Copyright 2012, the American Association for the Advancement of Science.)

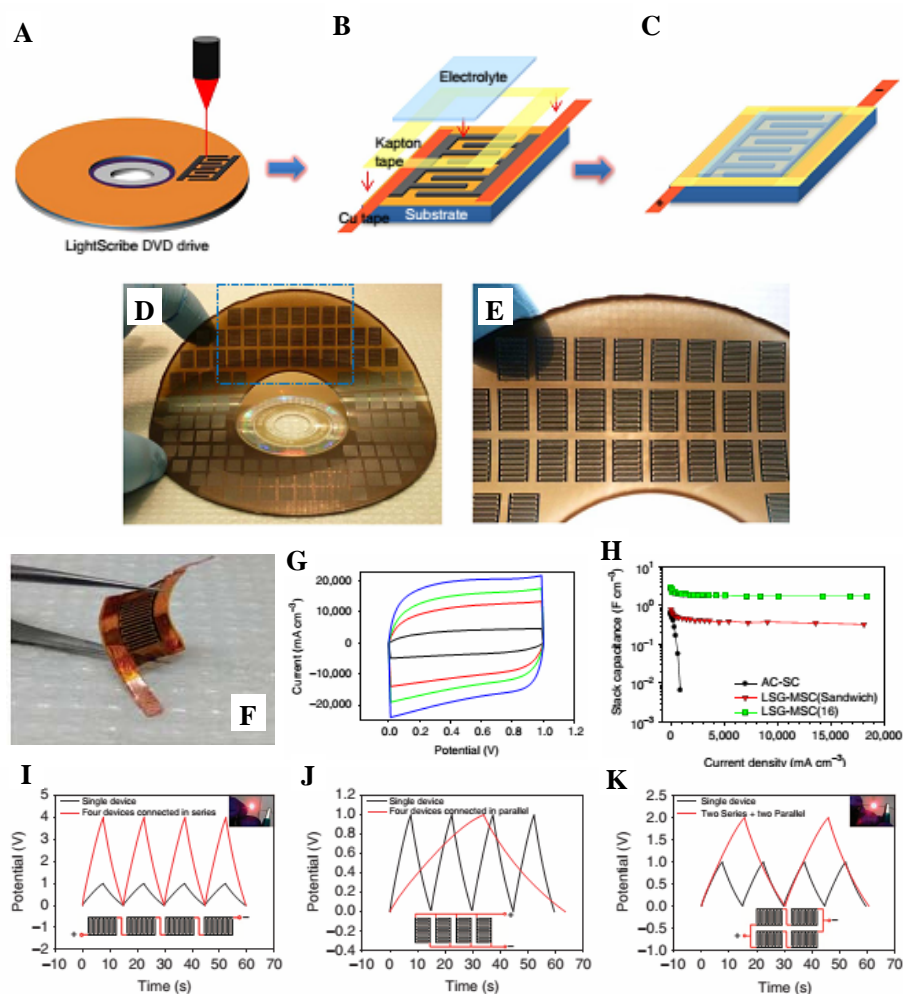


Fig. 6 (A–C) Schematic drawings illustrating the fabrication process of an LSG-MSC. (D–F) Micro-devices with high areal density prepared by the direct laser writing. (G–K) Capacitance performance of the LSG-MSC in the sandwich and interdigitated structures in PVA/H₂SO₄ gel electrolyte. (G) CV curves at a scan rate of 10 V s⁻¹ with 4, 8 and 16 electrodes. (H) Volumetric stack capacitance at different current densities. Galvanostatic charge/discharge curves for four tandem LSG-MSC connected in series (I), in parallel (J) and in a combination of series and parallel (K). A single device is shown for comparison. Insets show a shining light-emitting diode (LED) powered by the tandem micro-supercapacitor. (Reprinted with permission from ref. 162. Copyright 2013 Nature Publishing Group).

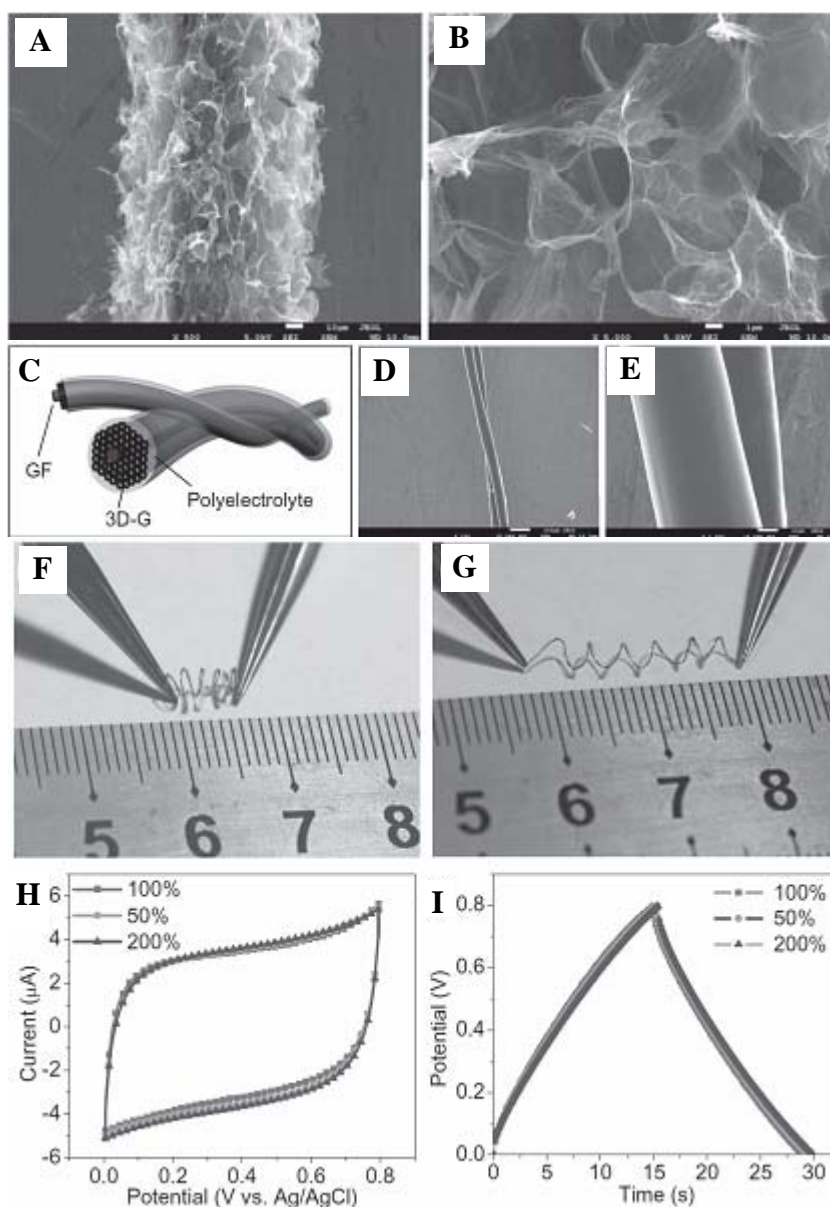


Fig. 7 (A, B) SEM images with different magnifications of a GF@3D-G. (C) Schematic drawings illustrating the fabrication of a wire-shaped supercapacitor from two twined GF@3D-Gs with PVA/H₃PO₄ gel polyelectrolyte. (D, E) SEM images of the twined and polyelectrolyte coated GF@3D-Gs under different magnifications. (F, G) The spring-like supercapacitor with a ca. 4.5 cm GF@3D-G at ca. 50% compressed and ca. 200% stretched status, respectively. The corresponding CVs at 50 mV s⁻¹ (H) and charge-discharge curves at the current of 4 μA (I) of the spring-like supercapacitor at free (100%), compressed (ca. 50%) and stretched (ca. 200%) status, respectively. (Reprinted with permission from ref. 173. Copyright 2013 Wiley-VCH)

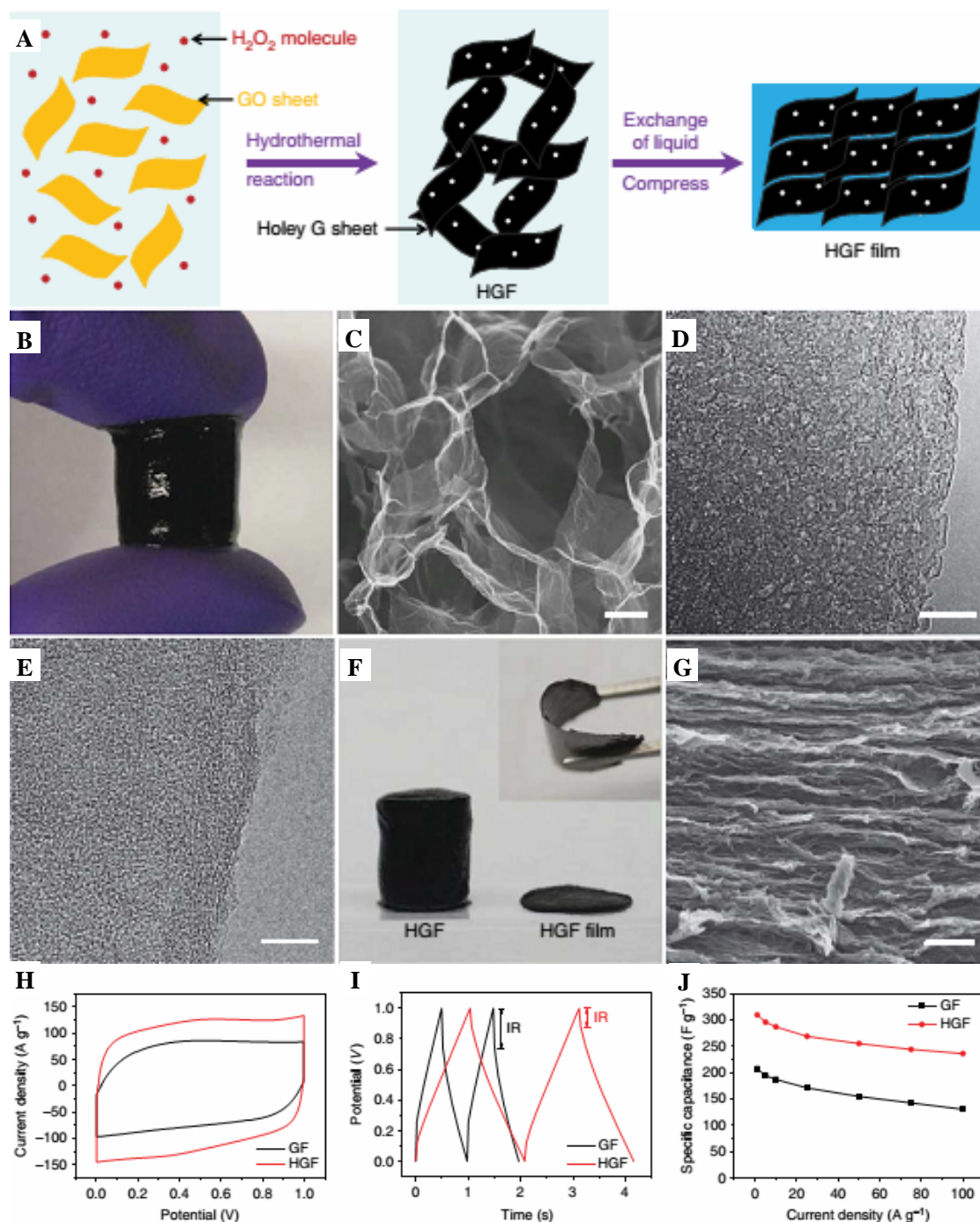


Fig. 8 (A) Schematic illustration of the fabrication of HGFs and HGF films. (B) A photograph displays the free-standing structure of a HGF. (C) SEM image of the interconnected porous structure of HGF (scale bar, 1 μm). (D) TEM image of the holey rGO sheets in HGF (scale bar, 10 nm). (E) TEM image of the non-hole rGO sheets in GF (scale bar, 10 nm). (F) A photograph shows a HGF before and after compression. The inset shows the flexibility of the compressed HGF film. (G) SEM image shows the cross-section of the compressed HGF film (scale bar, 1 μm). (H–J) Capacitance performance of the supercapacitors based on HGF and GF in 6 M KOH electrolyte. (H) CV curves at 1 V s^{-1} . (I) Galvanostatic charge/discharge curves at 100 A g^{-1} . (J) Comparison of C_s versus different current densities. (Reprinted with permission from ref. 37. Copyright 2014 Nature Publishing Group).

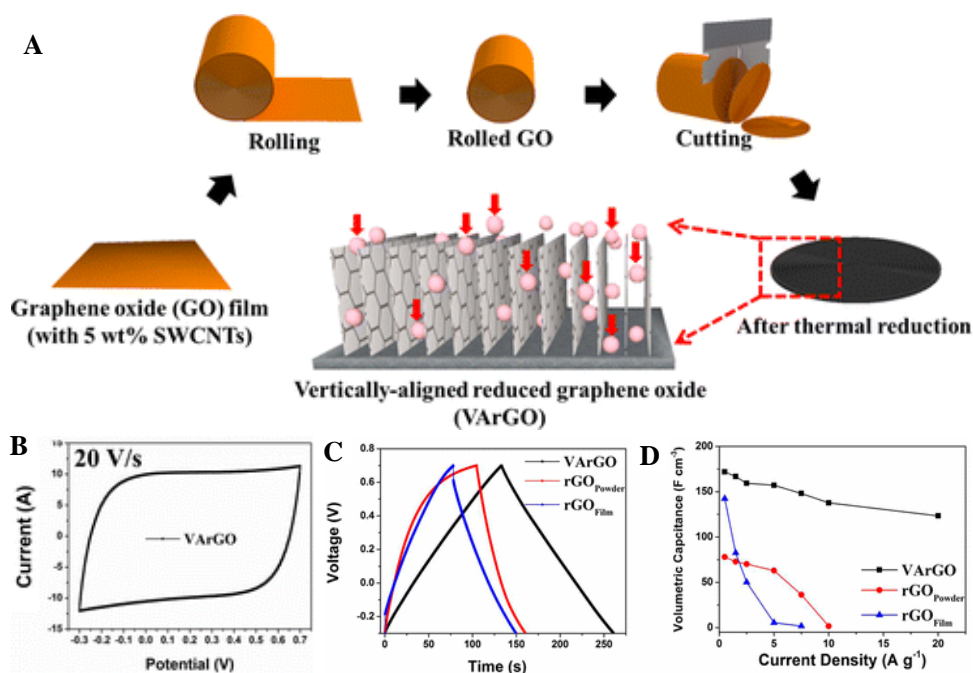


Fig. 9 (A) Schematic diagram of the fabrication of VArGO electrodes. (B) CV curves of VArGO electrode at an ultralarge scan rate of 20 V s⁻¹. (C) Galvanostatic charge/discharge curves of different rGO-based electrodes at 0.5 A g⁻¹. (D) Comparison of C_s versus different current densities on different rGO-based electrodes. (Reprinted with permission from ref. 217. Copyright 2014 American Chemical Society)

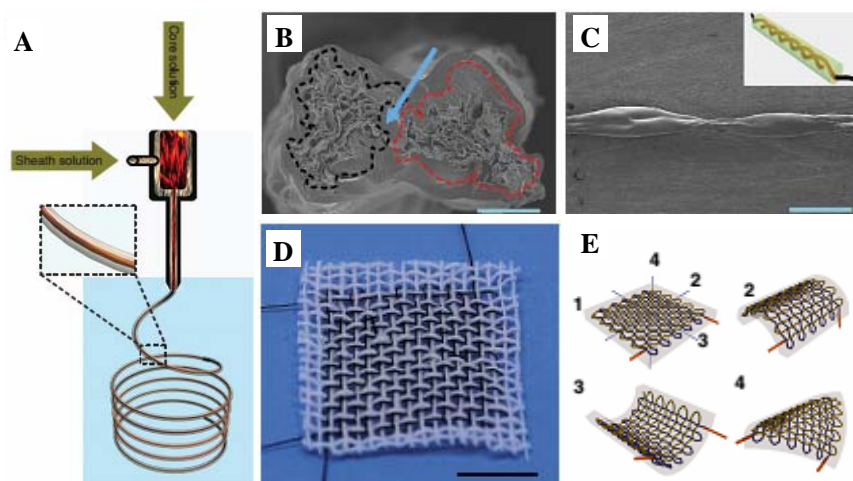


Fig. 10 (A) Schematic diagram of the coaxial spinning process for synthesizing GE+CNT hybrid fibers. (B) SEM images of cross-sectional and (C) side view of a two-ply YSC. The arrow area in (B) represents PVA/H₃PO₄ electrolyte and inset of (C) is the schematic of a YSC. (Scale bars, 50 µm in (B), 500 µm in (C)) (D) A cloth supercapacitor made by two intact coaxial fibers woven with cotton fibers. (E) Schematic illustration of a cloth supercapacitor in different status. (Reprinted with permission from ref. 218. Copyright 2014 Nature Publishing Group).

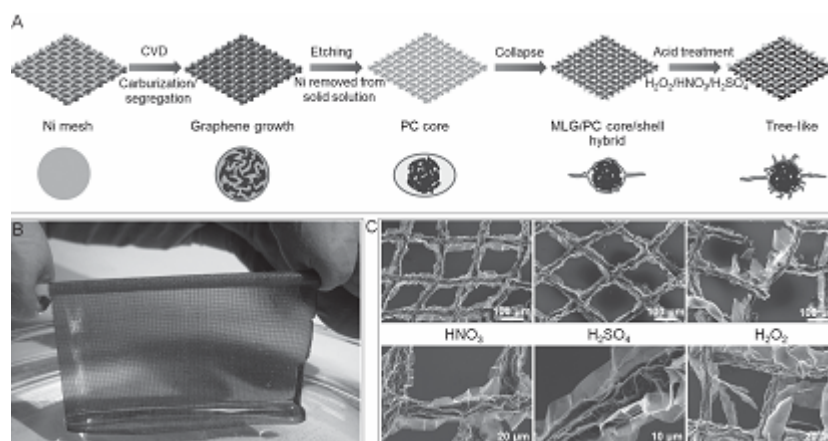


Fig. 11 (A) Schematic diagram illustrating the preparation of N-GE/PC film. Cross-sectional views of a core-shell structure are shown in the bottom plane, respectively. (B) Photograph of a 10-cm wide N-GE/PC film. (C) SEM images of N-GE/PC woven fabrics treated by acids. (Reprinted with permission from ref. 242. Copyright 2013 Wiley-VCH)

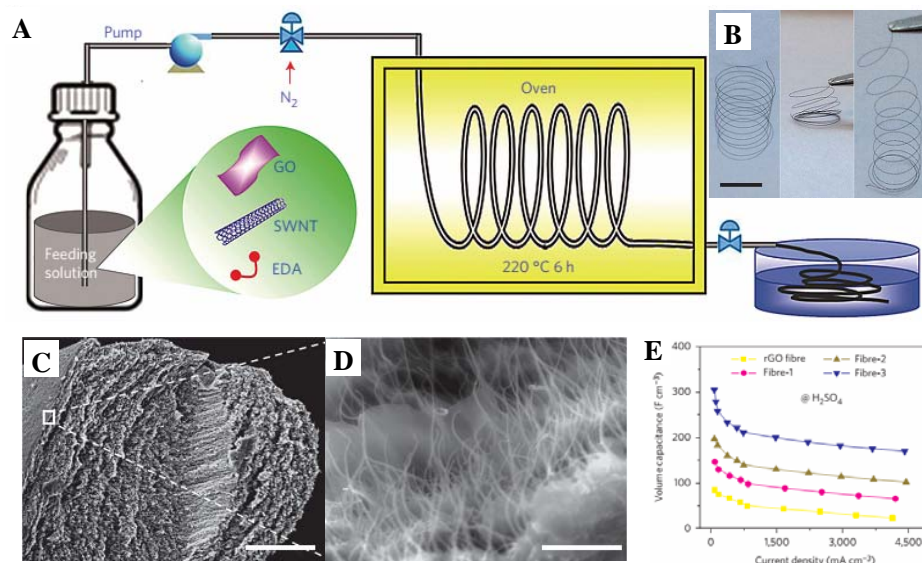


Fig. 12 (A) Schematic illustration of the synthesis process of carbon hybrid microfibres. (B) Photographs of fiber springs in different status. (C, D) Cross-sectional SEM images of the fibre-3 (scale bars: 15 μm in C, 300 nm in D). (E) Specific volumetric capacitance versus the current density of the as-prepared fiber supercapacitors in 1 M H₂SO₄ electrolyte. (Reprinted with permission from ref. 95. Copyright 2014 Nature Publishing Group).

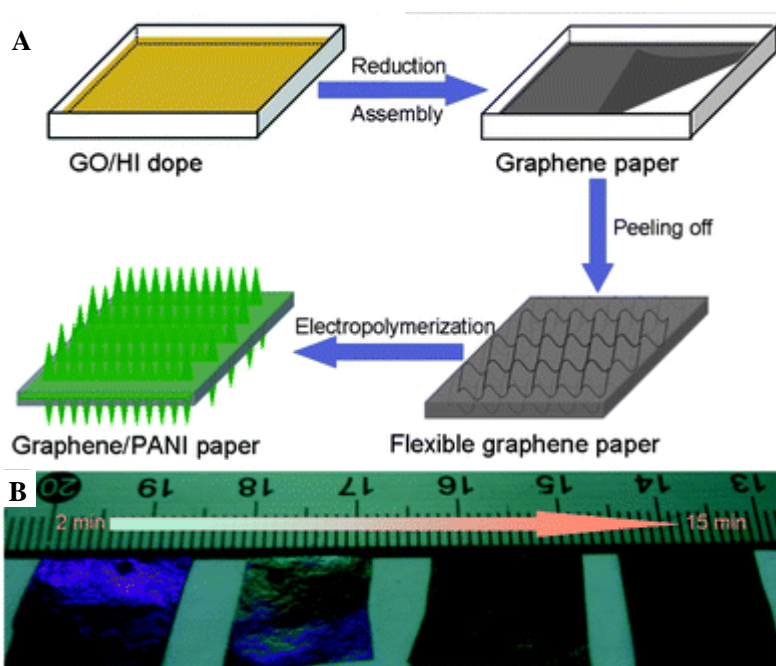


Fig. 13 (A) Schematic illustration of the preparation process of graphene/PANI paper. (B) Photograph of the graphene/PANI hybrid papers with electropolymerization times of 2, 5, 10, 15 min (from left to right). (Reprinted with permission from ref. 262. Copyright 2013 Royal Society of Chemistry)

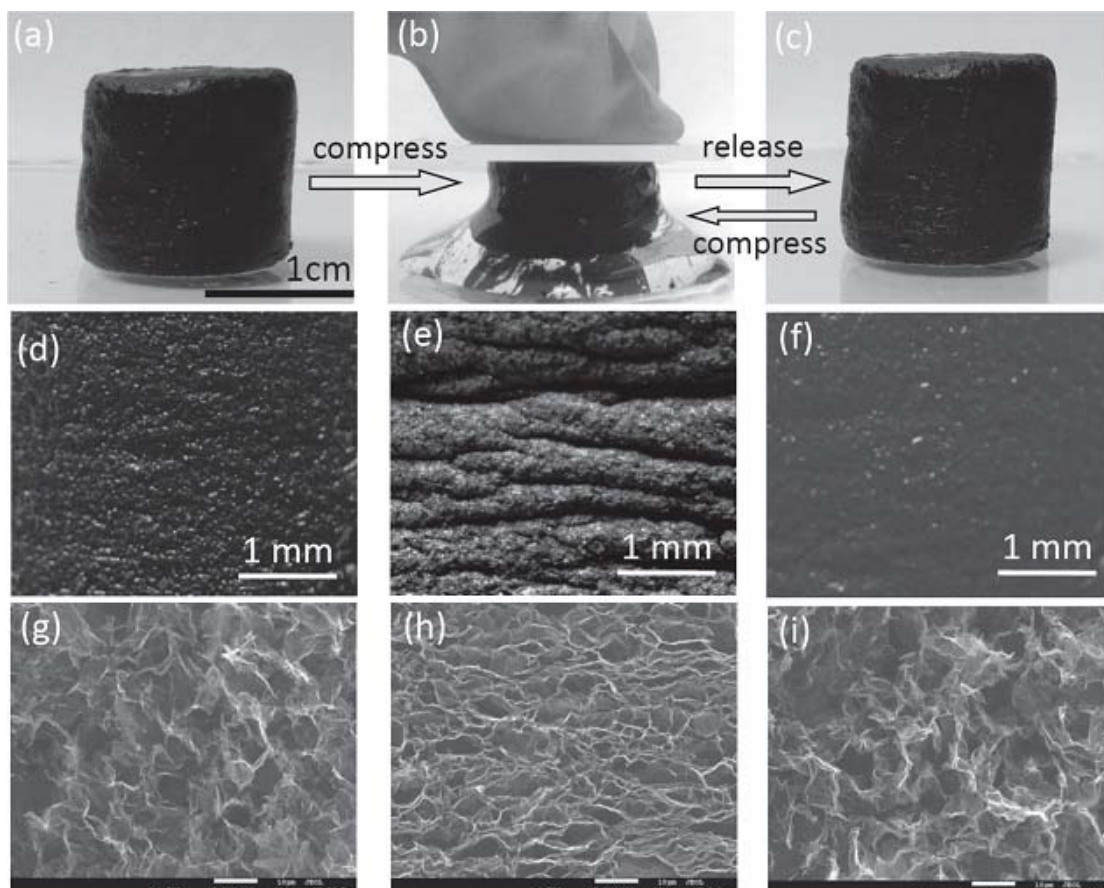


Fig. 14 (a-c) Photographs showing the compression-recovery processes of PPy/rGO foam. (d-f) Photographs of the surface views of PPy/rGO foam corresponding to status in (a-c), respectively. (g-i) Cross-sectional SEM images of the PPy/rGO foam, corresponding to the unloading-loading-unloading status in (a-c), respectively. (Reprinted with permission from ref. 93. Copyright 2012 Wiley-VCH)

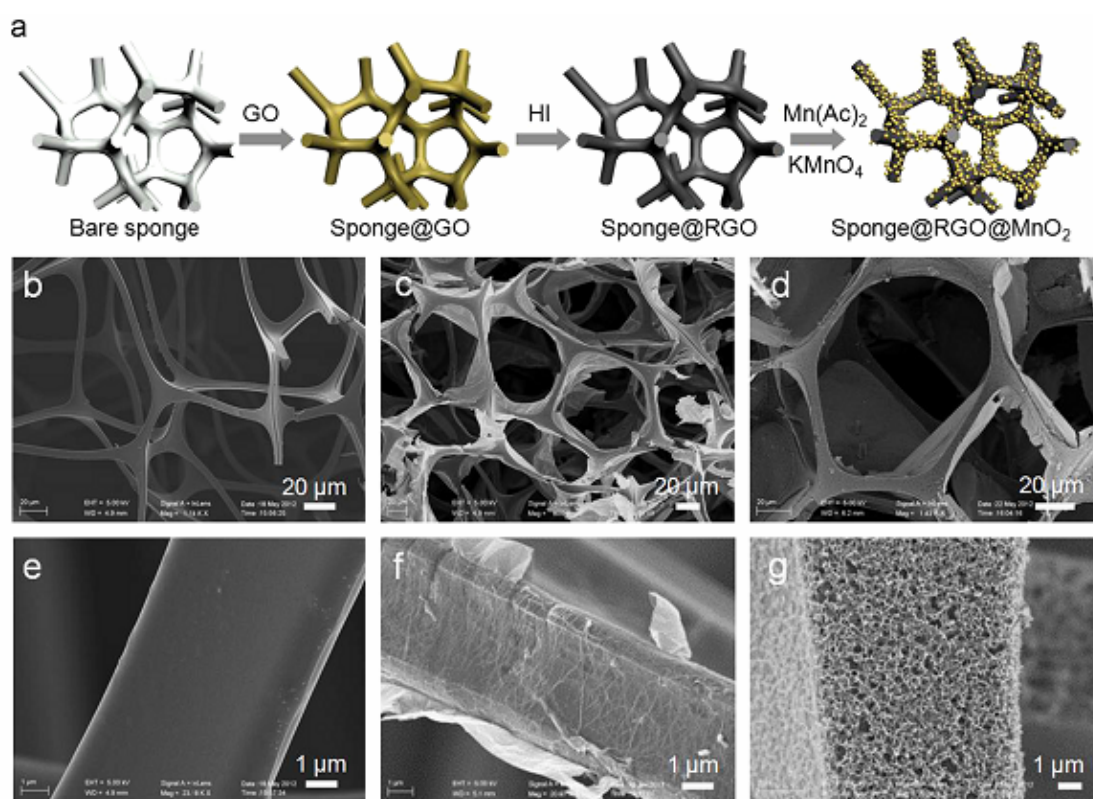


Fig. 15 (a) Schematic illustration of the synthesis of Sponge@rGO@MnO₂ hybrid. SEM images of bare sponge (b, e), sponge@rGO (c, f), and sponge@rGO@MnO₂ (d, g). (Reproduced with permission from ref. 317. Copyright 2013, Elsevier Ltd.)

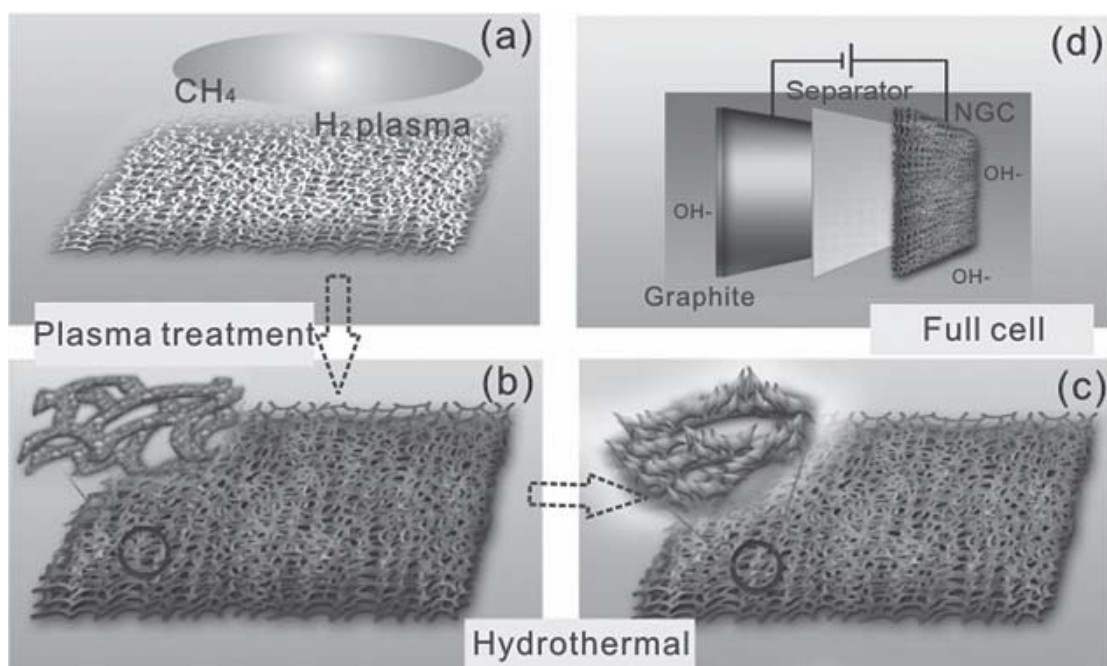


Fig. 16 (a-c) Schematic illustration of the fabrication process of NiO/GE composites: (a) Ni foam was treated by MPCVD in a H_2/CH_4 mixture. (b) The deposition process of GE on the Ni foam. (c) NiO/GE hybrid was formed by hydrothermal synthesis. (d) Schematic illustration of the configuration of a full cell by using the prepared hybrid as electrode. (Reprinted with permission from ref. 333. Copyright 2014 Wiley-VCH)

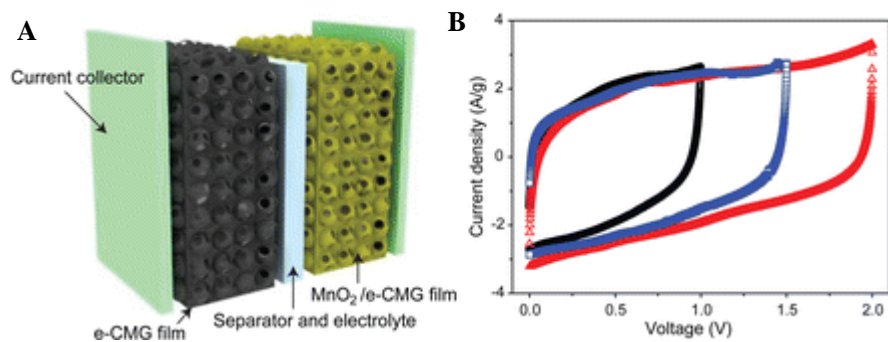


Fig. 17 (A) Schematic diagram of the configuration of e-CMG//MnO₂/e-CMG-based ASC device. (B) CV curves at 50 mV s⁻¹ obtained from the ASC with different voltage window of 1, 1.5, and 2.0 V. (Reprinted with permission from ref. 348. Copyright 2012 American Chemical Society)

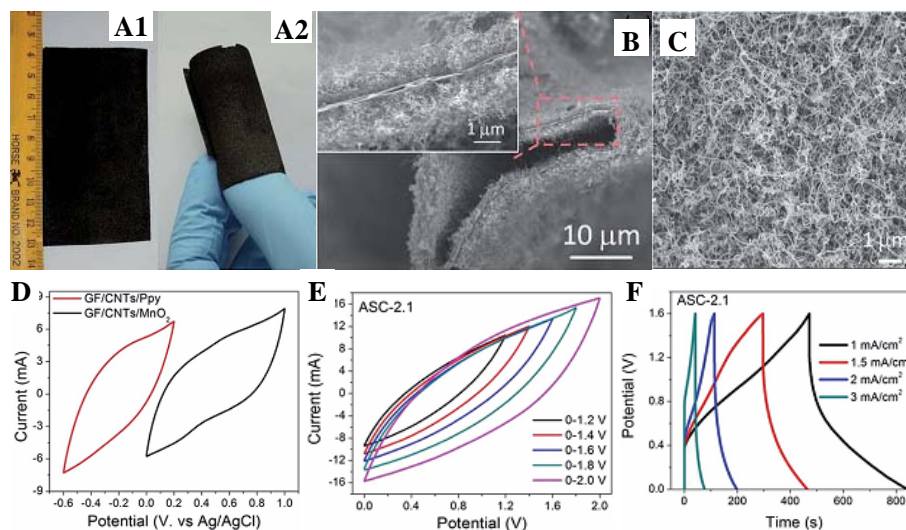


Fig. 18 (A1 and A2) Typical photographs demonstrating the large-size and flexibility of the CNT/GE foam. (B) Cross-sectional SEM image of a CNT/GE branch. (C) Top view SEM image of CNT/GE foam. (D) CV curves of GE/CNT/MnO₂ electrode and GE/CNT/Ppy electrode at 20 mV s⁻¹ in 0.5 M Na₂SO₄ electrolyte. (E) CV curves of ASC-2.1 measured at 50 mV s⁻¹ with different potential windows. (F) Galvanostatic charge–discharge curves of ASC-2.1 cell at different current densities. (Reprinted with permission from ref. 39. Copyright 2014 Royal Society of Chemistry)

Table 1 Summary of capacitive performances of the supercapacitors based on binder-free pristine GE structures.

Samples	Fabrication method	C	SSA	C _s	κ	R	E	W	T	C%	Ref.
GE nanoribbon carpet	Unzipping of CNT carpet	/	309	106.2 ⁽²⁾	/	/	9.4	103	2000	>95	53
GE nanoribbon aerogels	Unzipping of CNT aerogel	/	113.1	114.8 ⁽³⁾	36	/	/	/	/	/	54
rGO hydrogel	Hydrothermal assembly	0.5	/	175 ⁽²⁾	0.49 ± 0.2	/	/	/	/	/	166
rGO hydrogel film	Interfacial gelation	103.3	>600	160 ⁽²⁾	103.3	1.95	/	/	4000	97.8	86
rGO film	Casting and freeze dried	/	/	172 ⁽²⁾	18	<2	/	/	5000	99	120
rGO/GE/Ni foam	CVD+filtration	/	/	180 ⁽²⁾	/	0.93	>6	112.6	2000	100	193
rGO hydrogel	Hydrothermal assembly	192	~414	196 ⁽²⁾	192	/	0.61	0.67	10000	91	168
rGO foam	Al fiber blanket template	/	/	216 ⁽³⁾	/	3.5	/	/	/	/	185
rGO hydrogel	Hydrothermal assembly	>1.3	215	222 ⁽²⁾	2.7	/	5.7	30	2000	92	129
Vertical GE/Ni foam	CVD	/	/	230 ⁽³⁾	/	<35	/	/	1500	~99	199
GE film	CVD	/	/	247.3 ⁽²⁾	/	/	/	/	1500	100	189
rGO film	Laser reduction	1738	1520	265 ⁽²⁾	1738	/	/	/	1000	96.5	56
rGO hydrogel film	Filtration	/	/	273.1 ⁽²⁾	/	<2	150.9	776.8	10000	97	146
Holey rGO hydrogel	Hydrothermal assembly	~1000	830	310 ⁽²⁾	~1000	0.65	127	/	20000	95	37
rGO film on SSS	Far-infrared reduced	/	/	320 ⁽²⁾	~1020	0.5	~11.1	~25	10000	94	125
rGO fiber	Wet spinning	2508 ± 632	2210	409 ⁽²⁾	2508 ± 632	/	14	25	5000	1000	183

(C, electrical conductivity, S m⁻¹; SSA, specific surface area, m² g⁻¹; C_s, gravimetric specific capacitance, F g⁻¹, the number in superscript represents the configuration of supercapacitor cell, i.e. 2- or 3-electrode system; κ, electronic conductivity tested by four-probe method, S/m; R, internal resistance obtained from electrochemical impedance spectra measurements, Ω; E, maximum energy density, Wh kg⁻¹; W, maximum power density, kW kg⁻¹; T, cycles of cycle life test; C%, retention rate of C_s after cycle life test)

Table 2 Summary of capacitive performances of the supercapacitors based on binder-free GE/carbon hybrid materials.

Samples	C_s	R	E	W	T	C%	Ref.
CB/rGO	175 ⁽³⁾	0.7	/	/	6000	90.9	207
SWCNT/rGO	222 ⁽²⁾	/	106.6	10.9	1000	98.6	216
GNR/rGO aerogel	256 ⁽³⁾	/	/	/	10000	80.4	55
GQD/rGO aerogel	268 ⁽²⁾	<15	/	/	5000	90	204
CNT/GE/graphite paper	278 ⁽³⁾	18	/	/	8000	99	219
Ag/GE foam/OMC	213 ⁽²⁾	0.7	4.5	5.04	10000	>90	190
Porous C/rGO foam	238 ⁽²⁾	/	/	/	3000	/	203
Porous C/rGO aerogel	324 ⁽³⁾	~2	/	/	10000	>90	213
CNF/rGO mats	263.7 ⁽²⁾	0.8	/	/	2000	86.9	96
Porous C/rGO foam	379 ⁽³⁾	2.2	63.7	11	2000	94	212
CNT/rGO film	428 ⁽³⁾	2	59.4	50	10000	98	211

(C, electrical conductivity, $S\ m^{-1}$; SSA, specific surface area, $m^2\ g^{-1}$; C_s , gravimetric specific capacitance, $F\ g^{-1}$, the number in superscript represents the configuration of supercapacitor cell, i.e. 2- or 3-electrode system; R, internal resistance obtained from electrochemical impedance measurements, Ω ; E, maximum energy density, $Wh\ kg^{-1}$; W, maximum power density, $kW\ kg^{-1}$; T, cycles of cycle life test; C%, retention rate of C_s after cycle life test)

Table 3 Capacitive performances of some typical binder-free GE/conducting polymer hybrid electrodes.

Samples	C_s	R	T	C%	Ref.
PANI/GE foam	1024 ⁽³⁾	10	5000	87	270
PANI/rGO film	385 ⁽²⁾	3.5	5000	88	265
PANI/rGO film	1739 ⁽²⁾	<1	10000	93	267
PANI/rGO/CNT film	498 ⁽³⁾	<10	3000	95.8	264
PANI/rGO paper	763 ⁽²⁾	4.1	1000	82	262
PANI/GNR/CNT	890 ⁽²⁾	1.31	1000	89	261
PANI/rGO foam	790 ⁽²⁾	0.84-1.16	5000	80	266
PANI/rGO/cellulose paper	464 ⁽²⁾	/	1000	89	260
PANI/rGO/Ag/carbon fiber paper	828 ⁽³⁾	<10	3000	97.5	23
PPy/GO film	960 ⁽³⁾	<20	300	~100	24
PPy/rGO foam	350 ⁽²⁾	/	1000	~100	84
PPy/rGO membrane	284 ⁽³⁾	<2	5000	93	274
PEDOT/rGO film	213 ⁽³⁾	/	2000	87	252
PEDOT/rGO/C fiber cloth	714.93 ⁽³⁾	/	/	/	277
PpDA/rGO	248 ⁽²⁾	0.6-0.67	1000	72	29

(C_s , gravimetric specific capacitance, $F g^{-1}$, the number in superscript represents the configuration of supercapacitor cell, i.e. 2- or 3-electrode system; R, internal resistance obtained from electrochemical impedance measurements, Ω ; W, maximum energy density, $Wh kg^{-1}$; P, maximum power density, $kW kg^{-1}$; T, cycles of cycle life test; C%, retention rate of C_s after cycle life test.)

Table 4 Capacitance performances of the supercapacitors fabricated from some typical hybrids of binder-free GE/transition metal compounds.

Samples	C_s	R	E	W	T	C%	Ref.
MnO ₂ /CNT/GE/Ni foam	~251 ⁽²⁾	1.37	29	/	3000	82	12
MnO ₂ /CNT/GE foam	343.1 ⁽²⁾	2.15	4.95	5.95	1000	95.3	320
MnO ₂ /CNT/GE foam	326 ⁽³⁾	2.4	170	42	1000	95	318
MnO ₂ /rGO	450 ⁽²⁾	6.5	8.37	47	10000	90	317
MnO ₂ /GE foam	465 ⁽³⁾	<2.41	6.8	2.5	500	81.2	319
MnO ₂ /CNT/GE/Ni foam	1108.79 ⁽²⁾	~1	391.7	799.84	14000	97.94	322
Co(OH) ₂ /graphene/Ni foam	693.8 ⁽³⁾	/	/	/	3000	91.9	326
Co ₃ O ₄ /GE foam	768 ⁽³⁾	<7.5			500	143	14
Co _{0.66} Ni _{0.33} (OH) ₂ /GE foam	1847 ⁽³⁾	<50	62	/	1000	64	288
NiCo ₂ O ₄ /rGO/Ni foam	2260 ⁽³⁾	<0.5	/	/	10000	92.8	15
NiO/CNT/GE/Ni foam	815.5 ⁽³⁾	/	18.1	2.0	3000	110	13
NiO/GE foam	816 ⁽³⁾	~1	/	/	2000	115	329
NiO/GE foam	1829 ⁽³⁾	/	/	/	5000	81	333
rGO/Ni(OH) ₂ /Ni foam	1404 ⁽³⁾	/	/	/	1000	89.9	295
rGO/Ni(OH) ₂ /Ni foam	1250.3 ⁽³⁾	<1	/	/	1000	>95	292
Ni ₃ S ₂ /rGO	1424 ⁽³⁾	<4	/	/	3000	83	19
SnO ₂ /rGO	471 ⁽³⁾	/	/	/	1000	72	296
Fe ₃ O ₄ /rGO	368 ⁽³⁾	/	/	/	1000	108.9	18
V ₂ O ₅ /CNT/GO/textile	2590 ⁽³⁾	/	96	9	5000	97	17
RuO ₂ /CNT/GE/Ni foam	502.78 ⁽²⁾	2.7	39.28	128.01	8000	106	334

(C_s , gravimetric specific capacitance, F g⁻¹, the number in superscript represents the configuration of supercapacitor cell, i.e. 2- or 3-electrode system; R, internal resistance obtained from electrochemical impedance measurements, Ω ; E, maximum energy density, Wh kg⁻¹; W, maximum power density, kW kg⁻¹; T, cycles of cycle life test; C%, retention rate of C_s after cycle life test.)

Table 5 Summary of the capacitance performances of various asymmetric supercapacitors (ASCs) fabricated from binder-free GE-based materials

Samples	Electrolyte	C_P	C_N	C_A	R	V	E	W	T	C%	Ref.
MnO ₂ /RGO paper//RGO paper	1 M Na ₂ SO ₄	243 ⁽³⁾	67 ⁽³⁾		~2	1.6	/	/	3600	/	347
MnO ₂ /CMG film//CMG film	1 M Na ₂ SO ₄	389 ⁽³⁾	202 ⁽³⁾	/	/	2.0	44	25	1000	95	348
MnO ₂ -ERGO//CNT-ERGO	PAAK/KCl gel	422.5 ⁽³⁾	280.4 ⁽³⁾	69.4 ⁽²⁾	/	1.8	31.8	9.2	10000	84.4	40
Ni-Co-S arrays//rGO film	1 M KOH	1418 ⁽³⁾	332 ⁽³⁾	133 ⁽²⁾	/	1.8	60	28.8	50000	63.2	94
GF/CNT/MnO ₂ //GF/CNT/PPy	0.5 M Na ₂ SO ₄	215 ⁽³⁾	/	/	<20	1.6	22.2	10.3	10000	90.2	39
rGO/CNT/MnO ₂ //AC/CNT	1 M Na ₂ SO ₄	/	203 ⁽³⁾	46 ⁽²⁾	~10	2	27	7.8	2000	95	343
rGO/MnO ₂ //Ag/rGO	1 M Na ₂ SO ₄	/	/	112.8 ⁽²⁾	/	1.8	50.8	90.3	/	/	342
CNTG-40//MG-50	PAAK/KCl gel	302.9 ⁽²⁾	99.7 ⁽²⁾	72.6 ⁽²⁾	/	1.8	32.7	/	10000	86	339
rGO/MnO ₂ //V ₂ O ₅ /rGO	1 M LiTFSI	13 ⁽²⁾	21.3 ⁽²⁾	36.9 ⁽²⁾	~90	2	15.4	0.4	/	/	345
Au/MnO _x //rGO	1 M Na ₂ SO ₄	854.6 ⁽³⁾	214.5 ⁽³⁾	108.5 ⁽²⁾	/	1.8	46.8	11.83	2000	96.5	340
MnO ₂ /rGO textile//CNT/textile	0.5 M Na ₂ SO ₄	~315 ⁽³⁾	/	/	<50	1.5	12.5	110	5000	~95	310
CNT/MnO ₂ /GR//PANI/CNT	Na ₂ SO ₄ /PVP	486.6 ⁽³⁾	/	/	6.8	1.6	24.8	/	/	/	341
MnO ₂ /rGO//PANI/rGO	PVA/LiCl	491 ⁽³⁾	220 ⁽³⁾	39 ⁽²⁾	~22	1.7	16	7.4	2000	75	336
H-MnO ₂ //rGO	PVA/LiCl	449 ⁽³⁾	/	50.97 ⁽²⁾	/	1.8	/	/	5000	95.5	346
MnO ₂ /ZnO//rGO	PVA/LiCl	/	/	/	0.2	1.8	/	/	5000	98.5	337
MnO ₂ /rGO//rGO	2 M EMIMBF ₄ /AN	236 ⁽³⁾	150 ⁽³⁾	/	/	3.5	68.4	8.79	1000	80	302
MnO ₂ /rGO fiber//CNT/rGO fiber	PVA/LiCl	/	/	/	/	1.6	/	/	8000	92.7	131
MnO ₂ /Ni foam//rGO	0.5 M Na ₂ SO ₄	266.8 ⁽²⁾	157.7 ⁽²⁾	41.7 ⁽²⁾	6.9	2	23.2	10	5000	83.4	344

(C_P , specific capacitance of the positive electrode, F g⁻¹; C_N , specific capacitance of the negative electrode, F g⁻¹; C_A , specific capacitance of ASC cell, F g⁻¹, the number in superscript represents the configuration of supercapacitor cell, i.e. 2- or 3-electrode system; R, internal resistance obtained from electrochemical impedance measurements of ASC, Ω ; V, cell voltage of ASC cell, V; E, maximum energy density of ASC cell, Wh kg⁻¹; W, maximum power density of ASC cell, kW kg⁻¹; T, cycles of cycle life test; C%, retention rate of C_A after cycle life test.)